ZIKA VIRUS PATHOGENESIS IN THE DEVELOPING BRAIN AND THE INNER EAR

by

Ankita Thawani

A Dissertation

Submitted to the Faculty of Purdue University

In Partial Fulfillment of the Requirements for the degree of

Doctor of Philosophy

Department of Biological Sciences

West Lafayette, Indiana

May 2019

THE PURDUE UNIVERSITY GRADUATE SCHOOL
STATEMENT OF COMMITTEE APPROVAL

Dr. Donna M. Fekete, Chair
Department of Biological Sciences
Dr. Andrea L. Kasinski
Department of Biological Sciences
Dr. Richard J. Kuhn
Department of Biological Sciences
Dr. R. Claudio Aguilar
Department of Biological Sciences
Dr. Douglas J. LaCount
Department of Medicinal Chemistry and Molecular Pharmacology

Approved by:
Dr. Stephen F. Konieczny
Head of the Graduate Program

To Late Ms. Lata Thawani- my third parent, my forever advocate,
and my best friend.

ACKNOWLEDGMENTS

I thank my incredible mentor and “science mom”- Donna Fekete. She has been a constant pillar of support, inspiration, and a firm believer of my abilities even when I doubted myself. I want to thank my PhD advisory committee- Andrea Kasinski, Richard Kuhn, Claudio Aguilar, Doug LaCount- for encouraging and navigating my progress through the years in the graduate program. I really appreciate the teaching opportunities and career guidance provided by my TA mentors- Yuk Fai Leung and David Eichinger.

I am truly indebted to all the incredible members in Fekete lab- Deb Biesemeier, Vidhya Munnamalai and Katie Scott- who were my mentors, colleagues, friends and sounding boards when I needed them. These projects would not have been possible if not for the enthusiastic and invaluable assistance from the undergraduate researchers I worked with- Nabilah Sammudin, Hannah Reygaerts, Sydney Tola, Nick Lundin and Zoe Cubero.

I truly value our colleagues- Drs. Doris Wu, Devika Sirohi and Sumihare Noji, for sharing plasmids and reagents that contributed to my experiments. Purdue Statistics Consulting Services and Small Animal MRI facilities provided resources and guidance for some experiments. I thank the Purdue Research Foundation and Bilsland Dissertation Fellowships for funding my work.

I am sincerely grateful for all the love and championing from my family- Anita Thawani, Ashok Thawani, Lata Thawani, Akanksha Thawani, Bagheera, Phoebe, and Apoorv Thawani.

I am whole-heartedly appreciative of Jason St. John, Samarth Mathur, Logan Ganzen, Arpita Pal and Nabilah Sammudin for fortifying and enriching my personal as well as professional life. A big shout-out to Gina Rupp, for being a cheerleader to me until the finish line.

Lastly, I want to acknowledge the Internet and the abundance of cat videos for bringing me instant joy and humor whenever needed.

PREFACE

"It was the best of times, it was the worst of times,
it was the age of wisdom, it was the age of foolishness,
it was the epoch of belief, it was the epoch of incredulity,
it was the season of Light, it was the season of Darkness,
it was the spring of hope, it was the winter of despair,
we had everything before us, we had nothing before us,
we were all going direct to heaven, we were all going direct the other way."
- Charles Dickens

TABLE OF CONTENTS

LIST OF TABLES

LIST OF FIGURES

LIST OF ABBREVIATIONS

A	Anterior
ABC	Avidin-biotin complex
ABR	Auditory brainstem response
AG	Auditory ganglion
ANOVA	Analysis of variance
AP	Alar plate
Bmp	Bone morphogenetic protein
BP	Basal plate
BP	Basilar papilla
C/Cu	Cuboidal cells
CA	Crista ampullaris
CAM	Chorioallantoic membrane
CD	Cochlear duct
CDC	Centers of Disease Control and Prevention
D	Dorsal
DAB	Di-amino benzidine
DE	Diencephalon (posterior forebrain)
DENV	Dengue virus
DEPC	Diethyl pyrocarbonate
DNA	Deoxy-ribonucleic acid
dpi	Days post-infection
dsRNA	Double stranded RNA
E	Embryonic day
ED	Endolymphatic duct
ES	Endolymphatic sac
FB	Forebrain
Fgf	Fibroblast growth factor
FP	Floor plate
HB	Hindbrain

HCL	Hair cell layer
HH	Hamburger Hamilton stage
Hm	Homogene cells
HRP	Horseradish peroxidase
Hy	Hyaline cells
Hypo	Hypothalamus
Ig	Immunoglobulin
L	Lateral
LM	Lagenar macula
MB	Midbrain
MHB	MB-HB boundary
MRI	Magnetic resonance imaging
NF	Neurofilament
Nkx2	NK2 homeobox 2
OAE	Otoacoustic emission
P	Posterior
Pax	Paired box protein
PBS	Phosphate-buffered saline
PCR	Polymerase chain reaction
PFU	Plaque forming unit
PreT	Pretectum
Ptch1	Patched 1
Pth	Prethalamus
qRTPCR	Quantitative real time polymerase chain reaction
RNA	Ribonucleic acid
RP	Roof plate
SAG	Stato-acoustic ganglion
SC	Semicircular canals
SCL	Supporting cell layer
Shh	Sonic hedgehog
SM	Saccular macula

Sox2	SRY (sex determining region Y)-box 2
TAM	Tyro3, Axl, and Mer
TE	Telencephalon (anterior forebrain)
TFM	Tissue freezing media
Th	Thalamus
TIM	T-cell immunoglobulin and mucin domain
TORCHES	TOxoplasmosis Rubella Cytomegalovirus HErpes Syphilis
TUNEL	Terminal deoxynucleotidyl transferase dUTP nick end labeling
Tv/T	Tegmentum vasculosum
UM	Utricular macular
V	Ventricle
VG	Vestibular ganglion
WHO	World Health Organization
Wnt	Wingless/Integrated
ZIKV/Z	Zika virus
ZLI	Zona Limitans Intrathalamica

ABSTRACT

Author: Thawani, Ankita. PhD
Institution: Purdue University
Degree Received: May 2019
Title: Zika Virus Pathogenesis in the Developing Brain and the Inner Ear
Major Professor: Donna M. Fekete

Zika virus (ZIKV) is a mosquito-borne pathogen that stayed unnoticed for over half a century. Only after the 2015-16 Brazilian outbreak did the severity of the infectious outcome, particularly the Congenital Zika Syndrome, become apparent. ZIKV is associated with severe neurodevelopmental impairments in human fetuses, including microencephaly, ventriculomegaly, retinopathy, and sensorineural hearing loss. Though the pandemic is now under control in the Latin American countries, several tropical countries could still be at risk of widespread infection. This warrants a better understanding of the congenital Zika syndrome; this project attempts to contribute towards this goal.

Previous reports examining neural progenitor tropism of ZIKV in organoid and animal models did not address whether the virus infects all neural progenitors uniformly. To explore this, ZIKV was injected into the neural tube of 2-day-old chicken embryos, resulting in non-uniform periventricular infection 3 days later. Recurrent foci of intense infection were present at specific signaling centers that influence neuroepithelial patterning at a distance through secretion of morphogens. ZIKV infection reduced transcript levels for 3 morphogens, SHH, BMP7, and FGF8, expressed at the midbrain basal plate, hypothalamic floor plate, and isthmus, respectively. Levels of Patched1, a SHH-pathway downstream gene, were also reduced and a SHH-dependent cell population in the ventral midbrain was shifted in position. Thus, the diminishment of signaling centers through ZIKV-mediated apoptosis may yield broader, non-cell autonomous changes in brain patterning.

Sensorineural hearing loss is a relatively understudied consequence of congenital Zika syndrome, and balance disorders are essentially unreported to date. ZIKV pathogenesis was explored in the developing inner ear using the accessible chicken embryo model system. One goal was to assess the spatiotemporal susceptibility of otic epithelial-derived structures to ZIKV infectivity. Direct injections of the inner ear or the inner ear primordium were performed *in ovo* with subsequent harvests at 2 to 8 days-post-infection. The degree of infection in

sensory/prosensory organs was evaluated histologically to determine the susceptibility of one auditory and five vestibular organs. ZIKV infection of the sensory as well as non-sensory epithelia was observed at most stages of analysis, with no apparent preference for one over the other. The lagena, the ventral most tip of the chicken inner ear, and the endolymphatic sac/duct were least frequently infected. In this report, two novel findings in sequela of ZIKV infection are presented: the vestibular labyrinth can present with stalled canal morphogenesis, and the auditory ganglion can be severely shrunken, perhaps due to an increased cell death upon early ZIKV infection of the inner ear.

Additional methods of peripheral infection in the chicken embryos were tested to examine ZIKV transmission to the central nervous system: E3 blood vessel, E4 limb bud, and E10 chorioallantoic membrane infections. Although none of these methods resulted in a histologically significant infection of the developing brain 3 to 6 days-post-infection, evidence of ZIKV genome replication and viremia was detected in several tissue types.

CHAPTER 1. INTRODUCTION

1.1 Zika virus- Background and Pathology

Zika virus (ZIKV) is single-stranded RNA virus with a positive-sense RNA strand as the genome (Sirohi et al., 2016). ZIKV belongs to a family of arthropod-borne viruses called Flaviviridae, with dengue virus (DENV), spondweni virus, and West Nile virus as its phylogenetic neighbors (Weaver et al., 2016). The first discovery of this virus occurred about seven decades ago in the Zika forests of Uganda, when a group specializing in isolating and characterizing previously unknown viruses from the African forests stumbled upon ZIKV during a Yellow Fever study (Dick et al., 1952). They isolated the virus from febrile rhesus monkeys as well as local mosquitoes, provided evidence for infection, adaptation and morbidity in mice, and found seropositivity in 6.1% of the local population (Dick, 1952; Dick et al., 1952). However, since then, ZIKV remained a relatively obscure and mild febrile disease as it spread across several continents (Gatherer and Kohl, 2016). Its obscurity was transcended during the 2015-16 outbreak in Latin America, with a 20-fold increase in the occurrence of a microcephalic phenotype in human fetuses and newborns that correlated with maternal ZIKV infection. This attracted the attention of the media, and galvanized the scientific community to study symptomatology, pathogenesis, and transmission of ZIKV (Coelho and Crovella, 2017; Gyawali et al., 2016; Marrs et al., 2016). For much of 2016, WHO declared ZIKV to be a Public Health Emergency of International Concern (Gulland, 2016). The declaration was rescinded as the pandemic was brought under control through awareness and diminishing the mosquito population (Frieden et al., 2016); WHO, 2018) and possibly through herd immunity in local populations following the first wave of infection (Siedner et al., 2018). Nevertheless, because viral pandemics can reoccur, it is important to continue to study ZIKV biology and better understand the associated spectrum of medical complications. This thesis represents our efforts to contribute to this goal using the chicken embryo as an animal model.

1.1.1 Epidemiology and Etiology of ZIKV

The primary route of ZIKV transmission is through infected mosquitoes, mostly of the *Aedes* species (Dick et al., 1952; Weger-Lucarelli et al., 2016). Recently, strong evidence has been reported for two routes of transmission: *in utero* transmission from an infected pregnant mother to

the gestating fetus (Guillemette-Artur et al., 2016; Moore et al., 2017); and sexual intercourse with infected males (Foy et al., 2011; Hills et al., 2016).

Two phylogenetically distinct groups of ZIKV have been identified as (1) the African (ancestral or pre-epidemic) lineage from the Zika forests, and (2) the Asian lineage that caused the South American pandemic (Pettersson et al., 2018; Pettersson et al., 2016). *In vitro* and *in vivo* studies comparing the virulence and severity of the two strains are elaborated further in section 1.1.4. Using evidence from comparative genomics, several theories have been advanced for why the virus remained under the radar for several decades and why over time ZIKV pathology changed to cause severe birth defects. Hypotheses include mutations in either the surface proteins important for viral maturation or in non-coding segments of the genome that antagonize the host response proteins (Yuan et al., 2017; Zhu et al., 2016). Several high-population tropical and sub-tropical countries, such as India, with known seroprevalence of DENV and other arboviruses, are concerned about the potential of future outbreaks with these high-risk ZIKV strains (Doss et al., 2017; Gyawali et al., 2016; Mourya et al., 2016).

Only since 2007 have cases of ZIKV outbreak with adverse symptomatology been recorded; locales include the Yap islands in Micronesia, French Polynesia, and more recently Brazil and several other Latin American countries (Pettersson et al., 2018; Pettersson et al., 2016). According to the CDC, in the last 3 years, about 5,740 cases of infected individuals have been confirmed with laboratory evidence in the United States of America, and over 37,000 cases were reported in the American territories. In the territories, perhaps due to the tropical mosquito-breeding weather, 99.6% of the cases were due to local mosquito-mediated transmission; whereas in the states, only 4% of the cases recorded can be attributed to local mosquito bites, notably in the warmer states like Texas and Florida. Instead, 95% of the cases in the American states were observed in travelers that had recently visited an affected country. Infection in adults results in mild symptoms such as fever, arthralgia, myalgia, and/or a rash in only 20% of the cases, with a smaller percentage of that presenting with Guillain Barré Syndrome (peripheral neuropathology) (Barbi et al., 2018; do Rosario et al., 2016; Gatherer and Kohl, 2016; Mlacker et al., 2016). However, when pregnant mothers are infected, the gestating fetus can incur severe congenital defects, also referred to as the Congenital Zika Syndrome with the classic symptomatic presentation of microcephaly, defined as a head circumference more than 2 standard deviations below the mean [Congenital Zika Syndrome is further explained in section 1.1.3] (Ashwal et al., 2009; Moore et al., 2017; Rasmussen et al., 2016). Around 2,500 cases of pregnant women with

laboratory evidence of ZIKV infection have been detected in the American states with around 5% of those resulting in detrimental effects ranging from irreversible birth defects to loss of pregnancy (CDC, 2018).

Since 2015, attempts at designing antibodies, vaccines, and drug discovery to combat ZIKV infection have been pursued (Dai et al., 2016; Hasan et al., 2017; Retallack et al., 2016; Sacramento et al., 2017; Sirohi and Kuhn, 2017). FDA-approved compounds such as sofosbuvir (anti-viral used against Hepatitis C infection) and azithromycin (common anti-bacterial known to be safe in pregnancy) show promising results of reduced ZIKV proliferation *in vitro* (Retallack et al., 2016; Sacramento et al., 2017).

1.1.2 Structure and infection of the Zika virus

Similar to the other family members of the Flaviviridae family, ZIKV displays an icosahedral symmetry with several layers of proteins and glycosylation motifs. The outermost layer of glycosylated proteins, the envelope layer, is detected by transmembrane receptors on the target cells to initiate clathrin-mediated endocytosis of the viral particles. The envelope proteins and the membrane proteins are stacked to form somewhat-dynamic raft facets that are rooted in a lipid bilayer surrounding the capsid proteins that directly interact with the RNA genome. Epitopes on the envelope proteins are thought to be responsible for receptor binding and tissue tropism (Sirohi et al., 2016; Sirohi and Kuhn, 2017). At the inner-most core of the virus lies the single-stranded RNA genome comprises of ~11 kilobases of information encoding structural and non-structural components of the virus. Structural components include the capsid, membrane, envelope proteins etc., whereas the non-structural components are quintessential for virulence, viral propagation and host-immunity suppression, such as viral proteases and polymerases (Bollati et al., 2010; Sirohi and Kuhn, 2017).

When the viral genome replicates, double stranded RNA (dsRNA) motifs form that are often looked for indicating cellular infection (Weber et al., 2006). During the initial assembly of the virus at the endoplasmic reticulum, the membrane protein assembles as a precursor version in the immature or “spiky” virions. Cleavage by certain endogenous proteases results in the matured M protein and thus the bioactive or “smooth” version of ZIKV. In nature, however, most viral particles found are partially mature where the cleaved membrane protein facets can still bind to the respective host receptor (Sirohi et al., 2016; Sirohi and Kuhn, 2017).

Cell adhesion receptors such as DC-SIGN, and certain lectins are identified to be the entry points for flaviviruses where the specific glycosylation motifs on the envelope proteins can bind to cell-specific adhesion molecules. Additionally, the TIM/TAM family of receptors, the most well studied in the context of ZIKV tropism, that detect phosphotidyl serine motifs on apoptotic cells with the help of ligands like Growth arrest-specific 6 (GAS6), can be hijacked by these dynamic flaviviruses for entry into the target cells (Hamel et al., 2015; Sirohi and Kuhn, 2017).

1.1.3 Congenital Zika Syndrome

Numerous teratogenic pathogens, often referred to as TORCHES agents (TOxoplasmosis Rubella Cytomegalovirus HErpes Syphilis), cause mild to no disease symptoms in adult; however, when the pregnant mother is infected, the virus can be transmitted to the gestating fetus and can cause developmental defects (Rasmussen et al., 2016). Many of such viruses belong to the Flaviviridae family, including Hepatitis C virus and Bovine viral diarrhea virus (causes microcephaly in calves) (Mlacker et al., 2016). ZIKV drew attention when the incidence of babies born with microcephaly, a smaller head circumference mostly due to a smaller brain, increased by 20-fold in Brazil, and could be traced back to the ZIKV pandemic (Coelho and Crovella, 2017; Gyawali et al., 2016; Marrs et al., 2016; Rasmussen et al., 2016). Retrospective investigation into the previous 2013-14 outbreak in French Polynesia revealed a similar phenotype evidenced by the available ultrasounds and MRI data (Besnard et al., 2016; Guillemette-Artur et al., 2016; Musso et al., 2014).

ZIKV infection, when transmitted from an infected pregnant mother to the gestating fetus, can cause severe abnormalities and developmental defects, such as microencephaly, ventriculomegaly, irregular cortex, skull deformation, brain calcifications, cerebellar hypoplasia, brainstem dysfunction, corpus callosum defects, chorioretinal atrophy, sensorineural hearing loss, limb and joint deformities, overall intrauterine growth restriction, or even fetal mortality (Besnard et al., 2016; de Fatima Vasco Aragao et al., 2016; Driggers et al., 2016; Melo et al., 2016; Mlacker et al., 2016; Moore et al., 2017; Ventura et al., 2016). These symptoms are recognized under the umbrella of Congenital Zika Syndrome. Furthermore, the severity of the outcome correlates with the time of infection, with first trimester or early second trimester viral infection yielding more penetrating birth defects (Melo et al., 2016; Peterson et al., 2016; Rasmussen et al., 2016). Interestingly, several twin studies showed that the congenital defects can be conflicting, with one fetus completely normal while the other shows severe microcephaly with other brain defects

(Caires-Junior et al., 2018; Leal et al., 2016a). Since the nature of most of these defects is irreversible, coordinated care, physical therapy and regular check-ups are incredibly important as the child grows (CDC).

1.1.4 Neurotropism of Zika virus

Various *in vivo* and *in vitro* model organisms have been tested and established over the last couple of years that indicate the primary target of ZIKV infection is neural tissue, specifically the neural stem cells. An appreciation of the neurotropic nature of ZIKV dates back to the first communication of the ZIKV discovery in 1952, where intracerebral injection of viral isolate in mice resulted in morbid outcomes (Dick, 1952; Dick et al., 1952). In addition to infection of the neural progenitors, or radial glial cells, located at the ventricular zone in the neuroepithelium, numerous other cell populations such as immature neurons, astrocytes, oligodendrocyte precursors, microglia, and neural crest cells have been shown to be susceptible to ZIKV infection (Bayless et al., 2016; Retallack et al., 2016; Wang et al., 2018). ZIKV infection can even lead to neurovascular developmental defects and a leaky blood-brain-barrier (Shao et al., 2016). However, mature neurons are generally not susceptible to ZIKV. When infected, neural stem cells undergo apoptotic or necrotic death and proliferation reduces. Intranuclear vacuoles, lesions and gliosis can be observed in the neural tissue after infection (Adams Waldorf et al., 2016; Cugola et al., 2016). Infection of 3D brain organoids results in reduced size of the organoids compared to the uninfected controls (Garcez et al., 2016; Qian et al., 2016). After ZIKV injection in adult monkeys or immunocompromised mice via the subcutaneous, intravenous, or intraperitoneal route, the virus can be found in the brain and testes at high titers for a long time (Aliota et al., 2016; Dowall et al., 2016; Dudley et al., 2016; Hirsch et al., 2017; Lazear et al., 2016; Li et al., 2016b; Osuna et al., 2016; Rossi et al., 2016). Comparison of the rather recent Asian vs. the older African lineage of the virus suggests that the African lineage might be more virulent in certain cells, however the reduced cell death in Asian lineage infections might be a tactic for the virus to overcome the cellular innate immune responses (Anfasa et al., 2017; Cugola et al., 2016). Intraventricular infection of gestating murine embryos, as well as subcutaneous, intravenous, intraperitoneal, or intrauterine infection of pregnant mice or macaques each result in fetal brain defects and neural cell death (Adams Waldorf et al., 2016; Cugola et al., 2016; Huang et al., 2016; Li et al., 2016a; Vermillion et al., 2017; Wu et al., 2016; Wu et al., 2018; Yockey et al., 2016); the upregulation of interferon response genes is also observed (Li et al., 2016a; Wu et al., 2016). The chicken embryo

model system has also been demonstrated to be susceptible to ZIKV infection, with subsequent stunted brain growth observed (Goodfellow et al., 2016). Non-human primate data shows that infection occurring at later stages of development may not present a noticeable fetal phenotype. However, the mammalian sub-ventricular zone and hippocampus comprising of a few neural progenitors could be at risk of infection and consequentially undergo gliosis, or even cell death (Adams Waldorf et al., 2018; Adams Waldorf et al., 2016; Li et al., 2016b).

Using the knowledge from studies on DENV, a phylogenetic neighbor of ZIKV, it was determined that the virus likely binds to generic adhesion receptors on the target cell surface, such as heparan sulfate glycans and lectins. In addition to that, phosphotidylserine receptors such as TIM/TAM family of receptors are known to be important for flaviviral entry. Strong evidence points to a role of AXL, TYRO3, and other family members as entry receptors for ZIKV (Hamel et al., 2015; Perera-Lecoin et al., 2013). Interestingly, the AXL receptor is highly expressed in the ventricular zone of the neural epithelium and glial cells, indicating that expression of these receptors in neural stem cells could be correlated to their susceptibility to ZIKV infection (Meertens et al., 2017; Nowakowski et al., 2016). However, AXL seems to be sufficient yet not necessary for ZIKV infection (Hastings et al., 2017; Wells et al., 2016). Some evidence suggests that ZIKV suppresses the Type I interferon response system by AXL kinase downstream signaling and/or STAT2 to use the host transcriptional and protein maturation machinery for additional replication (Gorman et al., 2018; Meertens et al., 2017). Additionally, specific non-structural proteins of ZIKV, such as 2A, 4A, and 4B, have also been identified to be key players in the disruption of neurogenesis (Liang et al., 2016; Yoon et al., 2017).

In addition to the brain disorders, the sensory systems are also vulnerable to ZIKV infection. Bilateral or unilateral ocular defects, such as chorioretinal atrophy, lens subluxation, retinal pigmented epithelial mottling, are common morbidities associated with congenital Zika syndrome (de Paula Freitas et al., 2016; Miner et al., 2016b; Moore et al., 2017; Singh et al., 2017; Ventura et al., 2016). Sensorineural hearing loss has recently been added to the spectrum (Leal et al., 2016a; Leal et al., 2016b; Mittal et al., 2017).

1.1.5 Hearing loss associated with Zika virus

Sensorineural hearing loss is a relatively unexplored consequence of the congenital Zika syndrome. Several other infectious agents such as HIV, Herpes Simplex Virus, Cytomegalovirus, Rubella, etc., can result in congenital hearing loss either due to direct infection of the sensory cells,

or indirect effect of the immune system around the fragile inner ear tissue. Due to the limited regenerative capacity of the hair cells and the supporting tissue, such hearing damage cannot be cured, and the therapeutic measures involve hearing aids and cochlear implants (Cohen et al., 2014).

A medical report from Pernambuco, Brazil studied 70 babies with laboratory evidence of ZIKV infection and varying degrees of microcephaly. The clinicians observed that 5 out of the 70 newborns (7%) presented with unilateral or bilateral sensorineural hearing loss evidenced by diminished otoacoustic emissions (OAEs; a property of the healthy cochlea to emit detectable sounds in response to a pair of input frequencies) and auditory brainstem responses (ABRs; electrical brain impulses detected on the scalp in response to repetitive input sounds) (Leal et al., 2016b). Interestingly, all the newborns with hearing loss also presented with severe microcephaly (head circumference lesser than average by 3 times the standard deviation; (Ashwal et al., 2009)). Several studies suggest that the 6% occurrence of ZIKV-related hearing loss might be under-reported as only microcephalic babies were included (Fandino-Cardenas et al., 2018; Mittal et al., 2017). Furthermore, the 5 respective mothers were detected with ZIKV infection within the first 4 months of their pregnancies, indicating that there is possibly a temporal window when the cochlea is most susceptible to ZIKV mediated damage (Leal et al., 2016b).

1.2 Brain development in chicken embryos

The brain is the “supercomputer” of an organism with multiple inputs received from the environment, as well as within the animal, through the cranial nerves or the ascending sensory tracts along the spinal cord. The information is processed, and appropriate outputs are delivered to the respective muscles throughout the body via parallel opposing neural routes. The central nervous system is comprised of the brain and the spinal cord; the brain can be further segmented into the forebrain (FB), midbrain (MB), and hindbrain (HB). The development of the central nervous system begins around the fourth week of fetal gestation in humans, with FB, MB and HB clearly distinguishable within a couple of days, and by the end of gestation the majority of the cells in the brain are born. The remaining postnatal mass is built up by the axonal and dendritic projections of the neurons and glial cells (Lowery and Sive, 2009; Purves, 2008; Wolpert, 2007).

The FB, or prosencephalon, is divided into the telencephalon (TE) and the diencephalon (DE) as the anterior and posterior segments, respectively. The cerebral hemispheres, hippocampus, hypothalamus, thalamus, optic vesicles, olfactory bulbs, and basal ganglia (derived from a ventral

forebrain thickening or ganglionic eminences) arise from the prosencephalon. The prosencephalon undergoes three major cleavages to shape its morphology: (1) transverse, to separate the TE and DE; (2) sagittal, to form the two mirror-image hemispheres; and (3) horizontal for the optic cups (the retina). The MB, or mesencephalon, comprises of two main parts, the tectum and the tegmentum. The tectum is made up of the superior and inferior colliculi, that are important junctions for visual and auditory pathways and spatial mapping of the external world. The cephalic flexure at the midbrain results in vertebrates having a 90^0 bend in the body axis at the brain. The HB, or rhombencephalon, is made up of the pons, the medulla oblongata, and the cerebellum. Pontine and cervical flexures shape the rhombencephalon with cerebellum located dorsally behind the medulla and pons. The HB contains numerous relay junctions of information to the higher cortex; it also contains a collection of small nuclei called the reticular formation, with a myriad of functions in a very small space in the medulla. Barring specialized populations of neural stem cells in the hippocampus and the subventricular zone, as well as the mitotic abilities of glial cells in response to damage, the vast majority of adult brain neurons do not have proliferative capacity (Purves, 2008).

As a vertebrate, the early stages of neurodevelopment in the chicken embryo are comparable to human brain development. However, at later stages, the human brain becomes more complex, particularly with a six-layered neocortex with high gyrification. The chicken embryo is a long-standing model organism to study vertebrate development due to the ease of accessibility *in ovo*, allowing for surgical manipulations. Chicken embryos were some of the first animals dissected to study the neuroanatomy and embryonic development due to easily available fertilized eggs. Quail tissue implantation into chicken embryos to trace cell lineage are some of the classical experiments done to understand neural tube, crest cells, and limb development (Bronner-Fraser, 1996; Davey and Tickle, 2007).

1.2.1 Early development of the central nervous system- from ectoderm to the brain

Most multicellular organisms generate 3 germ layers during the process of gastrulation. A group of cells called the Hensen's node move posteriorly and form the notochord, a midline source of Sonic hedgehog (SHH) signaling. Neural tissue arises from the dorsal ectodermal layer (the neuroectoderm) with low to none Bone morphogenic protein (BMP) activity induced by the Hensen's node and the underlying notochord. During neurulation, the neuroectoderm makes a groove and closes along the anterior-posterior body axis and the resulting neural tube forms the

primordium for the central nervous system, with three distinct vesicles, the FB, MB and HB, and the spinal cord. The amniotic fluid enclosed within the neural tube becomes the ventricular cavity, that will eventually be filled with cerebrospinal fluid secreted by the choroid plexus. Neural tube closure starts in the middle and zippers in the anterior and posterior directions such that the two neuropores are the last regions to close. Improper closure of neural tube can lead to severe congenital anomalies such as spina bifida (posterior neural tube did not close completely), anencephaly (anterior neural tube did not close completely), and holoprosencephaly (disruption of ventral-anterior neural tube) (Purves, 2008; Rubenstein and Puelles, 1994; Wolpert, 2007).

During the fusion of the neural folds along the dorsal surface of the embryo, a bulk of neural crest cells migrate away deeper into the mesoderm; these ectodermal lineage cells are important for craniofacial connective tissue development (including the middle ear ossicles) and generate numerous sensory and sympathetic ganglia along the body and the enteric nervous system. Due to the unique and dynamic nature of neural crest cells, they have been referred to as the fourth germ layer in vertebrates (Purves, 2008; Rubenstein and Puelles, 1994; Wolpert, 2007).

Differential Wingless/Integrated (WNT) signaling is important during the early stages of development for anterior-posterior axis patterning. Combinatorial patterns of Hox-genes segment the neural tube into discrete positional units or neuromeres that have their individual genoarchitectural identities. Furthermore, the neural tube at these stages have two opposing signaling sources important for dorsoventral patterning of the central nervous system: (1) WNT/BMP at the roof plate (dorsal); and (2) SHH at the floor plate (ventral; induced by Shh expression from the underlying notochord). These two signals regulate the specification of sensory neurons in the dorsal side (alar side), and motor neurons in the ventral side (basal side). Shh-mediated suppression of dorsalizing Bmp signals is important for motor neuron fate specification (Hayhurst et al., 2008; Le Dreau and Marti, 2012; Puelles and Rubenstein, 2015; Purves, 2008; Rubenstein and Puelles, 1994; Wolpert, 2007).

As the neural tissue increases in thickness, the nuclei of radial glial cells, the progenitor population of the neural epithelium, swing between apical and pial surface, stopping at the apical (or ventricular) surface to divide. A symmetrical division parallel to the ventricular surface generates two progenitors, whereas an asymmetrical division (usually perpendicular to the ventricular surface) results in a radial glia located towards the apical side and a neuroblast, or an immature neuron, that migrates radially away from the ventricle and towards the pial surface. As the neurons mature, neural connectivity depends on long-range and short-range axonal guidance

cues to find the appropriate destination. Radial glia are Sox2-positive progenitor cells and are primarily located in the peri-ventricular region (Purves, 2008; Rubenstein and Puelles, 1994; Wolpert, 2007). In addition to the mature neurons, a majority of the adult brain weight is occupied by differentiated glial cells, such as astrocytes, oligodendrocytes, and microglia. The glial cells support the nervous system by myelination for faster impulse transmission, dendritic pruning, supplying nutrition to the neurons, and even guiding them during axonal outgrowth. Astrocytes, oligodendrocytes, and ependymal cells are born from the radial glia, however the microglia (the native macrophages of the central nervous system) are mesodermal by lineage (Ginhoux et al., 2013; Purves, 2008).

1.2.2 Evolutionarily conserved secondary organizers in the developing brain

Primary organizers, such as Hensen's node and the primitive streak, define the body axis and the neural tube. Several secondary organizers in the developing neural tube pattern the local neuroepithelium for fate specification of neuronal populations to pursue destined morphology and function. Morphogens are secreted cues that are essential for fate specification and patterning of the neighboring tissue in a concentration dependent manner. Morphogen protein is translated in the source cells and diffuses (or is transported) to the neighboring equipotent cells to pattern the tissue (Muller et al., 2013). Five key classes of morphogens are quintessential for patterning the embryo starting from a ball of cells: Shh, Bmps, Wnts, Fibroblast growth factors (Fgfs), and Retinoic acid. Several of these signaling pathways and signaling centers are largely conserved across the vertebrates (Echevarria et al., 2003; Ferran et al., 2008; Garcia-Lopez et al., 2009; Perez-Balaguer et al., 2009; Wurst and Bally-Cuif, 2001).

Two key morphogen-secreting organizers mentioned earlier, the floorplate and roofplate of the neural tube, pattern the motor and sensory regions. Along the anterior-posterior axis, several key boundary regions, such as anterior neural ridge, zona limitans intrathalamica (ZLI), and isthmus act in combination with the dorso-ventral patterning cues (Echevarria et al., 2003; Garcia-Lopez et al., 2009; Scholpp et al., 2006). At the midbrain-hindbrain boundary (MHB), the isthmic organizer secretes Wnt1 at the ventral side and Fgf8 at the dorsal side. An interaction between the OTX-expressing mesencephalon and the GBX-expressing rhombencephalon is hypothesized to be responsible for inducing the MHB. The isthmic organizer is important for cerebellum formation at the caudal side and the mesencephalon at the rostral side. Fgf8-soaked beads, when implanted in the neural tube, give rise to rudimentary cerebellum, isthmus, and mesencephalon. Knockdown of

Wnt1 results in loss of these structures (Cavodeassi and Houart, 2012; Echevarria et al., 2003; Wurst and Bally-Cuif, 2001). Another Shh-expressing domain, the ZLI, in the diencephalon, is located between the thalamus and the prethalamus. ZLI transplantation to other regions of the neural tube induces thalamic fate. At the dorsal tip of ZLI, yet another Wnt/Fgf boundary is located, making it an important signaling center (Echevarria et al., 2003; Lim and Golden, 2007). The anterior neural ridge is an Fgf secreting signaling center that is important for telencephalic development and rostral cortical neuron fate specification (Echevarria et al., 2003). In the brain, the Shh-expressing floorplate is key for specification of ventral neural populations via activation of transcription factor expression, such as the Nkx family. In synergy with the isthmus, it defines distinct neural populations such as dopaminergic, serotonergic, oculomotor neurons and reticular formation (Garcia-Lopez et al., 2009; Martinez-Lopez et al., 2015; Perez-Balaguer et al., 2009; Wurst and Bally-Cuif, 2001).

1.3 Inner ear in chicken embryos

Ears are one of the most complex and delicate sensory systems in animals, comprising of the outer ear (pinna, external auditory meatus and tympanic membrane), the middle ear (with 3 small ossicles and associated muscles) and the inner ear (the membranous labyrinth as the gateway to the central nervous system), with each of them playing a role in efficient conduction of mechanical “sound” energy. Audioception, or the sense of hearing, is the ability to convert the mechanical energy of the sound waves into electrical impulses conducted through the eighth cranial nerve, through the brainstem, through the thalamus and then to the primary auditory cortex. In addition to audioception, the inner ear is also important for sensing balance in all dimensions. The inner ear with its complex morphology is a fluid-filled labyrinth embedded in the temporal bone, housing sensory organs to detect sound and maintain balance. The mechanosensory cells or the hair cells of said sensory patches comprise of well-organized apical hair-like projections or the stereocilia facing the potassium-rich endolymphatic fluid in the labyrinth. Pressure waves within the endolymphatic fluid pivot the stereocilia, raising tension on the tip links between the stereocilia to open their ion channels leading to an influx of potassium ions. The base of these hair cells receive projections from the auditory nerve and information is carried from the peripheral sensory organ to the central nervous system, all the way up to the cortex, through a series of pathways connecting the central nervous system nuclei (Bissonnette and Fekete, 1996; Dallos et al., 1996;

Fischer, 1992; Hirokawa, 1978; Oesterle et al., 1992; Tanaka and Smith, 1978). Due to their synaptic transmission machinery, hair cells can be considered as neuron-like.

Hearing loss can be conductive, i.e., physical blockage or malformation of the outer or the middle ear, or sensorineural, i.e., damage or malfunction in the cochlea or the auditory pathway. While the former can often be fixed with surgical manipulation, loss of the hair cells or the tracts of the auditory pathways is irreparable (Dallos et al., 1996).

1.3.1 Inner ear development- from otic cup to a 3D labyrinth

During early embryogenesis in vertebrates, a narrow strip of ectodermal cells, called the pre-placodal domain, gives rise to several placodal organs, such as the lens of the eye, the olfactory pits, parts of the trigeminal ganglion, and the inner ear. The otic placode, that gives rise to the inner ear and its associated ganglion, is induced by Fgf signaling by the adjacent rhombomeres 4 and 5, and subsequent increased Wnt and Notch signaling (Jayasena et al., 2008; Ohyama et al., 2006). Pax2 expression is a classic marker of otic placode induction (Sanchez-Calderon et al., 2005; Singh and Groves, 2016). The placode then invaginates into the otic pit and then pinches off to form the fluid-filled otic vesicle. Delamination of cells from the ventromedial side of the otic vesicle gives rise to the sensory neurons of the statoacoustic ganglion (SAG) (Evsen et al., 2013; Fekete and Wu, 2002; Fritzsch et al., 2006). At the same time, an asymmetric activation of Wnt and Shh signaling in the otocyst is influenced by the opposing gradients in the adjacent neural tube. This leads to a dorsolateral to ventromedial subdivision of the inner ear epithelium. The dorsal subdivision becomes the vestibular part and the ventral subdivision elongates into the cochlear duct. Wnt misexpression at later stages of inner ear development can cause abnormal hyperproliferation and formation of vestibular-like patches (Jacques et al., 2014; Munnamalai et al., 2017; Stevens et al., 2003). Retinoic acid mediated signaling is important for anterior-posterior axis specification of the otocyst (Bok et al., 2011). Further morphogenesis influenced by Fgfs, Wnts and Bmps gives rise to the complex 3-dimensional labyrinth of the inner ear, that houses 6 to 8 sensory organs (Figure 1-1A; schematic of the avian inner ear). Each of the sensory domains can be identified by Bmp ligand expression at the early stages of morphogenesis, and Sox2 at later stages of development (Wu and Oh, 1996). Within the sensory patches, Notch signaling, specifically lateral induction, gives rise to the prosensory domains; and later on, lateral inhibition finesses the sensory patch into the mechanosensory hair cells (classically labeled by Atonal 1) and adjacent intermingled supporting cells (Groves and Fekete, 2012; Petrovic et al., 2014).

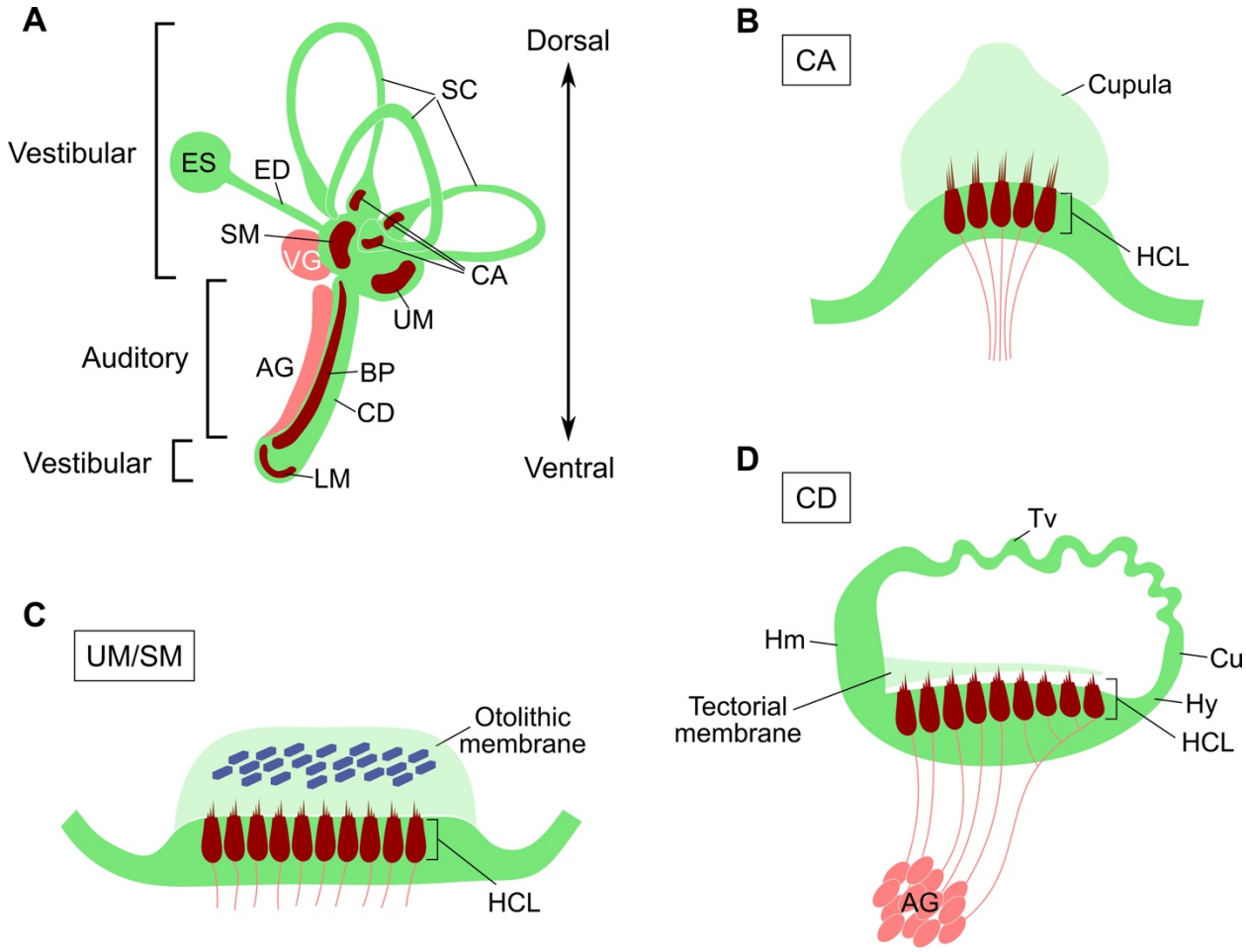

Figure 1-1 Schematics of the avian inner ear anatomy

A) The chicken inner ear labyrinth is represented in the schematic with sensory domains in dark red, associated ganglia in salmon color, and non-sensory tissue of the labyrinth in green. In panels (B-D) a cross section of each of the types of sensory organs shows the sensory domain with hair cells (dark red). B) Schematic of a crista with hair cell stereocilia embedded in the gelatinous cupula. C) Schematic of a macula with stereocilia embedded in the otolithic membrane with calcium carbonate crystals (in blue). D) Schematic of cross-section of the avian cochlear duct. Abbr.: AG, auditory ganglion; BP, basilar papilla; CA, crista ampullaris; CD, cochlear duct; Cu, cuboidal cells; ED, endolymphatic duct; ES, endolymphatic sac; HCL, hair cell layer; Hm, homogene cells; Hy, hyaline cells; LM lagenar macula; SC, semicircular canals; SM, saccular macula; Tv, tegmentum vasculosum; UM, utricular macular; VG, vestibular ganglion.

In humans, much of inner ear morphogenesis occurs between 4-10 weeks of fetal gestation (first trimester), after which the labyrinth grows in size for a couple of months. However, vestibular and auditory reflexes are not elicited until 19 and 24 weeks, respectively (Lim and Brichta, 2016). Comparable stages of mouse and chicken inner ear development are known. During this entire developmental process, several cell populations within the inner ear are neural progenitor-like; this includes maturing mechanosensory hair cells, immature neurons of the auditory and vestibular ganglion, and Sox2- or NeuroD-positive (neural progenitor markers) cells of the prosensory domain and SAG. These cell populations could be susceptible to the neurotropic ZIKV.

1.3.2 Dorsal compartment- semicircular canals, vestibule, and endolymphatic system

The dorsal compartment of the amniote inner ear, primarily housing vestibular organs, comprises of three orthogonal semicircular canals oriented to capture motion in three-dimensional space. A dilation (the ampulla) on one end of each of the canals houses a crista, with a bundle of hair cells and their stereocilia all pointing in the same direction. The cristae ampullaris (CA) detects angular acceleration of the head. The stereocilia are embedded in a cone-like cupula, a gelatinous mass (Figure 1-1B). When the fluid is flowing through the canal, the cupula moves and pivots the stereocilia and that opens ionic channels for electrical conduction to the vestibular pathway. The utricular and saccular maculae, or otolithic organs, detect linear acceleration (gravity) to assist with orienting the head in space. The macular hair cells have their stereocilia embedded in a gelatinous mass with calcium carbonate crystals, called the otolithic membrane (Figure 1-1C). The force of gravity or sudden changes in linear acceleration move the stereocilia, activating the mechanosensory ionic channels. Dorsal sensory organs in amniotes become distinguished structures and begin hair cell differentiation and maturation before the ventral (auditory) organs (Dallos et al., 1996; Lim and Brichta, 2016; Oesterle et al., 1992; Tanaka and Smith, 1978).

Medially, the labyrinth is connected to the endolymphatic sac via the endolymphatic duct. The endolymphatic sac is only partially embedded in the temporal bone and is conjectured to be the pressure-relief valve for the inner ear (Swinburne et al., 2018).

1.3.3 Ventral compartment- cochlea and lagena

The ventral part of the inner ear labyrinth of amniotes consists primarily of the cochlear duct housing the membranous auditory organ. The auditory organ is called the basilar papilla (BP) in the birds and is analogous to the mammalian organ of Corti. Unlike the spiraled cochlea of mammals, the avian auditory organ is a long sickle-shaped duct (Figure 1-1A). The mammalian

organ of Corti comprises of one row of inner hair cells (that take information to the brain via the afferent tracts) and three rows of outer hair cells (that bring feedback information from the brain to regulate auditory efficiency). The avian BP, however, has a gradient of hair cell morphology from the highly afferent-innervated tall hair cells (left side in Figure 1-1D) to the efferent-innervated short hair cells (right side in Figure 1-1D). Wnts and Bmps are known to play a role in patterning the radial axis of the avian cochlea. The stereocilia of the hair cells are embedded in the tectorial membrane to open the tip-link ion channels upon vibration of the BP. Amongst other non-sensory epithelial cell populations of the cochlear duct, the tegmentum vasculosum is highly vascularized and pumps K^+ ions into the endolymphatic fluid to maintain the highly positive potential across the sensory epithelium (Dallos et al., 1996; Lim and Brichta, 2016; Oesterle et al., 1992; Sienknecht and Fekete, 2008; Tanaka and Smith, 1978; Wu and Kelley, 2012).

At the ventral-most tip of the avian inner ear lies yet another vestibular-like sensory patch, the lagenar macula (LM), which is absent in most mammals. The function of the lagena is not very clear, although some evidence of its importance in geo-magnetic navigational abilities and a supplemental role to the saccular macula have been presented. Lagena is an otolithic organ, similar to the utricle and saccule (Khorevin, 2008; Oesterle et al., 1992; Tanaka and Smith, 1978).

1.4 Significance and Goals of the study

ZIKV can cause severe congenital defects in humans resulting in often irreparable damage and coordinated care as the primary treatment approach. With the rise in globalization and trade, diseases like ZIKV are not just restricted to the country of origin, as indicated by the 95% cases of ZIKV infection in the U.S. in the international travelers. Many tropical countries could still be at risk of infection by this mutated and rather more dangerous strain of the virus. Understanding the damage caused by ZIKV is the first step towards finding a cure or remedy.

From the congenital Zika syndrome case reports, we know that the developing brain and the inner ear are susceptible to ZIKV infection with strong indication of the peak of susceptibility at and just after the first trimester. We attempt to further elaborate the spatio-temporal infectability of target cell types in embryos not only to correlate the severity of developmental defects to the age of infection, but also to reveal potential hidden congenital abnormalities that are yet to be detected in clinical studies. To address these questions, we employed a model system with reduced biohazard risk, the self-contained *in ovo* chicken embryo. As a vertebrate, chicken embryo can

provide a higher-throughput and controlled experimental system to study the pathogenesis of ZIKV at early stages of development.

Several cellular and animal models present evidence that ZIKV preferentially infects neural progenitor cells and causes increased cell death and reduced proliferation. We initially assumed that **all accessible neural progenitor populations would be equally susceptible to infection in the early developing vertebrate brain, but this proved to be incorrect**. We explored ZIKV infection at early stages of brain development by injecting the chicken embryonic neural tube at embryonic day (E)2, as soon as the central nervous system primordium becomes a closed cavity. With this injection paradigm, the accessible pool of progenitors should be all those that line the brain ventricles; in other words, the cells of the ventricular zone. Briefly, we found that ZIKV not only infects the neural-progenitor-rich periventricular zone, but within the ventricular zone there are regions of preferential infection, or "hot-spots" of infection along the neuroepithelium; notably, some of these key regions are known to be morphogen-secreting signaling centers.

In addition to the ZIKV infection induced brain development defects, the spectrum of congenital ZIKV syndrome has been extended to chorioretinal atrophy and sensorineural hearing loss. Around 6% of newborns exposed prenatally to ZIKV presented with sensorineural hearing loss, perhaps originating in the inner ear, more specifically the cochlea. Furthermore, arguably due to more challenging brain defects, no evidence has been provided for vestibular dysfunction to our knowledge. Stages of inner ear organ development involve various neural-like cell populations that could be susceptible to ZIKV infection including immature neurons of SAG, the prosensory domains of inner ear sensory organs, and/or neural-like hair cells of those sensory organs. Interestingly, we found infection in the sensory cochlea several days after E2 brain injections (data not shown), further supporting the infectability of the inner ear. A key knowledge gap is to explore the spatial and temporal susceptibility of the developing inner ear to ZIKV infection. We attempted **to explore what inner ear cell types are most susceptible and prone to damage at each stage of infection**. One possibility is that neuronal and/or sensory progenitors might be preferred, considering the know neurotropism of ZIKV. Another possibility is that, like the neural tube, signaling centers of the inner ear might be preferred targets of ZIKV. We found that ZIKV injection into the chicken otic primordium on embryonic day (E)2 to 5 resulted in sensory epithelial infection in the vestibular and auditory organs frequently, with infection found in the basilar papilla (sensory cochlea) as late as E13. However, non-sensory tissues of the membranous labyrinth, and the periotic mesenchyme, were also frequent targets of ZIKV.

CHAPTER 2. MATERIALS AND METHODS

This section has been adapted from a first author publication.

Thawani A, Sirohi D, Kuhn RJ, & Fekete DM. (2018). Zika virus can strongly infect and disrupt secondary organizers in the ventricular zone of the embryonic chicken brain. *Cell Reports, 23(3),* 692-700.

2.1 Virus production, titration and injection into embryos

2.1.1 Zika virus (ZIKV)

The Zika virus strain used for chicken embryonic injections was originally obtained as a clinical isolate from French Polynesia (H/PF/2013) of the Asian lineage. At Dr. Richard J. Kuhn's lab at Purdue University, this strain was grown and titered on Vero cells (monkey kidney cells) obtained as a passage 2 stock from the lab of Dr. Michael S. Diamond at Washington University School of Medicine in St. Louis, Missouri, who obtained it as a passage 3 stock from Xavier de Lamballerie at Emergence des Pathologies Virales, Aix-Marseille Université, Marseille, France and the European Virus Archive Goes Global (EVAg). The virus stock was grown in the Kuhn lab and a passage 2 harvest of $9.6x10^7$ PFU/ml suspension was used for *in ovo* infections.

2.1.2 Dengue virus (DENV)

The Dengue-2 (DENV) strain was used as a non-neurotropic flaviviral control. The virus was obtained by Kuhn lab from CDC approximately 15 years ago and stock used in the experiments was a $5x10^7$ PFU/ml suspension collected from passage 4 in C6/36 mosquito cells.

2.1.3 Animal handling and injections

Fresh fertilized White Leghorn chicken eggs were purchased from the Poultry department at Purdue University Animal Sciences Research and Education Center. The eggs were incubated at 38^0C and high humidity for normal development and windowed at E2 for manipulation. The viral stock was mixed with 0.25% Fastgreen dye at a 9:1 ratio for visualization of viral spread under the microscope. For mock injections, chick ringer's solution (pH 7.4; 123.2mM NaCl, 1.56mM $CaCl_2$, 4.96mM KCl, 0.81mM Na_2HPO_4 in water) was mixed with 0.25% Fastgreen dye at a 9:1 ratio. A pulled glass micropipette with 10-12μm wide tip outer diameter (thin wall

borosilicate capillary glass tubing with filament- outer diameter 1.50mm, inner diameter 1.17mm) was attached to a positive displacement Picospritzer® II system (General Valve corporation) for *in ovo* injections. Rigorous Biosafety Level 2 (BSL2) precautions were observed while handling the virus and virus-infected tissue samples. For the brain injections, the inoculum was delivered directly to the midbrain (MB) at E2 and the viral suspension was observed to spread through the forebrain (FB) and hindbrain (HB) (refer to Chapter 3 for injection images). Direct inner ear primordium inoculations were performed at E2 [Hamburger-Hamilton stage (HH)13-14], E3 (HH16-18), E4 (HH20-23) and E5 (HH25-27), and tissue was thereafter harvested at 2, 4, 6, and 8 days post infection (dpi) for analysis (refer to Chapter 4 for injection images). The blood injections were performed at E3 by injecting the virus into the anterior carotid vein, the limb bud injections at E4 by infecting 5 different locations in the forelimb most accessible from the surface (usually right side), and the chorioallanotic membrane (CAM) infection by dispensing the virus over the CAM of E10 embryos (refer to Chapter 5 for injection images). Comparable stages of human development can be deduced with Carnegie staging (Table 2-1) (Butler and Juurlink, 1987).

Table 2-1 Carnegie staging to compare relevant chicken and human embryonic stages

Age of chick injection	**Carnegie staging**	**Weeks of human gestation**
E2	Stage 11	Week 4
E3	Stage 13	Week 4-4.5
E4	Stage 15	Week 5-5.5
E5	Stage 17	Week 6-6.5
E10	Stage 23	Week 8-8.5

A new micropipette with fresh cold viral suspension was mounted every 30 minutes to avoid the inoculum losing titer. Eggs were sealed with packing tape and returned to the incubator for further development. At the time of harvest, embryos were killed by removing them from the amnion, often followed by decapitation, and immersion in a fixative. The animals were staged using Hamburger and Hamilton staging system (Hamburger and Hamilton, 1992). No gender selection or separate analysis was employed as it is hard to distinguish genders this early in development. ZIKV-infected egg waste was directed for incineration through Stericycle®- a medical waste management company. All the injections and tissue processing of the chicken

embryos were performed according to NIH guidelines and policies established by Purdue University Animal Care and Use Committee.

2.2 Survival curve

Virus- or mock-injected embryo survival was recorded at the same time every day until E19-20, when they were terminated before the anticipated hatching at E21. Using Graphpad Prism software, a log-rank test was used to perform pair-wise statistical analysis of ZIKV or DENV survival curves compared to mock-injected controls.

2.3 Histology

2.3.1 Tissue processing and cryosectioning

For histological processing, whole embryos, embryo heads, or ear capsules were dissected and fixed in 4% paraformaldehyde in phosphate-buffered saline (PBS). They were then dehydrated with graded sucrose (10%, 20%, 30% sucrose in PBS; prepared with DEPC-treated water for RNAse-free conditions) and embedded in 300 bloom gelatin (for non-RNase-free conditions) or tissue freezing media (TFM®; General Data Company; for RNase-free conditions). The tissue blocks were frozen using liquid nitrogen and stored at -80^{0}C until cryosectioned. Depending on the tissue, 15 to 20µm thick sections were collected at -20 to -24^{0}C using a Leica® CM1900 cryostat and stored in a -20^{0}C or -80^{0}C freezer until histological processing. Two to ten sets of slides with alternate sections were generated in order to perform parallel staining on the same embryo sample.

2.3.2 Immunohistochemistry

For cryosections, tissue samples were embedded in 7.5% gelatin/15% sucrose in PBS or TFM® (General Data Company) and 20µm sections were collected. For whole mounts, live tissue was dissected to isolate intact brains that were then fixed, dehydrated by graded methanol solutions and stored at -20^{0}C in methanol.

Blocking solution with 5% of goat or horse serum in PBS was applied to reduce non-specific binding of the antibodies prior to antibody application. The primary antibodies used were dsRNA (1:500, J2, mouse IgG_{2a}, SCICONS), Sox2 (1:500, goat IgG[H+L], Santa Cruz, SC-17320), PAX6 (1:50, mouse IgG_1, deposited to the Developmental Studies Hybridoma Bank [DSHB] by

Kawakami, A.; DSHB Hybridoma Product PAX6), NKX2.2 (1:50, mouse IgG_{2b}, deposited to DSHB by Jessell, T.M./Brenner-Morton S.; DSHB Hybridoma Product 74.5A5), pH3 (1:200, rabbit IgG[H+L], Calbiochem), anti-NF70 (1:100, rabbit IgG[H+L] polyclonal raised against gel-purified chicken 70kD neurofilament protein, provided by Dr. Peter J. Hollenbeck, Purdue University), anti-NF (DSHB Hybridoma Product 3A10; 1:25 dilution from hybridoma cell supernatant, mouse IgG_1, hybridoma cells deposited to the DSHB by Jessell, T.M. / Dodd, J. / Brenner-Morton, S.), anti-HuC/HuD (1:50, mouse IgG_{2b}, ThermoFisher Scientific® A21271), anti-activated Caspase-3 (1:400, rabbit IgG[H+L], BD Biosciences 559565) and anti-Islet1/2 (1:50, mouse IgG_{2b}, deposited to DSHB by Jessell, T.M. / Brenner-Morton, S., DSHB Hybridoma Product 39.4D5). Fluorophore-tagged secondary antibodies (Life Technologies, 1:250 to 1:500 dilution), Lectin (1:400, *Lens culinaris* agglutinin, Vector laboratories), Phalloidin (1:250, Invitrogen), and nuclear label TO-PRO®-3 Iodide (642/661) (1:2000, Life Technologies) were added to the secondary antibody solution as needed.

TUNEL labeling was performed prior to immunohistochemistry using Roche *In Situ* Cell Death Detection Kit using the manufacturer's protocol with some modifications- 5 minutes of permeabilization in 0.1% TritonX, and 3-4 hours of labeling reaction. For diaminobenzidine (DAB) colorimetric stains on cryosections, after the primary antibody incubation, endogenous peroxidase activity was saturated with 0.3% H_2O_2 in methanol at -20^0C for 30 minutes after the primary antibody incubation. Biotinylated secondary antibody (1:250, horse anti-mouse IgG[H+L], Vector labs) was applied and the labelling was further amplified by avidin-biotin complex reaction with horseradish peroxidase (HRP) tagged to biotin (Vectastain ABC kit, Vector Laboratories). Slides were developed with 0.5mg/ml diaminobenzidine (DAB) with 0.06% H_2O_2 in 50mM Tris buffer (pH=7.4). For whole mount DAB staining, HRP-tagged secondary antibody (1:200, goat anti-mouse IgG[H+L]), Thermofisher Scientific) was used, followed by DAB oxidation reaction (Kawakami et al., 1997).

Images were acquired using Nikon Eclipse 90i (confocal imaging), Nikon Eclipse E800 (epifluorescence and DIC imaging) or Leica MZFLIII (stereomicroscope). For every slide stained with dsRNA, all the sections were thoroughly scanned to seek infection using the epifluorescence microscope. Selective images were then captured with confocal microscopy for better resolution. Post-processing of images was performed using ImageJ (NIH) by manipulating brightness and contrast to visualize the signal better; the same adjustment was applied to all the images for a specific marker to prevent bias.

2.3.3 In situ hybridization

The slides with cryosections were labeled with *in vitro*-transcribed digoxygenin (DIG)-labeled RNA-probe designed against chicken genes for *SHH, FGF8B, BMP7, PTCH1,* or *BMP4*. Plasmid stocks were maintained by transforming the plasmid into DH5α chemically competent cells followed by plasmid preparation of a selected antibiotic resistant colony using a midiprep kit (QIAGEN® Plasmid Midi Kit, 12143). Table 2-1 lists sources and transcription details for each plasmid used to transcribe the RNA probes. Linearized DNA was purified by phenol-chloroform extraction and transcribed with the respective anti-sense polymerase (Promega) using DIG-labelled nucleotides (Roche). The template strand was digested with RQ1 DNase (Promega) to leave only the RNA strands in the solution, which were precipitated with 0.05M LiCl in 100% Ethanol and eventually dissolved in 10mM Tris-EDTA or RNase-free water.

Table 2-2 In situ hybridization probes

Probe plasmid	Restriction enzyme (NEB)	Antibiotic resistance	Anti-sense polymerase (Promega)	Source
cBMP4^{+}	XbaI	Ampicillin	T7	Dr. Doris Wu, NIDCD
cBMP7	HindIII	Ampicillin	T3	Dr. Doris Wu, NIDCD
cFGF8B*	BamHI	Ampicillin	T7	Dr. Sumihare Noji, Univ. of Tokushima, Japan
cPTCH1	KpnI	Ampicillin	T3	Dr. Doris Wu, NIDCD
cSHH	HindIII	Ampicillin	T3	Dr. Doris Wu, NIDCD

$^{+}$Probe prepared and in situ hybridization run by Adam Lorch, Fekete laboratory (08/2018)
*Plasmid stock prepared by John Brigande, Fekete laboratory (02/2000)

This in-situ hybridization protocol has been adapted by the Fekete lab from Sanchez-Hidalgo's group (Sanchez-Calderon et al., 2005). In summary, after drying the slides, the tissue sections were briefly digested with Proteinase K (1µg/ml) for permeabilization and re-fixed with 4% paraformaldehyde. Acetylation with acetic anhydride and 0.1M triethanolamine was performed to avoid non-specific binding of negatively charged probes to the slides and the tissue. The probe was briefly heat-denatured and dissolved in hybridization buffer [10% Dextran sulfate, 50% Formamide, 1mg/ml dissolved yeast torula RNA, 1X Denhart's solution (50X stock, VWR), 1X in-situ salt solution (0.3M NaCl, 9mM Tris HCl, 1.2mM Tris base, 5mM NaH_2PO_4, 5mM

Na_2HPO_4, 5mM EDTA)]. After 2 hours of pre-exposure with the hybridization solution, the slides were exposed to 1mg/ml of probe dissolved in hybridization buffer for an overnight treatment at 72^0C. The slides were washed with saline-sodium citrate buffer and PBS several times, and anti-DIG Fab fragments (1:3500, Roche) conjugated with alkaline phosphatase dissolved in blocking solution (2% Roche blocking reagent, 10% fetal bovine serum, 0.1% Tween20 in PBS) was then used to amplify the signal overnight. On the third day, pretreatment with alkaline phosphatase buffer (100mM Tris pH 9.5, 100mM NaCl, 50mM $MgCl_2$), a nitro-blue tetrazolium dye solution at pH9.5 (SigmaFast™ BCIP/NBT tablet, Sigma-Aldrich) was used as a colorimetric detection method for alkaline phosphatase enzyme leading to an insoluble purple precipitate.

PAX6-DAB labeling, described in section "Immunohistochemistry", was executed subsequently on *SHH*-labeled sections and NKX2.2-DAB labeling on *PTCH1*-labeled sections. For *PTCH1, BMP7* and *FGF8B*, an observer blinded to treatment condition was provided with a set of template images from a control embryo. They then classified each sample region from additional embryos as showing signal intensity that was similar to, or weaker than, the control templates.

Images were acquired using Nikon Eclipse 90i (confocal imaging), Nikon Eclipse E800 (epifluorescence and DIC imaging) or Leica MZFLIII (stereomicroscope). Post-processing of images was performed using ImageJ (NIH) by manipulating brightness and contrast to visualize the signal better; the same adjustment was applied to all the images for a specific marker to prevent bias.

2.4 Quantitative Real-Time Polymerase Chain Reaction (qRTPCR) and Polymerase Chain Reaction (qRTPCR)

Whole or half brains and whole (E3-4) or apical (older than E4) heart samples were collected for RNA isolation by dissolving the tissue in TRIzol™ Reagent (Invitrogen™). Pheno-chloroform extraction was performed to isolate the RNA, followed by RQ1 DNase (Promega) treatment and purification with Qiagen RNAeasy® mini kit. qRTPCR was performed using SuperScript® III Platinum® SYBR® Green One-Step qPCR Kit w/ROX (Thermofisher Scientific) kit and primers: 5'-CCGCTGCCCAACACAAG-3' and 5'-CCACTAACGTTCTTTTGCAGACAT-3'. Each of the samples was run in triplicate reactions and optimized with the same total RNA weight across the samples. The derived C_t values were converted to the number of ZIKV RNA molecules per 100ng of total RNA using a standard curve

created using *in vitro* transcribed RNA from the ZIKV cDNA (FSS13025 strain) clone (Shan et al., 2016). In separate PCR reactions, the extracted RNA optimized for the same total RNA weight across the samples was amplified with the ZIKV genome primers (expected amplicon ~700bp) and with primers for GAPDH (Glyceraldehyde 3-phosphate dehydrogenase) as the housekeeping gene (expected amplicon ~150bp); GAPDH primers (designed by M. Katie Scott, Fekete lab): 5'-TTGGCATTGTTGAGGGTCTT-3' and 5'-GTGGACGCTGGGATGATGTT-3'. Amplified products were loaded on a 2% agarose gel for electrophoresis. The qRTPCR protocol and PCR amplification from the extracted RNA was performed by Dr. Devika Sirohi (Dr. Richard Kuhn's lab), who was provided samples decoded for experimental condition and age of harvesting in order to avoid bias.

2.5 Paint-filling inner ears

Embryo heads harvested post infection were fixed in Bodian's fix (75% 190-proof ethanol, 5% formalin, 5% glacial acetic acid, 15% water), processed through increasing gradients of ethanol (75%, 95% and 100%) and cleared in 100% methyl salicylate for at least several hours. White gloss enamel paint (1%; The Testor Corporation) in methyl salicylate was sonicated for homogenizing and loaded onto a glass micropipette connected to a motorized Stoelting microsyringe pump with the tubing filled with heavy mineral oil to avoid compressing air (Bissonnette and Fekete, 1996; Kiernan, 2006). The protocol for delivering paint into the fluid compartment of the inner ear is described in detail in Bissonnette and Fekete (1996) and Kiernan (2006). We performed this experiment on E2 ear injected embryos at 6dpi (E8). After paint-filling both the ears, the heads were stored in methyl salicylate for one night or more before imaging. The heads were cut along the sagittal axis and imaged using a Leica MZFLIII stereomicroscope. As described above, ImageJ or FIJI was used for image post-processing if required.

2.6 Image quantification

2.6.1 External brain size quantification for microcephalic phenotype

Embryos injected with ZIKV suspension at E2 were harvested as whole embryos (3dpi) or dissected brains (7dpi). For 3dpi harvests, left and right sides of the fixed whole embryo were imaged on a Leica MZFLIII stereomicroscope with a Spot digital camera. At such early ages, the embryo sizes differ significantly from one stage to the next; therefore, the analysis was restricted

to HH stage 26 to 27. One stage 26 embryo from a ZIKV-injected group was removed from the analysis because it presented with one eye significantly smaller than the other and similar defects are occasionally observed in control embryos. For 7dpi harvests, fixed whole brains were removed and imaged from a dorsal view. After the regions of interest were identified, ImageJ was used for conducting brain dimension measurements (projected areas and widths), with appropriate scaling calibrations, by an investigator who was blinded to the experimental group. The total dimensions (left and right sides) were combined. Only for 7dpi wet weight measurements, the investigator was not blinded.

2.6.2 Magnetic Resonance Imaging

MRI scanning was done on selected fixed 7dpi brains using the 7T Bruker Biospec 70/30 USR small animal scanner with a true fast imaging with steady-state precession (TrueFISP). Fixed and washed 7dpi brains were embedded in 4% gelatin in PBS and scanned in a 16mm x 16mm frame using a surface coil receiver with 0.275mm slice thickness. A middle slice along the dorsal-ventral axis through the FB and MB was used for length measurements (ImageJ, NIH). Using "Measure Stack" plugin, the volume of the MB ventricle was determined. "Volume viewer" plugin was used to obtain a tricubic interpolated X-Z cross-section through the MB for mesencephalic nuclei thickness measurement.

2.6.3 Morphometric analysis of midbrain histology

To quantify *SHH*, PAX6 and NKX2.2 domains, double-labeled alternate sections of either *SHH*-PAX6 or *PTCH1*-NKX2.2 were imaged using a 20X lens (numerical aperture=0.75) on a brightfield microscope (Nikon Eclipse E800). Colorimetric *SHH*-PAX6 stains were channel-separated by deconvolution on ImageJ. One or two middle sections of the MB basal plate were imaged for left and right sides separately. The same data collection method was used for an adjacent set of sections co-labeled with *PTCH1*-NKX2.2. Pixels numbers for *SHH*, PAX6 and NKX2.2 were quantified using auto local thresholding. The distances from the midline of the lateral boundaries of PAX6 and NKX2.2 domains were measured in ImageJ using a calibrated line tool.

2.6.4 Cell death quantification

TUNEL quantification was performed using ImageJ (NIH). High resolution images were captured using a 20X lens (numerical aperture=0.75) on a confocal microscope. The MB basal

plate was analyzed by quantifying 3 to 4 middle sections of the domain. ZIKV-infected embryos were selected for the analysis only if the MB basal plate was considered strongly infected. Approximately 75µm from the midline a box of 160µm x 160µm was cropped with one edge of the box aligned with the ventricular surface. TUNEL-positive pixels in the field of interest were measured by thresholding using a pre-determined pixel intensity cut-off value. The measure was averaged over the 3 to 4 sections and represented as the percentage of the total area evaluated.

Activated-caspase-3 signal quantification was performed using ImageJ (NIH). Three sections (sampled every other section) through the middle of the left and right stato-acoustic ganglia were imaged using a confocal microscope with a 10X lens (numerical aperture=0.45). For animals that received ZIKV injections, each ganglion was evaluated for strength of infection based on dsRNA co-labeling and assigned to the uninfected or infected groups. Controls obtained from uninjected animals were analyzed separately. Activated-caspase positive pixels were measured in the stato-acoustic ganglion by cropping out the area and thresholding the activated-caspase signal using a pre-determined pixel intensity cut-off. The measured values were summed across the three middle sections, normalized for the cross-sectional area of the ganglion for those sections and represented as caspase pixels per unit area.

2.7 Statistics and Graphical data analysis

Scatterplots and survival curves were prepared using Graphpad Prism. Convex hull plots were prepared using RStudio. Statistical Analysis Software (SAS) was used for generating averaged data summaries from raw data points for *SHH*-PAX6 and NKX2.2 quantification. Unpaired Mann-Whitney t-test without assuming the data exhibits Gaussian distribution was performed for statistical analysis of brain size comparisons. For *SHH*, PAX6, and NKX2.2 individual measurement statistical analyses, a mixed effects model was used in SAS with random effect terms to account for correlation between the left and right data points recorded from each embryo. A one-tailed t-test was performed for every measure with the hypothesis that ZIKV causes microencephaly (smaller brains) and reduced genetic markers (*SHH*, PAX6, NKX2.2), except ventricular volumes when two-tailed t-test was used because the expected direction of change in ventricular volume was unknown. MANOVA (Multivariate ANOVA) test was used in SAS for *SHH*-PAX6 and *SHH*-NKX2.2 convex hull plot quantification. Two-way ANOVA test was used for qRTPCR statistical analysis after brain injections, and for trends of infection in 3D histograms after inner ear injections. Log-rank test was used for survival curve analysis. Trends of infection

and 3D histograms after the inner ear infection were built using Microsoft Excel. One-way ANOVA (non-parametric) test was used for activated-caspase analysis.

2.8 Image processing and compilation

ImageJ or Fiji (NIH open source software) were used for image processing and quantification. Adobe® Photoshop® (*.psd files) or Inkscape (*.svg files; a free and open-source graphics software) were used to compile and design data figures.

CHAPTER 3. ZIKA VIRUS PATHOGENESIS IN THE DEVELOPING BRAIN

This section is a version of a first author publication.

Thawani A, Sirohi D, Kuhn RJ, & Fekete DM. (2018). Zika virus can strongly infect and disrupt secondary organizers in the ventricular zone of the embryonic chicken brain. *Cell Reports, 23(3),* 692-700.

3.1 ZIKV infection of neural progenitors correlates with neurodevelopmental disorders

Over 60 years after the Zika virus (ZIKV) was first suspected to infect humans (Dick, 1952; Dick et al., 1952), this *Aedes* mosquito-transmitted flavivirus was linked to increased incidences of severe brain defects in fetuses and Guillain Barré syndrome in adults (do Rosario et al., 2016; Rasmussen et al., 2016). ZIKV infection during fetal development causes 'Congenital Zika Syndrome' that can present with microencephaly, ventriculomegaly, ocular defects, hearing loss, orthopedic contractures and intra-uterine growth retardation (de Paula Freitas et al., 2016; Melo et al., 2016; Moore et al., 2017).

Animal models show persistence of ZIKV in the adult brain and testes (Dowall et al., 2016; Lazear et al., 2016). Neural progenitors of the central nervous system are particularly susceptible to infection in the adult murine cerebral cortex, in human embryonic brain organoids, as well as in the developing brains of murine and non-human primates (Li et al., 2016a; Li et al., 2016b; Miner et al., 2016a; Wu et al., 2016; Yockey et al., 2016). ZIKV infection reduces proliferation and increases cell death of neural stem cells. Ensuing neural defects, like cerebral cortical hypoplasia, glial lesions and overall embryonic growth restriction, culminate with microencephaly and a higher incidence of fetal lethality (Adams Waldorf et al., 2016; Li et al., 2016a; Miner et al., 2016a; Wu et al., 2016; Yockey et al., 2016). Furthermore, ZIKV host range was extended to the chicken embryo, where ZIKV was shown to impede brain development and cause ventriculomegaly and embryonic lethality (Goodfellow et al., 2016).

Detailed information about regional specificity for ZIKV infectivity within the early developing brain is currently a knowledge gap. **In this study, we exploited the ease of spatiotemporal access in the chicken embryo to explore whether neural progenitors throughout the early developing brain are equally susceptible to ZIKV infection.** According to the prosomere model, the embryonic brain is composed of individual anteroposterior (A-P)

neuromeres (or brain segments) that are further subdivided into dorsoventral (D-V) compartments. Some of these smaller compartments, or the boundaries between them, are the source of secreted factors (morphogens) that regulate brain patterning from a distance (Echevarria et al., 2003; Puelles and Rubenstein, 2015; Wurst and Bally-Cuif, 2001). By mapping ZIKV infection in different segments of the early developing brain, we identified 'hot-spots' of infection at specific neuromeres or neuromere boundaries, many of which are known signaling centers. Three such sites were shown to exhibit reduced morphogen expression when heavily infected, and one is further demonstrated to be accompanied by neural patterning defects. Thus, infection of neuromeres by ZIKV raises the possibility of broader, non-cell-autonomous misregulation in brain development.

3.2 Results

3.2.1 ZIKV replicates in chicken embryos and causes lethality

Embryonic day (E)2 chicken embryos were injected with 10-20nl of ZIKV ($9.6x10^7$ plaque-forming units (PFU)/ml) delivered to the midbrain (MB) ventricle (Figure 3-1A). The inoculum spread to the forebrain (FB), MB and hindbrain (HB) ventricles and often entered the anterior spinal cord (Figure 3-1B). All ZIKV-injected animals died by 15 days-post-infection (dpi; 3-4 days before the anticipated hatching), whereas 70% of the mock-injected controls survived until 17dpi, when they were terminated; median age of survival was 7dpi (Figure 3-1C). In contrast, survival from infection with a non-neurotropic phylogenetic neighbor of ZIKV, DENV, was no different from controls ($p=0.35$) (Weaver et al., 2016).

By 3dpi, the MB and/or FB were visibly smaller in ZIKV embryos compared to stage-matched controls (Figure 3-1D), although the penetrance of microencephaly was variable for both the telencephalon (TE; anterior FB) and the MB lobes (statistical assessment to follow). To assess ZIKV infection and replication, quantitative Real Time PCR (qRTPCR) was performed. ZIKV genomic RNA amplified above the baseline from brains at 1dpi and from heart by 2dpi (Figure 3-1E). In both organs, ZIKV RNA levels peaked around 3dpi, dropped about 30- to 100-fold at 5dpi, and leveled off at 7dpi. Thus, we chose to further explore the phenotype at two time-points: the approximate peak of viral load (3dpi) and median age of survival (7dpi).

Figure 3-1 Chicken embryos are permissive to ZIKV, resulting in a lethal infection

A) Schematic depicting the timing (red arrowhead) of virus (Z) or mock injections and days (3 and 7dpi, black and grey arrowheads) of histological analysis. B) ZIKV inoculum (green hue) into the MB ventricle on E2 spreads to the FB and HB ventricles. C) Survival curves for ZIKV, recorded daily, for 10 mock-injected controls, 15 ZIKV, 14 DENV (Log-rank test). D) At 3dpi, the MB diameter (yellow arrows) was smaller in ZIKV-infected embryos. E) qRTPCR shows the time course of ZIKV viral RNA load in both brain and heart (n=3 to 7 embryos; Two-way ANOVA; time is also a statistically significant factor by ANOVA). Bar represents the mean. Abbr: FB, forebrain; HB, hindbrain; MB, midbrain; TE, telencephalon; Z, ZIKV. (***=$p<0.001$, n.s.=not significant).

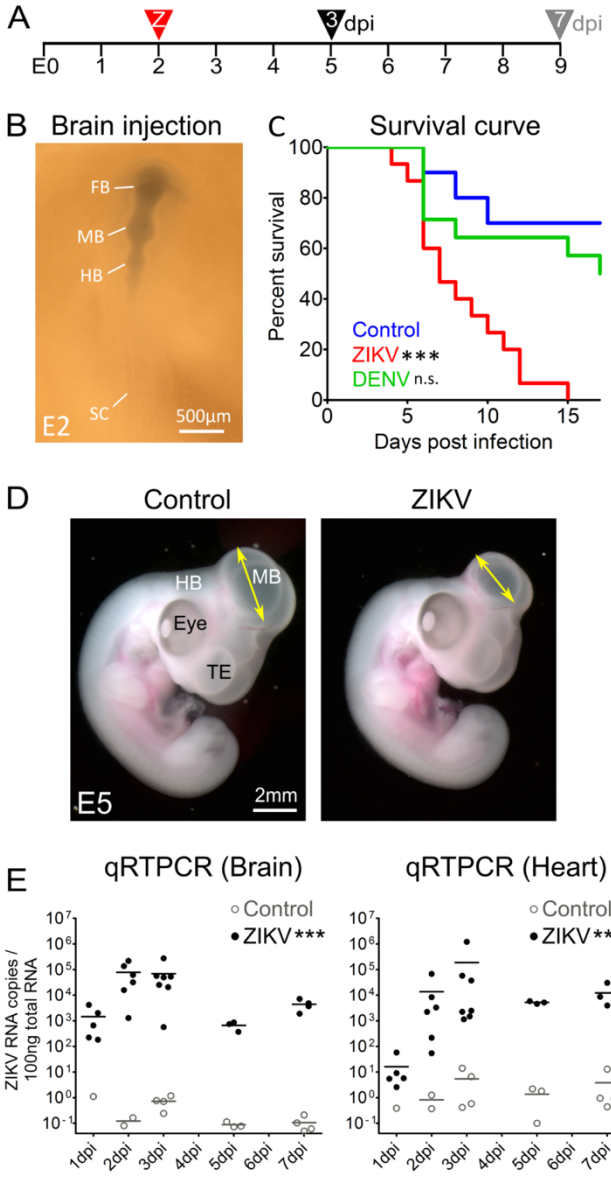
A
Z
3dpi
7dpi
E0 1 2 3 4 5 6 7 8 9
B Brain injection
FB
MB
HB
SC
E2
500µm
C Survival curve
Percent survival
100
80
60
40
20
0
0 5 10 15
Days post infection
Control
ZIKV***
DENV n.s.
D
Control
ZIKV
HB
MB
Eye
TE
E5
2mm
E
qRTPCR (Brain)
qRTPCR (Heart)
Control
ZIKV***
ZIKV RNA copies / 100ng total RNA
1dpi 2dpi 3dpi 4dpi 5dpi 6dpi 7dpi

3.2.2 ZIKV infection reduces the size of developing brain within 3dpi

The TE and MB areas measured from a lateral projection were reduced by 14% and 16%, respectively, at 3dpi (Figure 3-2A). Microcephaly in human infants is measured by head circumference, with 'severe' phenotype being over 3 standard deviations below the mean for a specific age (Ashwal et al., 2009). Using similar criteria for the projected area measurements, 25% of 3dpi embryos showed a severe reduction in brain size (MB and TE).

By 7dpi, the surviving ~50% of embryos displayed gross morphological abnormalities such as pale epidermis, focal depigmentation in the eye, brain hemorrhages and/or thoracoabdominal schisis (heart, liver, stomach, intestines outside the body cavity) (data not shown). Average brain wet weight was decreased by 7.6% (Figure 3-2B). Likewise, the total projected brain area (FB+MB) measured from a dorsal view was 8.3% smaller (Figure 3-2B). Over one-third (36%) of 7dpi embryos displayed a severe reduction in brain size (MB+FB).

We used Magnetic Resonance Imaging to ask whether ZIKV infection reduces neuroepithelial thickness or enlarges brain ventricles in the chicken embryo, as it does in humans (Moore et al., 2017). The 5 most severely affected 7dpi ZIKV brains (from a total of 11) were selected for comparison to 5 randomly selected controls. The average thickness of the TE nuclei was reduced by 15% in ZIKV brains. However, there was no significant change in MB ventricular volume (the site of injection); the variability across ZIKV samples was high (Figure 3-2C). Figure 3-3 presents several additional brain measurements at 3 and 7dpi.

Figure 3-2 ZIKV infection causes microencephaly in embryonic chicken brain

A) Projected brain areas were measured from images of 3dpi whole embryos for the TE area (i) and the MB (ii) area (Figure 3-3A, areas 2 and 3; n=10 controls, 8 ZIKV). B) At 7dpi, brain wet-weight was determined (i) and then images were used to measure the combined projected brain areas (ii) (Figure 3-3B, area 6; n=10 controls, 11 ZIKV). C) MRI scans of fixed 7dpi brains were used to measure TE epithelial thickness (i) and MB ventricle volume (ii; two-tailed t-test) (Figure 3-3C, measure 12 and 15; n=5 controls, 5 ZIKV). (one-tailed Mann-Whitney test; **=$p<0.01$, *=$p<0.05$, n.s.=not significant). Error bars represent mean ± SEM. Abbr: V, ventricle and see Figure 3-1. See also Figure 3-3.

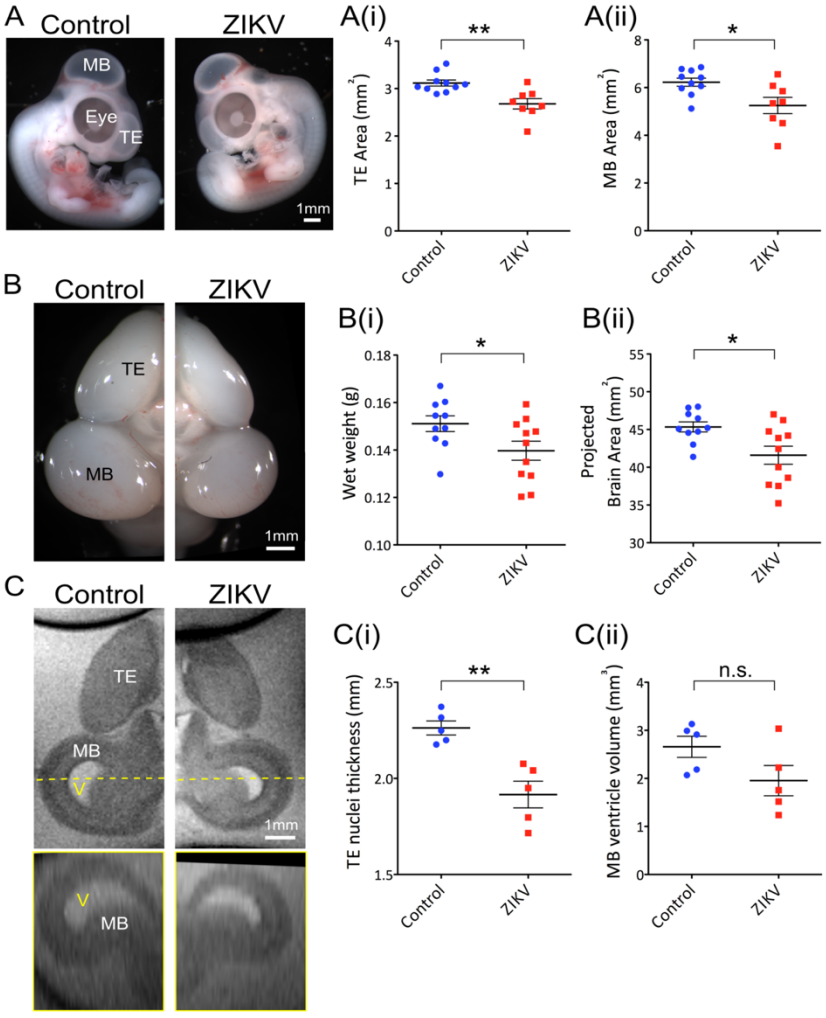
A
Control
ZIKV
MB
Eye
TE
1mm
A(i)
**
TE Area (mm²)
Control
ZIKV
A(ii)
*
MB Area (mm²)
Control
ZIKV
B
Control
ZIKV
TE
MB
1mm
B(i)
*
Wet weight (g)
Control
ZIKV
B(ii)
*
Projected Brain Area (mm²)
Control
ZIKV
C
Control
ZIKV
TE
MB
V
1mm
V
MB
C(i)
**
TE nuclei thickness (mm)
Control
ZIKV
C(ii)
n.s.
MB ventricle volume (mm³)
Control
ZIKV

Figure 3-3 Quantification of brain regions

All measurements were obtained from images using ImageJ software as described in the Materials and Methods chapter. A) In 3dpi embryos (n=10 mock controls; 8 ZIKV), area measurements were taken for the eye (#1), MB (#2), and TE (#3). Widths (#4, #5) were defined as largest diameter of each brain compartment. B) In 7dpi dissected brains (n=10 mock controls; 11 ZIKV), three areas were measured: total brain (FB+MB; #6), TE (#7) and MB (#8). Width diameters (#9, #10) were measured for each brain compartment and TE+MB length (#11) was measured as a straight line along the midline joining A-P vertices of the total brain area trace (#6). C) In MRI scans of 7dpi dissected brains (n=5 per condition), a middle slice of the MB from the MRI scan stack was chosen for linear measurements. The thickness (largest measure) of the TE nuclei structures (#12), MB cortical structures (#13) and mesencephalic nuclei (#14) were measured. The lateral ventricles of the TE were insufficiently resolved to ensure accurate delineation, so outlines of the MB ventricles across several sections were used as a measure of MB ventricular volume (#15). Error bars represent mean ± SEM. Abbr: TE-telencephalon, MB-midbrain, FB-forebrain, V-ventricle.

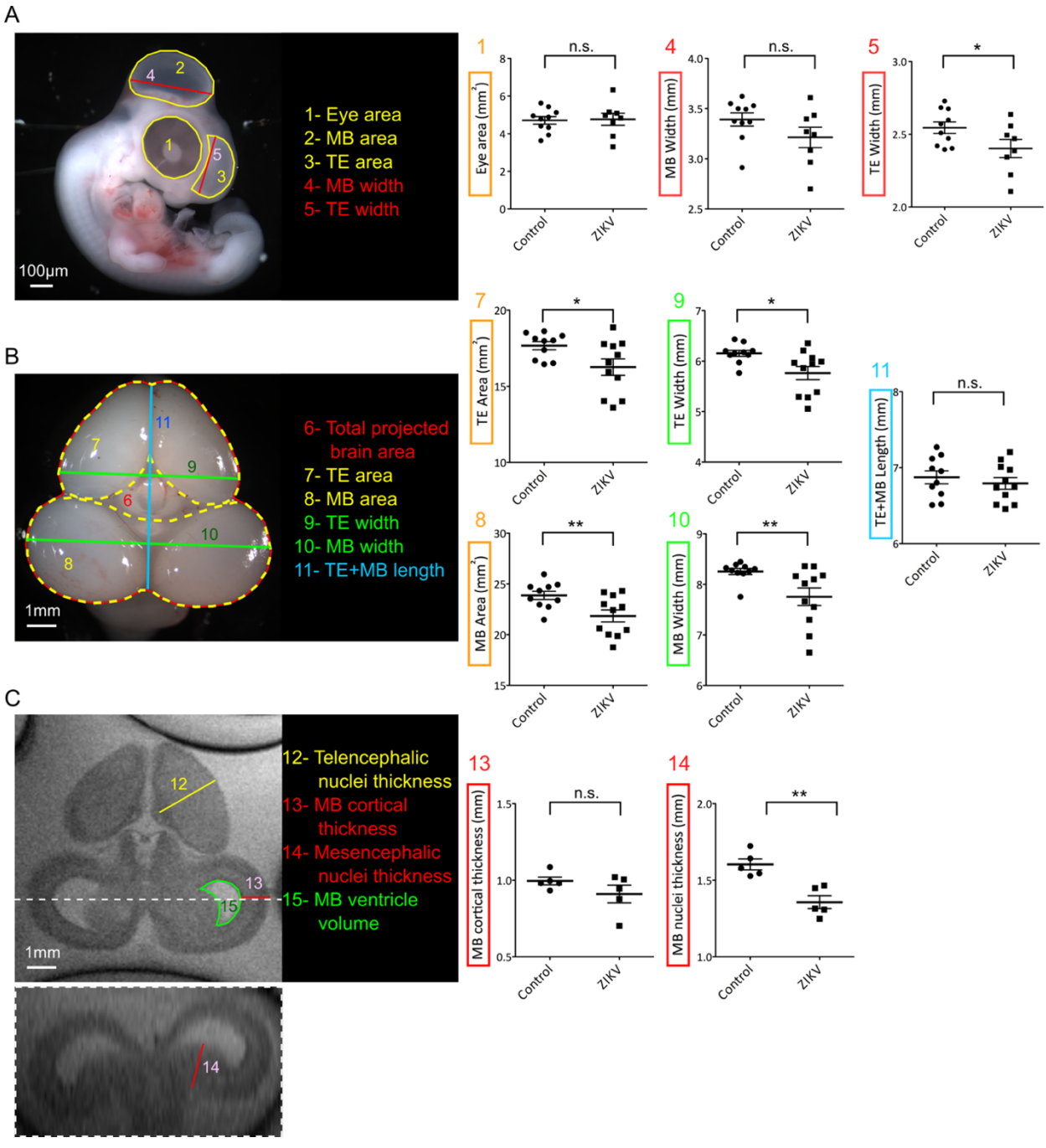
A
1- Eye area
2- MB area
3- TE area
4- MB width
5- TE width
100µm
B
6- Total projected brain area
7- TE area
8- MB area
9- TE width
10- MB width
11- TE+MB length
1mm
C
12- Telencephalic nuclei thickness
13- MB cortical thickness
14- Mesencephalic nuclei thickness
15- MB ventricle volume
1mm
Eye area (mm²)
MB Width (mm)
TE Width (mm)
TE Area (mm²)
TE Width (mm)
TE+MB Length (mm)
MB Area (mm²)
MB Width (mm)
MB cortical thickness (mm)
MB nuclei thickness (mm)
Control
ZIKV
n.s.
*
**

3.2.3 ZIKV shows a preference for specific neuromeres and neuromere boundaries

The localization of ZIKV infection throughout the embryonic brain was done using tissue sections. ZIKV+ cells were labeled with the J2 antibody directed against double-stranded RNA (dsRNA), which is abundantly produced in flavivirus-infected cells (Weber et al., 2006). We expected to find relatively uniform infection in the brain periventricular regions at the early stage of E5 (3dpi), especially in the MB and TE, given their reduced size (Figure 3-2 and 3-3). Instead, there appeared to be a strong preference for ZIKV to infect a few specific regions of the developing brain. Strong dsRNA labeling, or 'hot-spots' of infection, were found repeatedly at certain neuromere boundaries and brain subregions (Figure 3-4A, 3-5A, Table 3-1). To better map the ZIKV+ foci, we labeled adjacent sections for the evolutionarily-conserved genoarchitectural markers, SHH and PAX6 (Ferran et al., 2008; Wurst and Bally-Cuif, 2001). An exemplar specimen shows high ZIKV infection in the hypothalamus, thalamic roof plate, basal plate of the diencephalon (DE) and MB, pretectum, and MB-HB boundary (Figure 3-4B, red arrows). For a more holistic view of the ventricular/periventricular zone, Figure 3-5B shows a bisected 3dpi brain, with robust dsRNA labeling in the pretectum, MB basal plate, MB-HB boundary and hypothalamus. Figure 3-5C shows a summary schematic for recurrent regions of infection. Additionally, other regions of the brain and spinal cord show sporadic infection. Scattered dsRNA labeling in the head mesenchyme and the rest of the body lacked overt spatial preferences (Figure 3-4B).

Figure 3-4 ZIKV preferentially infects and abates key signaling centers in the developing brain at 3dpi

A) Qualitative analysis of infection at 3dpi is summarized in the schematic (n=15). Each row represents an embryo injected with ZIKV at stage (s)11 or 12. B) Alternate sections from a 3dpi ZIKV-infected embryo (Embryo# 1 in panel A) stained for PAX6 (brown), SHH (purple) and dsRNA; this example is representative of n=10 embryos. Some ZIKV infection hot-spots are labeled with arrowheads. Relative dorsal-ventral position is indicated by the percentile. Red bracket at 39% shows a peculiar crenellation defect of the neuroepithelium (40% occurrence). Red circle at 69% marks a hemorrhage reflecting DAB pigment oxidation by endogenous peroxidase in red blood cells. C, D) At the MB midline, SHH expression is weaker where ZIKV infection is heavy. PTCH1, a gene downstream of SHH, is also weaker in expression. Magnified views in the flanking red panels. E) PAX6+ pixel count was not changed by ZIKV infection. F) The PAX6+ population develops closer to the midline in ZIKV-infected embryos, possibly due to reduced SHH signal (SHH pixels) (one-tailed mixed effects SAS model). Left and right sides of each embryo are plotted independently. G) Convex hull plot of PAX6 lateral edge against number of SHH pixels show ZIKV data in the lower left quadrant of the plot (MANOVA). H-I) Although the NKX2.2 population does not show a statistically significant difference in the position of the domain; the convex hull plot shows the cloud of ZIKV data in the lower left quadrant. (***=$p<0.001$, **=$p<0.01$, *=$p<0.05$, n.s.=not significant). Error bars represent mean ± SEM. Abbr: AP, alar plate; A, anterior; BP, basal plate; D, dorsal; FP, floor plate; Hypo, hypothalamus; L, lateral; MHB, MB-HB boundary; PreT, pretectum; Pth, prethalamus; P, posterior; RP, roof plate; Th, thalamus and see Figure 3-1. See also Figure 3-5, Table 3-1.

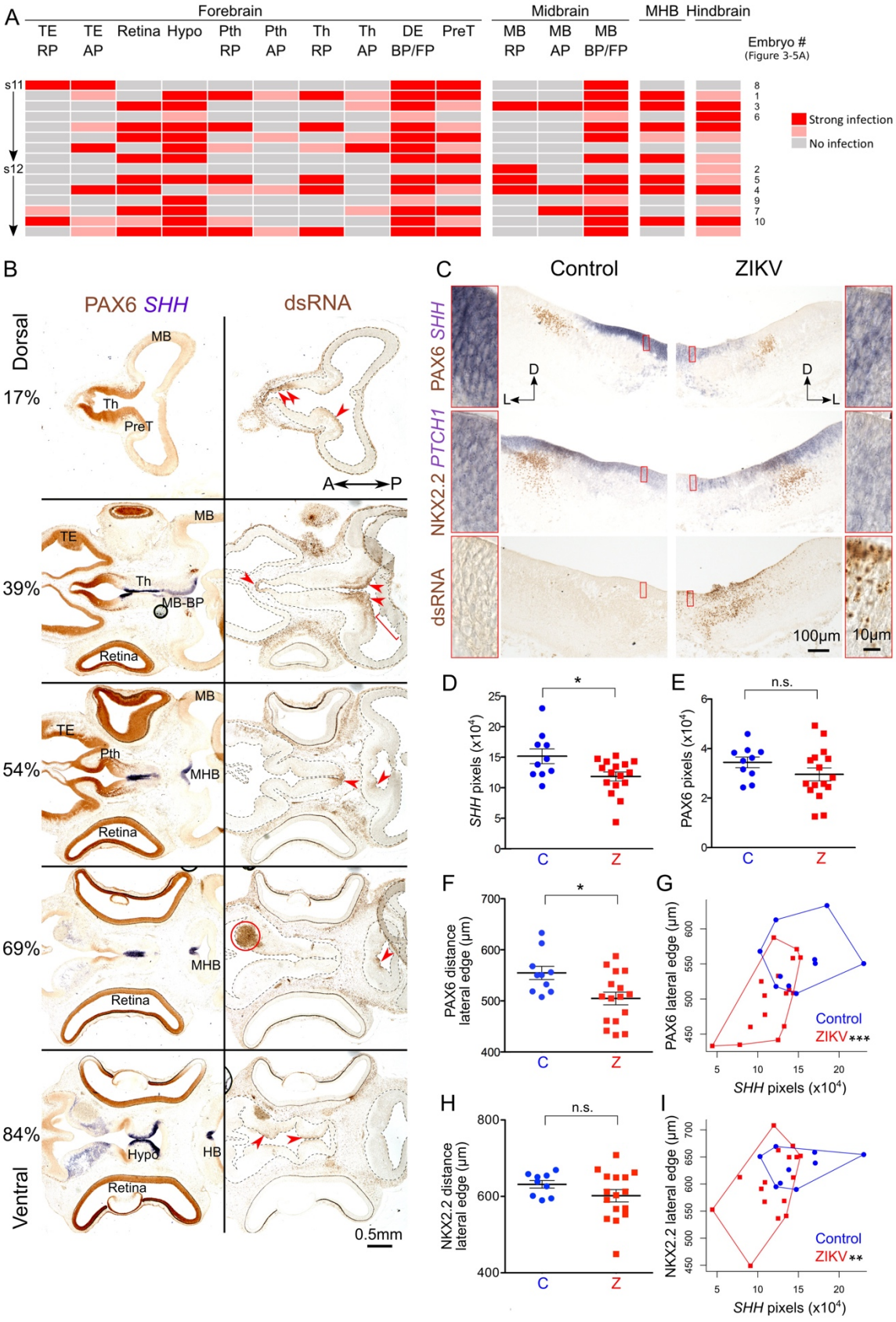
A
Forebrain
Midbrain
MHB
Hindbrain
TE RP
TE AP
Retina
Hypo
Pth RP
Pth AP
Th RP
Th AP
DE BP/FP
PreT
MB RP
MB AP
MB BP/FP
Embryo #
(Figure 3-5A)
s11
s12
8
1
3
6
2
5
4
9
7
10
Strong infection
No infection
B
PAX6 SHH
dsRNA
Dorsal
17%
39%
54%
69%
84%
Ventral
MB
Th
PreT
TE
MB-BP
Retina
Pth
MHB
Hypo
HB
A
P
0.5mm
C
Control
ZIKV
PAX6 SHH
NKX2.2 PTCH1
dsRNA
D
L
100µm
10µm
D
*
SHH pixels (x10^4)
C
Z
E
n.s.
PAX6 pixels (x10^4)
F
*
PAX6 distance lateral edge (µm)
G
PAX6 lateral edge (µm)
Control
ZIKV***
SHH pixels (x10^4)
H
n.s.
NKX2.2 distance lateral edge (µm)
I
NKX2.2 lateral edge (µm)
Control
ZIKV**
SHH pixels (x10^4)

Table 3-1 Summary of regions of infection in 3dpi ZIKV-injected embryos

Magnification	#Embryos with infection (n=15)	#Embryos with robust infection (n=15)
Diencephalon (basal plate)	93%	80%
Midbrain (basal plate)	87%	73%
Hypothalamus	80%	73%
Retina	60%	53%
Pretectum	80%	47%
Midbrain-hindbrain boundary	53%	47%
Hindbrain	80%	33%
Thalamus (roof plate)	40%	33%
Prethalamus (roof plate)	47%	27%
Midbrain (roof plate)	27%	27%
Telencephalon	47%	20%
Midbrain	20%	20%
Telencephalon (roof plate)	20%	13%
Thalamus	33%	7%
Prethalamus	27%	0%

The table is rank-ordered by the percentage of embryos with domains of strong infection in each region. Grey rows represent regions overlapping with presumed secondary organizers at this stage of development.

Figure 3-5 ‘Hot-spots’ of ZIKV infection observed in 3dpi brains

A) Comparable sections stained with dsRNA for multiple embryos show repeatability of the ‘hot-spots’ of infection observed. Strong infection of thalamic roof plate, MB basal plate and MB roof plate is indicated with blue, red and black arrowheads, respectively. Due to slight differences in the angle of sectioning and the range of sections we have stained for each embryo, certain regions of infection indicated in Figure 3-4A are not obvious in one low power frame we have presented here. For MB basal plate infection particularly, panels for embryos 6 and 9 that are classified as weakly infected, include insets showing modest dsRNA immunolabeling from fluorescent (and color inverted) images captured in the same approximate location in that domain a few sections away. B) Whole mount brain-half of a 3dpi embryo stained for dsRNA to show hot-spots of infection along the ventricular surface (*=mesenchymal infection in the tissue surrounding the brain is not considered as a hot-spot). The basal plate at MB+DE, hypothalamus, isthmus, and HB show robust infection in this example; there is also some infection in pretectum. Anomalous non-specific labeling is visible in TE due to tissue damage during dissection (cyan arrowheads). Dashed black line shows the approximate plane of sections shown in panel A. C) Schematic shows recurrent hot-spots mapped on an E5 (3dpi) brain. Brain segments are labeled based, in part, on evolutionarily-conserved genoarchitecture (Cavodeassi and Houart, 2012; Echevarria et al., 2003; Ferran et al., 2008; Wurst and Bally-Cuif, 2001). D) Schematic shows presumed prosomeres superimposed on an E5 chicken brain (solid grey lines for anterior-posterior prosomeres and dashed lines for dorsal-ventral subdivisions). Also shown are the approximate expression domains of SHH, FGF8B and BMP7- three morphogens we mapped in ZIKV-infected brains. Abbreviations: D, Dorsal; P, Posterior; FB, forebrain; MB, midbrain; HB, hindbrain; TE, telencephalon; Th, thalamus; Pth, prethalamus; PreT, pretectum; MHB, MB-HB boundary; Hypo, hypothalamus; V, ventricle.

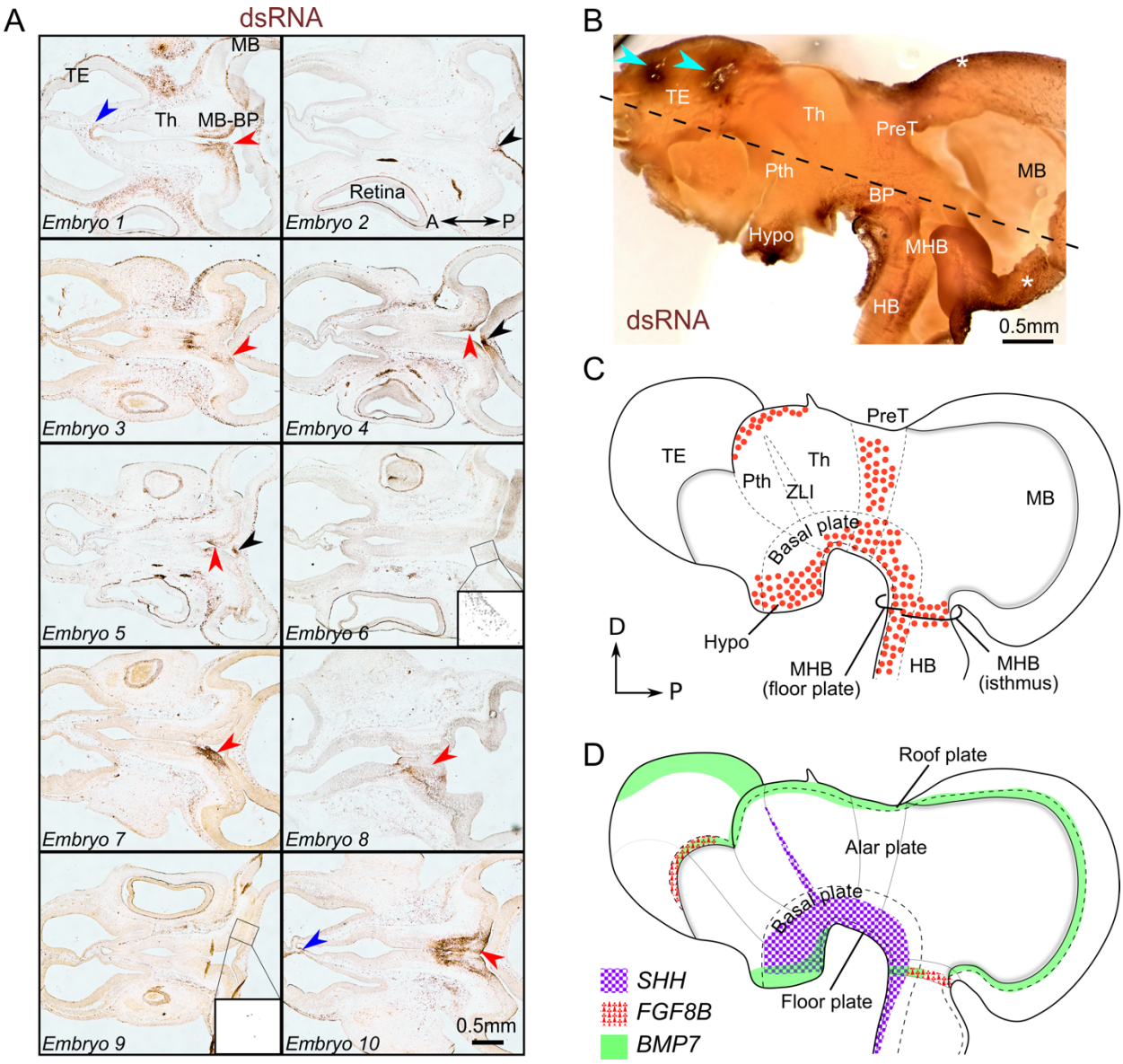
A
dsRNA
MB
TE
Th
MB-BP
Retina
A
P
Embryo 1
Embryo 2
Embryo 3
Embryo 4
Embryo 5
Embryo 6
Embryo 7
Embryo 8
Embryo 9
Embryo 10
0.5mm
B
TE
Th
PreT
Pth
MB
BP
Hypo
MHB
HB
dsRNA
0.5mm
C
TE
PreT
Th
Pth
ZLI
MB
Basal plate
D
P
Hypo
MHB
(floor plate)
HB
MHB
(isthmus)
D
Roof plate
Alar plate
Basal plate
Floor plate
SHH
FGF8B
BMP7

3.2.4 ZIKV in signaling centers abates morphogen expression levels and affects neural patterning

Various neuromeres and neuromere boundaries along both the A-P and D-V axes of the neural tube express evolutionarily-conserved secreted morphogens (SHH, BMPs, FGFs, WNTs) that diffuse into the neighboring neuroepithelium and provide fate specification cues to the immature neural tissue. We mapped transcripts of 3 morphogens expressed in the embryonic chicken brain at 3dpi in areas where ZIKV infection was robust: SHH along the floor plate (Perez-Balaguer et al., 2009), BMP7 at hypothalamic floor plate (Ohyama et al., 2008) and FGF8B at the isthmus (Wurst and Bally-Cuif, 2001) as shown in Figure 3-5D. In the regions with heavy ZIKV infection, these transcripts were reduced as indicated by in situ hybridization (Figure 3-4C, 3-6A). SHH labeling was analyzed quantitatively, whereas BMP7 and FGF8 were analyzed qualitatively by a blinded observer with 70-100% overall agreement achieved (Table 3-2).

We next sought evidence that morphogen reduction could have a functional impact on brain development, focusing on the MB floor plate at 3dpi. Patched1 (PTCH1), a downstream effector in the SHH pathway (Marigo and Tabin, 1996), is reduced (Figure 3-4C, Table 3-2). At comparable stages of mouse development, the knockout of SHH leads to the absence of a PAX6 population in the basolateral MB, and a reduction in an adjacent NKX2.2 population at the alar-basal boundary (Martinez-Lopez et al., 2015; Perez-Balaguer et al., 2009). We hypothesized that in chicken embryos, a ZIKV-associated reduction of SHH expression will either reduce the size or alter the position of the PAX6 and NKX2.2 populations. As expected, SHH+ pixel counts were significantly reduced in ZIKV-infected embryos, but this was not accompanied by a significant change in the size of the PAX6 domain (PAX6+ pixels; Figure 3-4D, E). However, the position of the domain was shifted, with the lateral edge of the PAX6 domain located closer to the midline (Figure 3-4F). The distance of this edge seems to correlate with the size of the SHH expression domain, with ZIKV data points located in the lower left quadrant in Figure 3-4G. Although the NKX2.2 domain was not significantly different in size or position, the lateral edge of the domain shifts medially in a subset of the samples showing reduced SHH expression (Figure 3-4H, I). Overall, the data indicate that D-V brain patterning was disrupted by ZIKV-mediated damage to the SHH-expressing floor plate.

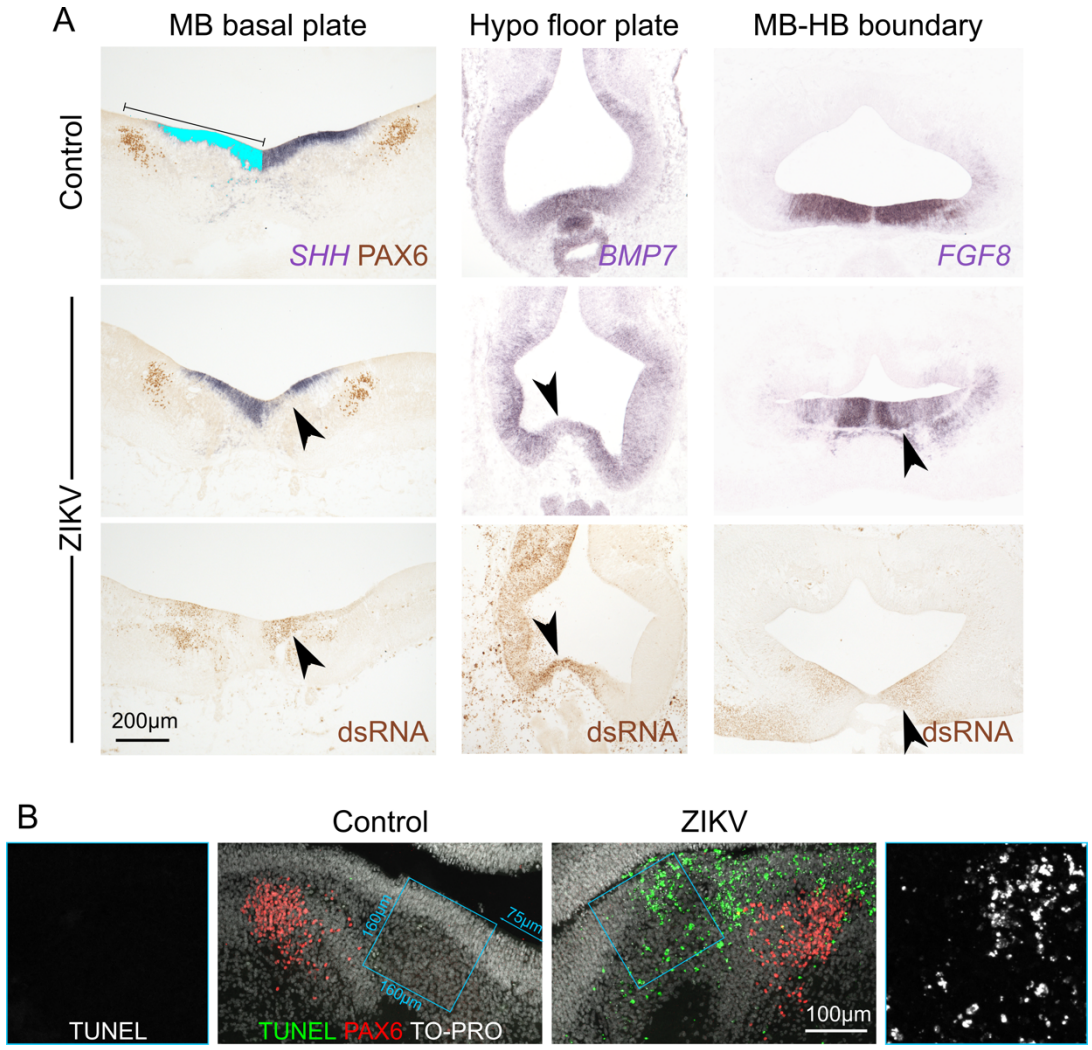

Figure 3-6 Morphogen expression is reduced, and cell death increases in heavily infected regions

A) Transcripts for 3 morphogens were mapped: SHH (MB floor plate), BMP7 (Hypo floor plate) and FGF8B (MHB). PAX6 and dsRNA are shown by immunohistochemical labeling. Each morphogen was reduced in heavily ZIKV-infected regions (black arrowheads). SHH pixels (cyan), PAX6 pixels and distance of the lateral edge of the PAX6 domain from the midline (bracket) were quantified to evaluate domain sizes and patterning. B) Exemplar TUNEL quantification images for a mock-infected control and a ZIKV-injected embryo show the 160µm x 160µm area (blue box) selected approximately 75µm away from the midline. The TUNEL signal was split from the multi-channel fluorescent image, as shown in the flanking magnified quantification fields, and the number of TUNEL-positive pixels was measured after thresholding pixel intensity. Robust ZIKV-infection was determined by dsRNA-labeling of adjacent sections (data not shown).

Table 3-2 Qualitative blinded analysis for in situ hybridization signal

Transcript	**Control**	**ZIKV** (weak or no infection)	**ZIKV** (strong infection)	**Total agreement**
PTCH1	50% (n=5)	80% (n=5)	100% (n=3)	**75%**
BMP7	100% (n=5)	100% (n=1)	100% (n=4)	**100%**
FGF8	100% (n=2)	75% (n=4)	60% (n=5)	**70%**

Images of transcript expression from a single control embryo were provided as templates to an observer blinded to treatment condition. Sampling regions included the MB basal plate (PTCH1), the hypothalamus (BMP7) and the MB-HB boundary (FGF8); see Figure 3-6A for exemplar images. The observer was asked to judge whether the *in situ* hybridization signal was knocked down in comparison to the template. Another observer (not blinded) independently judged whether each ZIKV-infected sample region showed little to no infection in the MHB, or robust infection. Correct responses were those where an assignment of gene knockdown was matched to a region with strong ZIKV infection, or an assignment of normal expression was matched to a control or a sample with little ZIKV infection.

3.2.5 ZIKV infection increases cell death and reduces cell proliferation in the brain

ZIKV-infected cells were mostly located in the periventricular regions that were identified by the densely populated Sox2-expressing progenitors of the ventricular zone and the surrounding intermediate zone of immature neurons (Figure 3-7A-D). As expected in the developing brain, phosphohistone-3-positive (pH3+) dividing cells were located along the apical surface of the ventricular zone, where the nuclei reside during M-phase of the cell cycle (Misson et al., 1988). Heavily-infected regions (dsRNA+) had fewer pH3+ cells and more TUNEL+ labeling (compare Figure 3-7A to 3-7B; Figure 3-7C-D). In an exemplar specimen with bilaterally asymmetric ZIKV infection, these changes were particularly striking in a direct comparison of the two sides, with large numbers of fragmented nuclei visible with TUNEL and TO-PRO on the heavily-infected side (Figure 3-7E). Quantitative analysis verified the increase in cell death associated with ZIKV infection (Figure 3-7F, 3-6B).

Sensory organs can also be impacted by ZIKV infection, such as chorioretinal atrophy, optic nerve atrophy and focal pigment mottling in the eye (de Paula Freitas et al., 2016; Miner et al., 2016b; Moore et al., 2017). In 60% of 3dpi embryos, we observed ZIKV-infected foci in the retina (or the optic nerve), with robust infection correlating with local thinning of the retina, lack of pigmentation (PE), lack of stratification, reduced cell proliferation, increased cell death and often epithelial delamination (Figure 3-7G).

At 7dpi, the medial age of survival, sparse infection remained in the neuroepithelium. Retinal infection was still observed with the aforementioned defects, in addition to frequent infection of extraocular muscles (Figure 3-8).

Figure 3-7 ZIKV infection causes reduced proliferation and increased cell death

A-D) Immunostaining at 3dpi shows ZIKV infection (dsRNA) primarily in the Sox2-positive cells of the ventricular zone (VZ) and adjacent intermediate zone (IZ). Regions of high ZIKV infection show fewer pH3+ cells and more TUNEL+ puncta (TUNEL signal quantified in Figure 3-7F). Other recurring 'hot spots' of infection include MHB (C) and thalamus (D). Sample sizes: dsRNA, n=15; pH3, n=6; TUNEL, n=5. E) Dorsal-anterior thalamic section with bilaterally asymmetric infection facilitates a comparison of pH3 and TUNEL labeling under different ZIKV loads. The bottom, heavily-infected, side (green dsRNA) has fewer pH3+ cells (magenta) at the ventricular surface, more TUNEL+ puncta (red) and more TO-PRO®-3+ nuclear fragments (white). Such stark asymmetry of infection was relatively uncommon in our data set. Panels B-E correspond to Embryo #4 of Figure 3-4A. F) Area occupied by TUNEL+ pixels was quantified at the MB basal plate, a common hot-spot of infection (n=6 controls, 6 ZIKV; one-tailed Mann-Whitney test). Error bars represent mean ± SEM. G) Retinal infection is observed in 60% of embryos at 3dpi (n=15). High ZIKV infection overlapped with retinal atrophy and delamination (black box in DIC image), low pH3+ and high TUNEL+ signals (yellow bracket). Data corresponds to Embryo #5 of Figure 3-4A. Abbr: A, Anterior; DIC, differential interference contrast; MHB, MB-HB boundary; PE, pigment epithelium; P, Posterior; V, Ventricle. See also Figures 3-5 and 3-8.

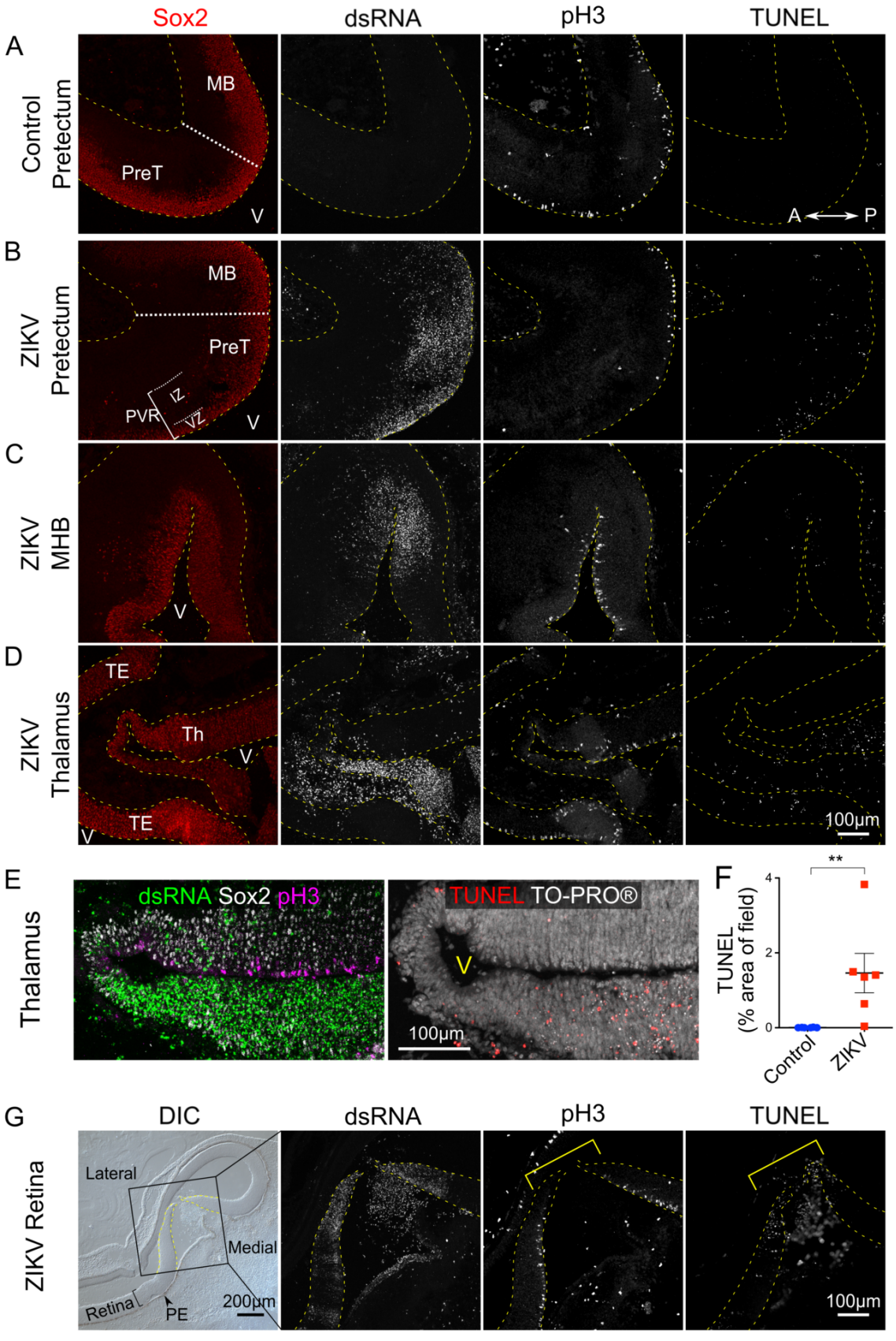
Sox2
dsRNA
pH3
TUNEL
A
Control Pretectum
MB
PreT
V
A
P
B
ZIKV Pretectum
MB
PreT
PVR
VZ
SVZ
V
C
ZIKV MHB
V
D
ZIKV Thalamus
TE
Th
V
TE
V
100μm
E
Thalamus
dsRNA Sox2 pH3
TUNEL TO-PRO®
V
100μm
F
TUNEL (% area of field)
**
4
2
0
Control
ZIKV
G
ZIKV Retina
DIC
dsRNA
pH3
TUNEL
Lateral
Medial
Retina
PE
200μm
100μm

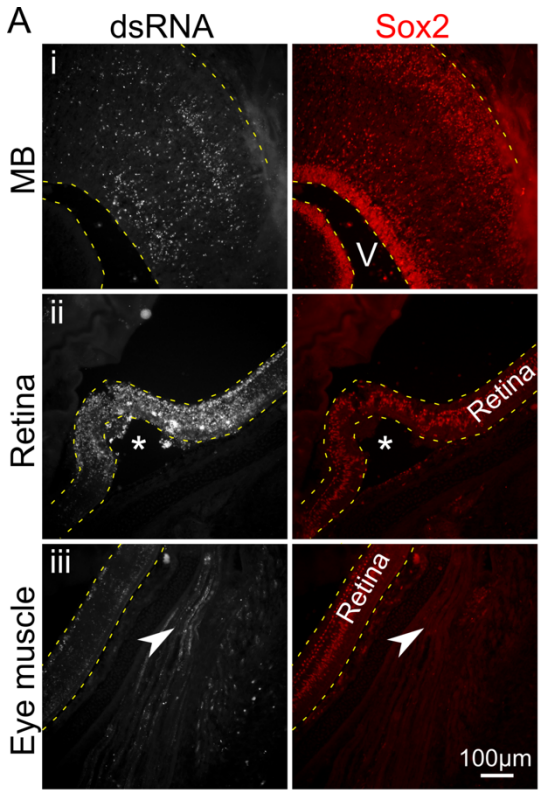

Area of infection	# Embryos Infected (n=7)	% Embryos Infected
Eye muscle	7	100%
Neck muscle	7	100%
Midbrain (MB)	6	86%
Retina	4	57%
Hypothalamus (Hypo)	4	57%
Hindbrain (HB)	3	43%
Mesenchyme	7	100%

Figure 3-8 ZIKV infection in 7dpi embryos

A) Antibodies to dsRNA and Sox2 show the location of cells with detectable ZIKV and neural progenitors, respectively. Infection hot-spots in the periventricular epithelium are diminished by this age (7dpi), as the neural progenitors are migrating into the MB lobes and showing sparse infection (i-iii). Infected cells in the retina (ii) and extraocular muscles (iii) are often observed. Heavily-infected foci in the retina (ii) showed a blister-like retinopathic phenotype (asterisk) beneath a region with disrupted stratification of the retinal cell layers. White arrowhead points to infected extraocular muscle fibers (iii). B) Dorsal view of exemplar 7dpi embryo heads with a yellow arrowhead pointing to an eye atrophic defect. C) A summary of repeatedly observed regions of infection at 7dpi (n=7). Abbreviations: TE, telencephalon; Th, thalamus; Pth, prethalamus; PreT, pretectum; MB, midbrain; MHB, midbrain-hindbrain boundary or isthmus; HB, hindbrain; Hypo, hypothalamus; V, ventricle.

3.3 Conclusions and Discussion

Like humans, birds can be infected by flaviviruses such as West Nile virus, and hence birds are often used as sentinels for arboviral disease detection (Fair et al., 2011; Langevin et al., 2001). In this study, we investigated the cell and tissue tropism of ZIKV (a flavivirus) in chicken embryos by inoculating them just after closure of the neural tube, a developmental stage comparable to the early 4th week in human gestation (Carnegie stage 11) (Butler and Juurlink, 1987). Although direct ventricular injection does not mimic a natural viral transmission route, our goal was to offer a relatively higher throughput in vivo model to study ZIKV pathogenesis. ZIKV caused a productive infection in chicken embryos, as shown previously (Goodfellow et al., 2016). With an inoculum size of ~1,000 pfu, lethality reached 100% within 15 dpi. It is not known if animals die because of the ensuing neural deficits, or from some other cause as the virus spreads systemically. The presence of ZIKV in the periventricular region increased cell death, decreased mitotic activity, was sometimes accompanied by reduced expression of the proneural gene Sox2 and could lead to delamination of the neuroepithelium. While periventricular infection and apoptosis were abundant at 3dpi, very few infected cells were evident 4 days later. This clearance of infected cells is consistent with qRTPCR data showing that brain viral load fell at 5-7 dpi. In contrast, DENV injection into chicken embryos was not lethal and did not lead to any detectable infection at 3dpi with anti-dsRNA immunolabeling (data not shown).

Early regionalization and fate specification of the central nervous system is regulated in part by key signaling centers that are conserved across vertebrates (Ferran et al., 2008; Garcia-Lopez et al., 2009; Puelles and Rubenstein, 2015; Wurst and Bally-Cuif, 2001). For example, the isthmic organizer at the MB-HB boundary regulates formation of the adjacent mesencephalon anteriorly and the cerebellum posteriorly via Wnts and Fgfs (Cavodeassi and Houart, 2012; Echevarria et al., 2003). Similarly, the floorplate expresses Shh, and the encoded protein is thought to diffuse dorsally to specify discrete neuronal identities along the D-V axis based on a morphogen model (Echevarria et al., 2003; Perez-Balaguer et al., 2009). Specification of various cell populations, such as dopaminergic and serotonergic neurons of the ventral MB-HB and motor neurons of cranial nerves III-IV, is dependent on patterning cues from the isthmus (A-P signaling center) and the floor plate (Shh, D-V signaling center) (Echevarria et al., 2003; Wurst and Bally-Cuif, 2001). Abatement of signaling factors alters the specification or location of neighboring cell populations.

Hence, it was intriguing to discover recurring foci of dense ZIKV infection at several of the morphogen-expressing secondary organizers in our data. Some of these 'hot-spots' separate A-P compartments (pretectum, isthmus), or reflect D-V compartmentalization (basal plate ventral to the pretectum, thalamic roof plate, hypothalamus). Another 'hot-spot' observed less frequently was the dorsal midline (or roof plate) of the MB or TE. The diencephalic regions often showed scattered infection that was much reduced compared to the 'hot-spots'. Although there was relatively little infection along the ventricular zone of the dorsal MB, we propose that heavy infection and resulting ZIKV-mediated apoptosis within the neighboring signaling centers could mediate non-cell-autonomous effects on MB development. In support of this idea, in the presence of heavy ZIKV infection, there was a reduction in expression of three morphogens (SHH, BMP7, FGF8) within three different signaling centers (the MB floorplate, the hypothalamus floorplate and the posterior isthmus, respectively). In the case of SHH bioactivity at the MB basal plate, suggestive evidence of weaker downstream signaling was shown by PTCH1 in situ hybridization. However, since SHH and PTCH1 domains partially overlap, it is unclear whether the diminished PTCH1 expression primarily reflects weaker SHH protein levels reaching the responsive cells (i.e., an indirect effect), or whether reduced responsiveness and/or survival of the PTCH1-expressing cells could also be contributing factors. We further provide evidence for a neighboring neuroepithelial patterning change in an adjacent PAX6 cell population known to be dependent upon SHH for specification. We do not observe a significant difference in the PAX6 domain size (pixel count). Although direct effects of ZIKV infection on the PAX6 lineage are possible, we observed far less infection within the PAX6+ domain, or in the nearby ventricular zone, in comparison to the SHH-expressing domain at the midbrain basal plate. Specifically, the SHH-expressing cells had 4.7 times more infection (dsRNA+ pixels) and 28 times more cell death (TUNEL+ pixels) than the PAX6+ cells (data not shown). A significant change was not observed for the NKX2.2 cell population lateral edge position, possibly because it forms further from the SHH basal domain than the PAX6 cells, or maybe NKX2.2 cells depend on additional morphogens.

In human infants and various animal models including the chicken embryo, ZIKV exposure causes microencephaly and enlarged brain ventricles (Adams Waldorf et al., 2016; Goodfellow et al., 2016; Moore et al., 2017; Wu et al., 2016). While our study showed size reductions for several brain regions including the MB, the volume of the MB ventricles was unchanged at 7dpi; if anything, the average ventricular volume was smaller following ZIKV infection. This discrepancy may be related to differences in the site and timing of ZIKV inoculation, and/or ventriculomegaly

might develop from infection during later stages of cortical thickening. Moreover, considering that the MB and TE lobes expand most rapidly during early brain development in the chicken, that we targeted the inoculum to the MB and FB ventricles, and that these structures were obviously reduced by ZIKV injections, we were surprised to find only sparse infection in their respective periventricular regions at 3dpi and 7dpi. This leads us to speculate that the growth retardation of these regions might have been indirectly influenced by disruptions in nearby brain structures (such as the secondary organizers).

It remains to be shown whether the regional brain tropism displayed by ZIKV in chicken embryos extends to mammals, and whether it can be explained by differential expression of receptors for the virus or other cellular characteristics of signaling centers.

In summary, the chicken embryo is a suitable and self-contained animal model to study the pathogenesis of ZIKV infection in a tissue-specific and temporal manner, and potentially to explore therapeutics because of its relative accessibility. Our results suggest that ZIKV exhibits a more nuanced neurotropism than previously appreciated: it preferentially targets specific subpopulations of neural stem cells, particularly some known signaling centers, which leads to reduced morphogen transcripts and alters neural patterning.

CHAPTER 4. ZIKA VIRUS PATHOGENESIS IN DEVELOPING INNER EAR

This section is a first author manuscript in preparation.

Thawani A, Sammudin NH, Reygaerts H, Munnamalai V, Kuhn RJ, & Fekete DM. Zika virus infects the vestibular and auditory organs of the developing inner ear in the chicken embryo. (Manuscript in preparation)

4.1 Zika virus can cause auditory organ defects during embryonic development

Zika virus (ZIKV), a mosquito-borne pathogen, is a newly identified teratogenic virus that causes mild flu-like infection symptoms in adults and severe congenital defects in gestating fetuses (Barbi et al., 2018; Dick, 1952; Dick et al., 1952; Moore et al., 2017; Rasmussen et al., 2016). Congenital Zika Syndrome can present with brain defects (microencephaly, ventriculomegaly, brain calcifications, brainstem defects), joint contractures, and sensory system defects (chorioretinal atrophy, lens subluxation, hearing loss) (Melo et al., 2016; Moore et al., 2017; Ventura et al., 2016). Hearing loss can be attributed to (1) damage of the outer or middle ear, i.e., conductive hearing loss, or (2) dysfunction of inner ear or the auditory pathway, i.e., sensorineural hearing loss. Evidence of sensorineural hearing loss has been detected in 6-9% of the microcephalic cases from the recent Brazilian outbreak, based on diminished otoacoustic emissions and/or auditory brainstem responses (Group, 2016; Leal et al., 2016a; Leal et al., 2016b). However, several reviews indicate that the number might be grossly underestimated as only the patients with evident microcephaly were included in these studies (Mittal et al., 2017).

The neurotropic nature of ZIKV has been demonstrated primarily using three mammalian model systems: neuronal derivatives of human stem cells, non-human primates and mice. These studies revealed that ZIKV reduces the proliferation of neural stem cells and increases cell death (Caine et al., 2018; Garcez et al., 2016; Li et al., 2016c; Miner and Diamond, 2017; Qian et al., 2017; Qian et al., 2016). The vulnerability of sensory systems associated with the inner ear warrants further investigation. The inner ear contains neurons and sensory organs for hearing and balance. It develops from an otic placodal domain located adjacent to the future hindbrain region of the neural plate (Singh and Groves, 2016). As the inner ear develops, it deepens into an otic cup, seals off to form an otocyst, and then morphs into a three-dimensional complex, endolymphatic fluid-filled labyrinth, with a dorsally located vestibular compartment (important for detecting

balance), and a ventrally located cochlear duct (important for audition). The mammalian inner ear comprises of six key sensory patches: (1) three cristae, one associated with each semicircular canal, to detect angular acceleration; (2) two macula located in the utricle and saccule that are arranged perpendicularly to each other to sense linear acceleration (gravity); and (3) one cochlea containing the organ of Corti to sense sound. The chicken inner ear contains two additional maculae: the macula neglecta near the posterior crista and the lagenar macula at the ventral-most tip of the cochlear duct. Its hearing organ, the basilar papilla, is homologous to the mammalian organ of Corti. All inner ear sensory organs consist of organized arrays of mechanosensory hair cells with ion channels that are apically exposed to the potassium ion rich endolymph. Hair cells are presynaptic to the afferent terminals of statoacoustic ganglion (SAG) neurons and usually receive synapses from efferent axons whose cell bodies reside in the hindbrain. The bulk of SAG neurons originate from the otic cup/otocyst epithelium through a process of delamination (Bissonnette and Fekete, 1996; Dallos et al., 1996; Satoh and Fekete, 2005; Tanaka and Smith, 1978; Torres and Giraldez, 1998).

Progressing through the stages of inner ear development, we hypothesized that several neural progenitor-like cell types could be susceptible to ZIKV infection, specifically immature neurons of the SAG, the cells of the prosensory domain, and immature mechanosensory hair cells. In humans, ganglion formation, prosensory specification and major morphogenesis of the inner ear happens within the first 10 weeks of gestation and the labyrinth achieves its mature size by the 19th week (Lim and Brichta, 2016). Interestingly, it is during this time window (the first 4 months of pregnancy) when most of the mothers that delivered newborns with ZIKV-associated hearing loss reported a fever and other infection symptoms (Leal et al., 2016b). We thus hypothesized that, in addition to the spatial preference of ZIKV infection for neurosensory domains, there is likely to be a temporal window of viral susceptibility of the inner ear epithelium. For this descriptive analysis, we employed the chicken embryo as an accessible vertebrate model organism to examine ZIKV-mediated infectivity and pathogenesis during inner ear development.

4.2 Results

4.2.1 Direct ZIKV injection into the inner ear results in infection of the otic epithelium

The goal of the study was to gather data about both the initial site(s) of infection and the spread of the virus through the developing inner ear epithelium. To accomplish this, a French Polynesian strain of ZIKV from the Asian lineage [H/PF/2013; 9.6x10^7 plaque forming units

(PFU)/ml] was delivered directly to the otic primordium of chicken embryos at embryonic day (E)2, 3, 4, or 5, followed by varying times of survival before collecting tissue for analysis (Figure 4-1A, B). Inoculum was delivered until the otic cavity was filled yet not over-inflated to maximize the viral load delivered to the target tissue while minimizing leakage (Figure 4-1C-F). Accessing the inner ear at E4 and 5 required teasing open the extra embryonic membranes to allow for the reorientation of the embryo within the amniotic sac. Embryonic tissues (whole heads until E8-9 and temporal bones at later stages) were systematically harvested at 2, 4, 6, and 8 days post infection (dpi) and processed for tissue sectioning for analyzing the localization of ZIKV infection (Figure 4-1A). Table 4-1 lists some key milestones for the ages of infection and harvests as a reference for the relevance of the timeline of the study.

Viral infection was detected by immunolabeling for double-stranded RNA (dsRNA), since dsRNA motifs are abundantly produced in flaviviral-infected host cells when the single-stranded RNA genome is actively replicating (Weber et al., 2006). The overall strength of infection indicated that only one third of the embryos were well infected after the injection (Figure 4-1G); see later text for details of evaluating levels of infection.

ZIKV is neurotropic in nature and primarily infects neural progenitors in the developing embryonic brain. With that information, we hypothesized that the mitotic prosensory domains of the inner ear would be more susceptible to ZIKV infection compared to either mature sensory organs or non-sensory domains. Sox2, a classic marker for neural progenitors that also labels supporting cells of the inner ear sensory organs and glial cells in the SAG, was used to identify the prosensory/sensory domains and the SAG (Neves et al., 2007). Interestingly, we observed that sensory as well as non-sensory tissue of the otic epithelium was infected by ZIKV. Figure 4-2 shows several representative examples of infection in Sox2-positive sensory/prosensory (solid arrowheads) and Sox2-negative non-sensory (blank arrowheads). Neurofilament (NF) is another antibody marker used for locating sensory organs because axons reach the prosensory domains before the hair cells are born. Many of these axons are presumed to originate from developing SAG neurons. Figure 4-2G shows infection in the Sox2-positive auditory ganglion adjacent to the BP. In addition to the inner ear tissue, the periotic mesenchyme often presented with dsRNA immunolabeling (Figure 4-2B, E, G, H). We thus speculate that the virus might be able cross the basement membrane of the epithelium to reach the surrounding tissue. Yet another possibility is that during E3 to E5 injections, perhaps puncturing the otic epithelium laterally created an escape route for the viral particles into the surrounding mesenchyme.

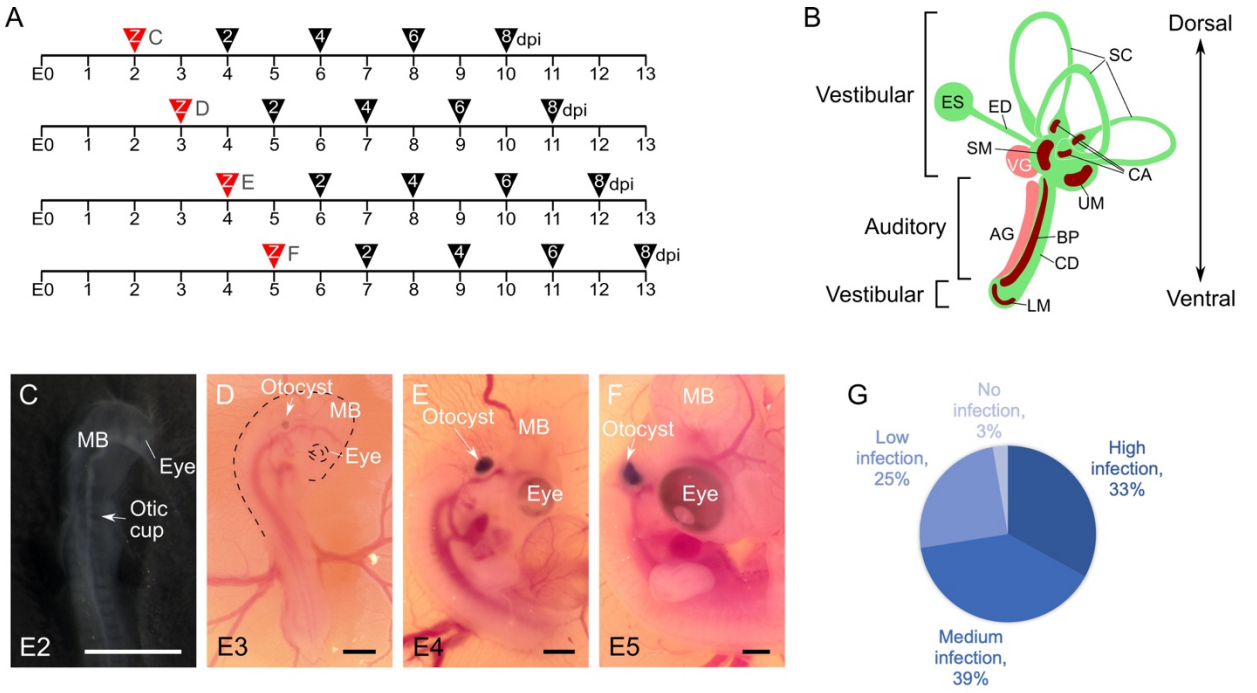

Figure 4-1 Direct ZIKV injection to the inner ear was performed to study viral pathogenesis in its associated structures.

(A) Timelines of infection and tissue harvest after direct inner ear injections from E2 to E5 *in ovo*. (B) Schematic of the avian inner ear after its three-dimensional morphogenesis is complete; this figure represents an inner ear at approximately E8 to E13 for the purposes of this study. The green color shows the non-sensory epithelia of the labyrinth with the sensory patches in maroon. This includes three cristae (anterior, posterior and lateral), three maculae (utricular, saccular and lagenar; neglecta not shown) and the basilar papilla. Salmon color shows the vestibular and auditory ganglia. (C-F) ZIKV inoculum (arrows and green tinge) into the otic cup (C) or otocyst (D-F) at E2 to E5. (G) Overall success of infection in the embryo analyzed through histology (explained in detail in section 4.2.2). Abbr.: AG, auditory ganglion; BP, basilar papilla; CA, cristae ampullaris; CD, cochlear duct; dpi, days-post-infection; ED, endolymphatic duct; ES, endolymphatic sac; LM lagenar macula; MB, midbrain; SC, semicircular canals; SM, saccular macula; UM, utricular macular; VG, vestibular ganglion; Z, Zika virus.

Table 4-1 Milestones of the embryonic chicken inner ear development during the period of study

Embryonic day	**Morphology**	**Some key markers**
E2	Otic cup invaginates; Neuroblasts start delaminating	Sox2 and Ngn1 label the neuro-sensory domain, regions from which Islet1+ neuroblasts delaminate
E3	Otocyst closes into a cavity; Dorso-ventral axis defined; Neuroblasts start differentiating and axonal outgrowth of bipolar neurons	
E4	Dorsal canal, endolymphatic duct, and cochlear domain pouches extend; Axons penetrate BP	Bmp4 marks 3 cristae, 2 vestibular maculae and the cochlea
E5	Vertical and horizontal canal pouches are distinguishable; First hair cells of the BP are borne	
E6	Canal fusion of vertical and horizontal pouches; Mesenchyme begins forming cartilage around the labyrinth	HCS1+/Sox- hair cells in the vestibular compartment
E7	All parts of the membranous labyrinth formed but morphogenesis continues	HCS1+/Sox- hair cells in the auditory compartment (ventral tip)
E8	Posteromedial elongation of cochlear duct and endolymphatic duct/sac	
E9	Hair cells of the BP stop dividing; Stereocilia produced; Endolymphatic sac makes contact with the hindbrain	
E10	Auditory ganglion neurons develop synapses with hair cells	
E11	Connection between the vestibular and cochlea becomes very thin ductus reuniens; Otoconia appear on maculae	
E12	Calcification of the cartilage begins; Tegmentum vasculosum begins to secrete	
E13	Auditory histogenesis complete	

(Fekete and Wu, 2002; Goodyear et al., 2010; Groves and Fekete, 2012; Knowlton, 1967; Neves et al., 2011; Wu and Kelley, 2012; Wu and Oh, 1996)

Figure 4-2 ZIKV infects sensory and non-sensory epithelia of the inner ear.

(A-H) Examples of infection 6 days after ZIKV injections on E5. Sections through the inner ear were immunostained with antibodies to dsRNA (green) for ZIKV infection, Sox2 (red) for sensory domain marker and NF70 (blue) for axons. These representative images were selected from 3 embryos to show examples of sensory (A-D; solid arrowheads) and non-sensory (E-H; open arrowheads) infection. The epithelium is outlined with dashed lines. Panels B, E, G and H also show evidence of periotic mesenchymal infection. Scale bar = 100μm. Abbr: AG, auditory ganglion; BP, basilar papilla; CA, cristae ampullaris; dpi, days-post-infection; ES, endolymphatic sac; Hm, homogene cells (non-sensory cochlea); LM lagenar macula; LSC, lateral semicircular canal; MB, midbrain; SM, saccular macula; UM, utricular macular.

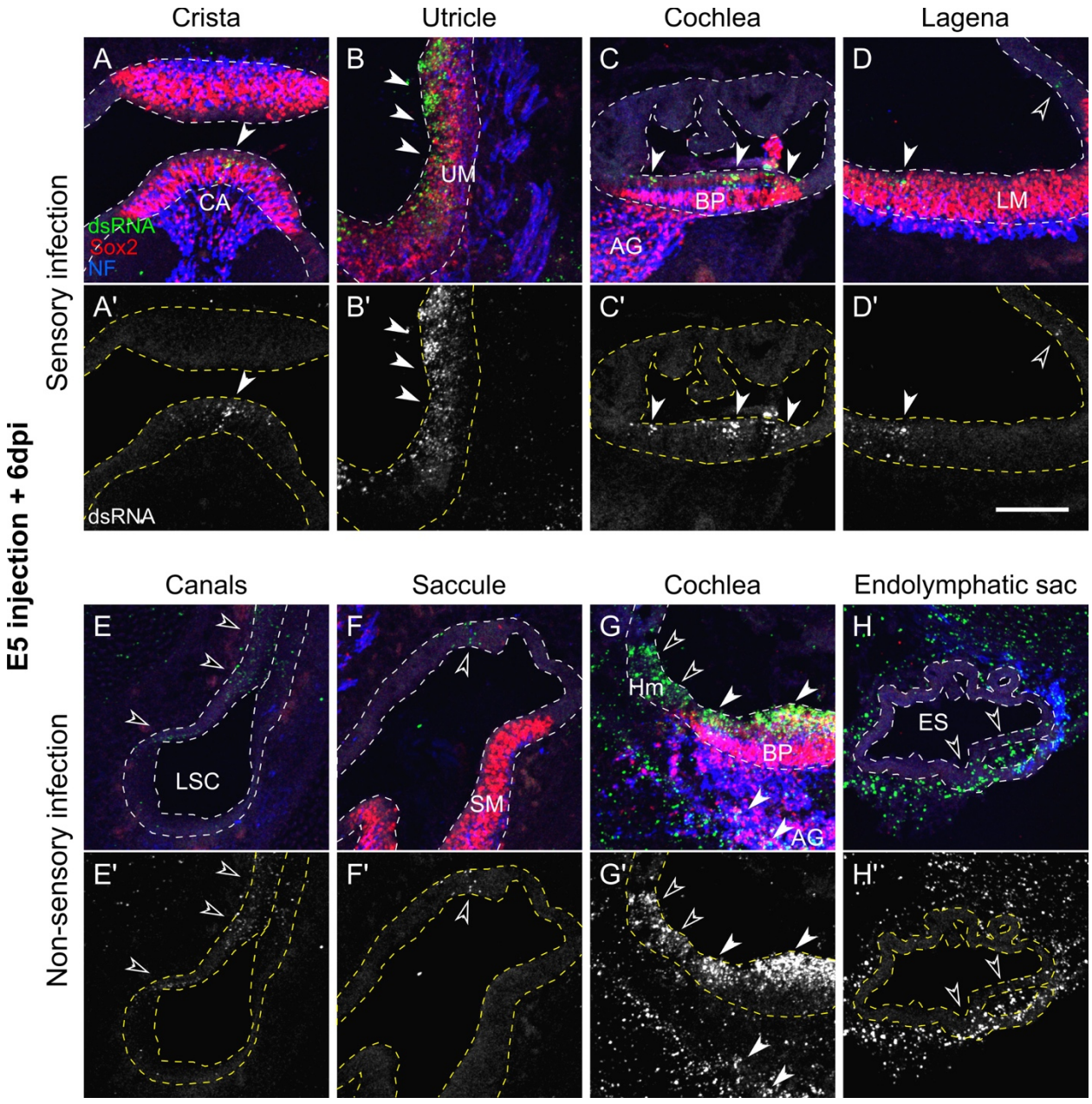
E5 injection + 6dpi
Sensory infection
Non-sensory infection
Crista
Utricle
Cochlea
Lagena
Canals
Saccule
Cochlea
Endolymphatic sac
A
B
C
D
A'
B'
C'
D'
E
F
G
H
E'
F'
G'
H'
CA
UM
BP
AG
LM
dsRNA
Sox2
NF
dsRNA
LSC
SM
Hm
BP
AG
ES

4.2.2 Semi-quantitative analysis of ZIKV infection in various parts of the inner ear to reveal patterns of infection susceptibility

In order to map the spatiotemporal distribution of ZIKV infection within the inner ear, we analyzed 5 to 10 embryos per age of injection and subsequent harvest as explained in Figure 4-1A. Different sensory domains of the inner ear develop and differentiate at different times during embryonic development. For instance, vestibular sensory organs develop and mature sooner than the auditory organ; anterior and posterior cristae develop sooner than the lateral crista (Knowlton, 1967; Lim and Brichta, 2016; Wu and Oh, 1996).

To investigate the inner ear labyrinth in its entirety, tissue sections sampling the ear from the dorsal to the ventral end were immunostained with anti-dsRNA antibody. Additionally, neural markers such as Sox2 (neural progenitor), HuC/HuD (neurons leaving mitotic cell cycle), and/or NF (axons) were used as co-labels to identify the morphology of the inner ear tissue. As elaborated in the 'Materials and Methods' section, for embryos until E8/9, whole heads were decapitated and processed for histology; however, the ear capsules were dissected for older animals.

We divided the inner ear into separate groups of tissue to characterize infection of each cell population. The semicircular canals, ampullae (cristae), vestibular maculae, and cochlea were evaluated separately. The sensory and non-sensory epithelium of each of these structures was graded separately. Furthermore, the vestibular and auditory ganglia were analyzed separately from the inner ear labyrinth, except for E4 ears, where the delaminated neuronal mass has not yet separated into two parts: vestibular and auditory. Additionally, we included the endolymphatic sac and duct, the lagena, and the periotic mesenchyme in our analysis. To observe patterns or trends of infection over this three-dimensional dataset, we rated the infection in each of the aforementioned cell populations on a scale of no infection to high infection, and assigned them an integer value from 0 to 3 (Figure 4-3A). Characteristic examples of this rating system are shown in Figure 4-3B using images of infected basilar papilla (BP) tissue sections with dsRNA-Sox2-NF immunolabeling.

Figure 4-3C shows the full breadth of our data with all 109 embryos investigated for ZIKV infection and charted so to observe trends of viral susceptibility. Notably, for some embryos, certain columns could not be analyzed: (1) E2+2dpi embryos did not show a lagenar domain clearly separated from the BP; and (2) endolymphatic sac and duct were missing from the dissected ear capsules, possibly lost during dissections. We observed that all 3 cristae and their associated canals (anterior, posterior and lateral), two vestibular maculae and the chambers in which they

reside (utricle and saccule), and the cochlear duct were infected in the majority of embryos. In contrast, the lagena and the endolymphatic sac/duct were infected less frequently, and hence excluded from further analyses. Interestingly, in 103 out of 105 embryos, infection of the inner ear epithelium was accompanied by infection of the surrounding periotic mesenchyme.

As mentioned above, we hypothesized that the prosensory domains would be more susceptible to ZIKV infection than the non-sensory tissue, with the domains being identified by differential expression of several neural progenitor-like markers, such as Sox2. Contrary to our prediction Figure 4-3C shows that non-sensory territories were infected about as frequently as the sensory organs. A plot of the average infection trends for the vestibular compartments (canals, cristae, vestibule) versus the auditory organ (cochlear duct) shows that infection of the cochlea appears to be higher when older embryos were observed, disregarding the age of inoculation (Figure 4-3D).

During this comprehensive analysis, two apparent developmental defects were observed in the inner ear: (1) stunted canal formation; and (2) severely reduced auditory ganglion. These defects are elaborated on further in the consecutive ‘Results’ sections.

Figure 4-3 Semi-quantitative analysis of ZIKV infection in the inner ear after E2-E5 inner ear injections.

(A) Description of the color-coding key employed to qualitatively analyze the levels of infection and assign numeric values to them (0, 1, 2, and 3). (B) Exemplar infection of mid-maturation BPs to represent what was classified as low, medium or high infection. The samples are stained for dsRNA (green, infection), Sox2 (red, sensory domain) and NF70 (blue, axons). Scale bar = 20μm. (C) Summary of 109 embryos analyzed histologically after ZIKV infection and harvested at specific days post infection. Each row represents one embryo analyzed for degree of infection observed in various locations in the developing inner ear. The color scheme for sensory/neuronal (red) vs. non-sensory (green) corresponds to that shown in Figure 4-1B. For specimens showing infection within the non-sensory cochlear duct, the specific subdomains (homogene cells, hyaline cells, cuboidal cells, tegmentum vasculosum) with dsRNA labeling are indicated on each green bar. (D) Trends of infection in the vestibular versus cochlear tissue of the inner ear at various ages of harvest. Nabilah H. Sammudin and Hannah Reygaerts assisted with the immunostaining, imaging and analysis of infection to build Figure 4-3C. Abbr.: AG, auditory ganglion; CA, crista ampullaris; CD, cochlear duct; C, cuboidal cells; dpi, days-post-infection; ED, endolymphatic duct; ES, endolymphatic sac; Hm, homogene cells; Hy, hyaline cells; Inf, overall infection; L, lagena; Mes, periotic mesenchyme; NS, non-sensory epithelium; S, sensory epithelium; SC, semicircular canals; T, tegmentum vasculosum; U/S, utricle/saccule; VG, vestibular ganglion.

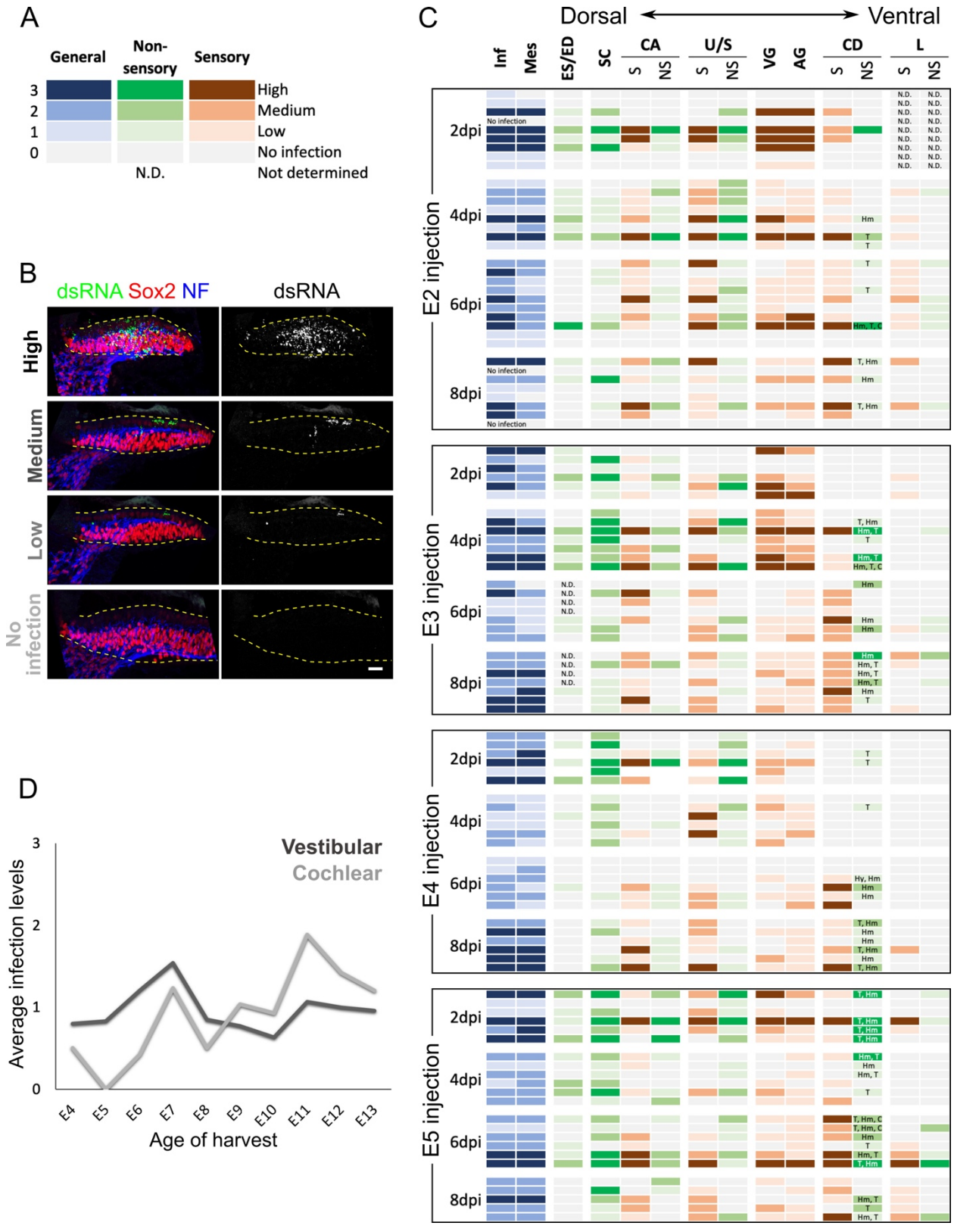
A
General
Non-sensory
Sensory
3
2
1
0
High
Medium
Low
No infection
N.D.
Not determined
B
dsRNA Sox2 NF
dsRNA
High
Medium
Low
No infection
C
Dorsal
Ventral
Inf
Mes
ES/ED
SC
CA
U/S
VG
AG
CD
L
S
NS
E2 injection
E3 injection
E4 injection
E5 injection
2dpi
4dpi
6dpi
8dpi
D
Vestibular
Cochlear
Average infection levels
Age of harvest
E4
E5
E6
E7
E8
E9
E10
E11
E12
E13

4.2.3 ZIKV infection results in canal morphogenesis defects

About 40% of the injected ears showed significant ZIKV infection (infection rating 2 or 3) in the semicircular canals. Using the semi-quantitative analysis chart in Figure 4-3C, we constructed a three-dimensional histogram using averaged infection levels over all the embryos in a category to observe trends of infection versus the age of infection and harvest. The highest levels of infection were observed in embryos injected at later stages (Figure 4-4A). Interestingly, a closer look at the histology showed several incidents of canal fusion defects, particularly after E2 injections. An exemplar paint-fill of the inner ears in an embryo injected at E2 and harvested at 6dpi suggests that canal morphogenesis may be stalled at a prefusion stage. The vertical and horizontal canal pouches are still present and located approximately where they would be just prior to fusion (about E6). Moreover, the overall semicircular canal domain is reduced in size for their actual age of E8 (compare to the control in Figure 4-4B), and a partially grown anterior semicircular canal phenotype is present in the defective inner ear. Another example of an E2+6dpi embryo using histology is shown in Figure 4-4C. Remarkably, we observe indications of some under-fusion (canal pouches still present), as well as arguably some over-fusion phenotypes (partial canal formation).

Figure 4-4 ZIKV infection results in severe morphological defects in the vestibular compartment. (A) A three-dimensional histogram allows visualization of the temporal trends of semicircular canal infection as a function of both the stage of injection (E2-5) and the days-post-injection (2-8dpi; age at the time of harvest is labeled on each bar). Two-way ANOVA; $p<0.001$ for dpi and the age of injection as individually significant variables; $p<0.05$ for interaction between the two variables. (B) Paint-filled inner ears 6dpi after E2 ZIKV injections. The images are representative of canal morphogenesis defects often observed post E2 injections. The panel shows an unaffected ear and one severely deformed ear post ZIKV infection with a partial anterior canal (ASC*). Scale bar = 1mm. (C-C') A control ear is compared to an example of canal morphology defect in cryosectioned samples stained for dsRNA (green, infection), Sox2 (red, sensory domain) and NF70 (blue, axons). White arrowheads show regions of the vertical canal pouch that failed to fuse in panel C'. Panel C is the contralateral uninjected ear and normal canal morphology is observed. Dashed yellow lines in panel B show the approximate axis of sectioning for the representative images, however the C-C' embryo is different from the ones used for panel B. Scale bar = 100μm. Abbr.: ASC, anterior semicircular canal; CD, cochlear duct; D, dorsal; dpi, days-post-infection; ES, endolymphatic sac; P, posterior; PSC, posterior semicircular canal.

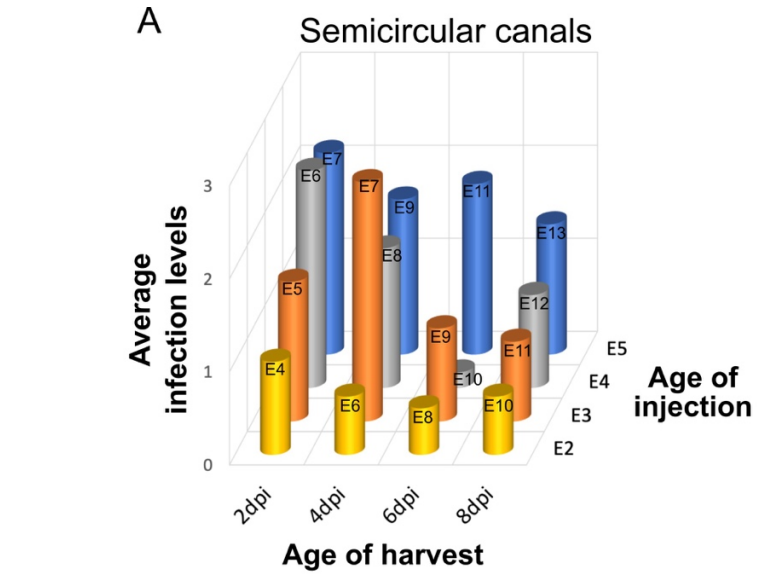
A
Semicircular canals
Average infection levels
0
1
2
3
E4
E5
E6
E7
E6
E7
E8
E9
E8
E9
E10
E11
E10
E11
E12
E13
E2
E3
E4
E5
Age of injection
2dpi
4dpi
6dpi
8dpi
Age of harvest

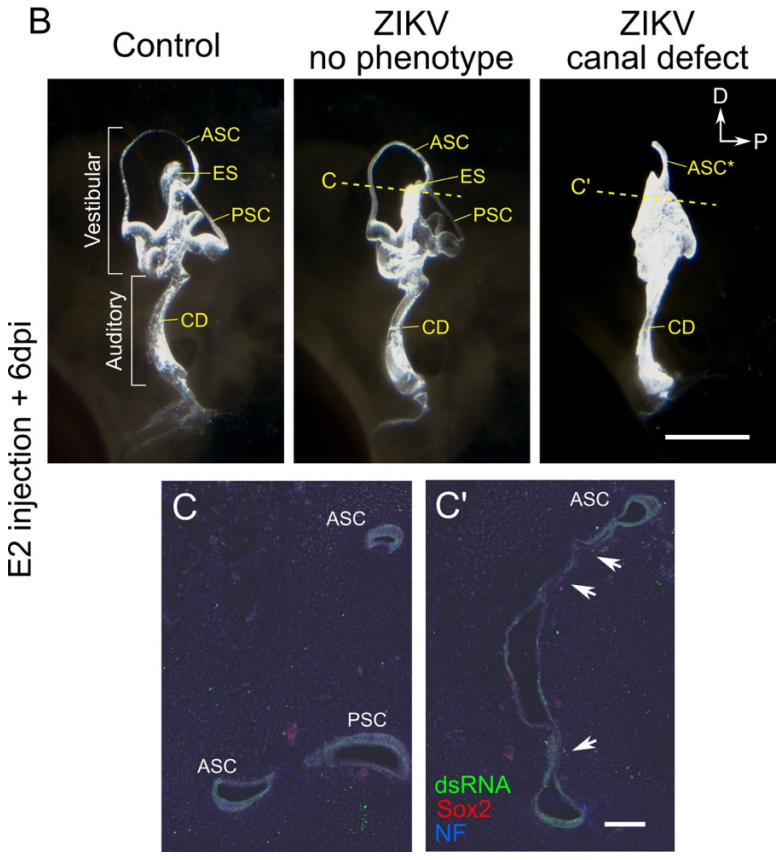
B
Control
ZIKV no phenotype
ZIKV canal defect
E2 injection + 6dpi
Vestibular
Auditory
ASC
ES
PSC
CD
C
C'
ASC*
D
P
C
C'
ASC
PSC
dsRNA
Sox2
NF

4.2.4 ZIKV infection can result in a stunted auditory ganglion

Malformation of the SAG can interrupt relay of information along the auditory pathway to the brainstem and thus be correlated with sensorineural hearing loss as a consequence. We found that after E2 and E3 injections, SAG infection was frequently observed. This time window is intriguing considering the bulk of delamination of cells from the otocyst occurs at these ages. A 3D plot to observe trends of infection shows that the average levels infection in the SAG were lower at later ages of harvests (Figure 4-5A). Figure 4-5B shows an exemplar immunostaining with anti-activated Caspase-3 antibody, to detect programmed cell death, indicating that ZIKV infection results in increased cell death in the SAG on the injected side compared to the contralateral uninjected side. Increased cell death as a result of ZIKV infection was verified by quantitative analysis (Figure 4-5C). Figures 4-5D and E show examples of stunted ganglia in the injected ear compared to the contralateral uninfected ears after E2 and E3 injections.

Figure 4-5 ZIKV can infect and damage the auditory ganglion.

(A) A three-dimensional histogram shows temporal trends of infection intensity in the SAG as a function of both the stage of injection (E2-5) and the days-post-injection (2-8dpi; age at the time of harvest is labeled on each bar) ($p<0.05$; Two-way ANOVA; dpi is a significant variable, but age of injection is not). (B) Exemplar embryo at 2dpi after E2 infection stained for dsRNA (cyan, infection), Sox2 (gray, sensory domain) and activated-caspase-3 (magenta, cell death). The SAG shows increased cell death in the infected ear versus the contralateral uninfected ear. (C) Area occupied by activated caspase positive pixels normalized to the SAG cross-sectional area was quantified for controls (ears from uninjected animals), uninfected (injected but dsRNA-negative ears) and infected (injected and dsRNA-postive ears) samples ($p<0.0001$; Non-parametric one-way ANOVA) (n=36 ears; 18 embryos). (D-E) The auditory ganglion (dashed yellow outline) was often observed to be unusually small on the infected side as compared to the contralateral uninfected side following ZIKV injections on E2 or E3. Note that dsRNA labeling is sometimes found surrounding the otic epithelium on the uninjected sides, as seen in panel B and E. The samples are stained for dsRNA (green, infection), Sox2 (red, sensory domain) and NF70 (blue, axons). Scale bars = 100μm. Abbr.: AG, auditory ganglion; BP, basilar papilla; dpi, days-post-infection; SAG, statoacoustic ganglion; Tv, tegmentum vasculosum (non-sensory cochlear duct). Data collection and quantification for Figure 4-5B & C was done by Nabilah H. Sammudin (second author to the work-in-progress manuscript).

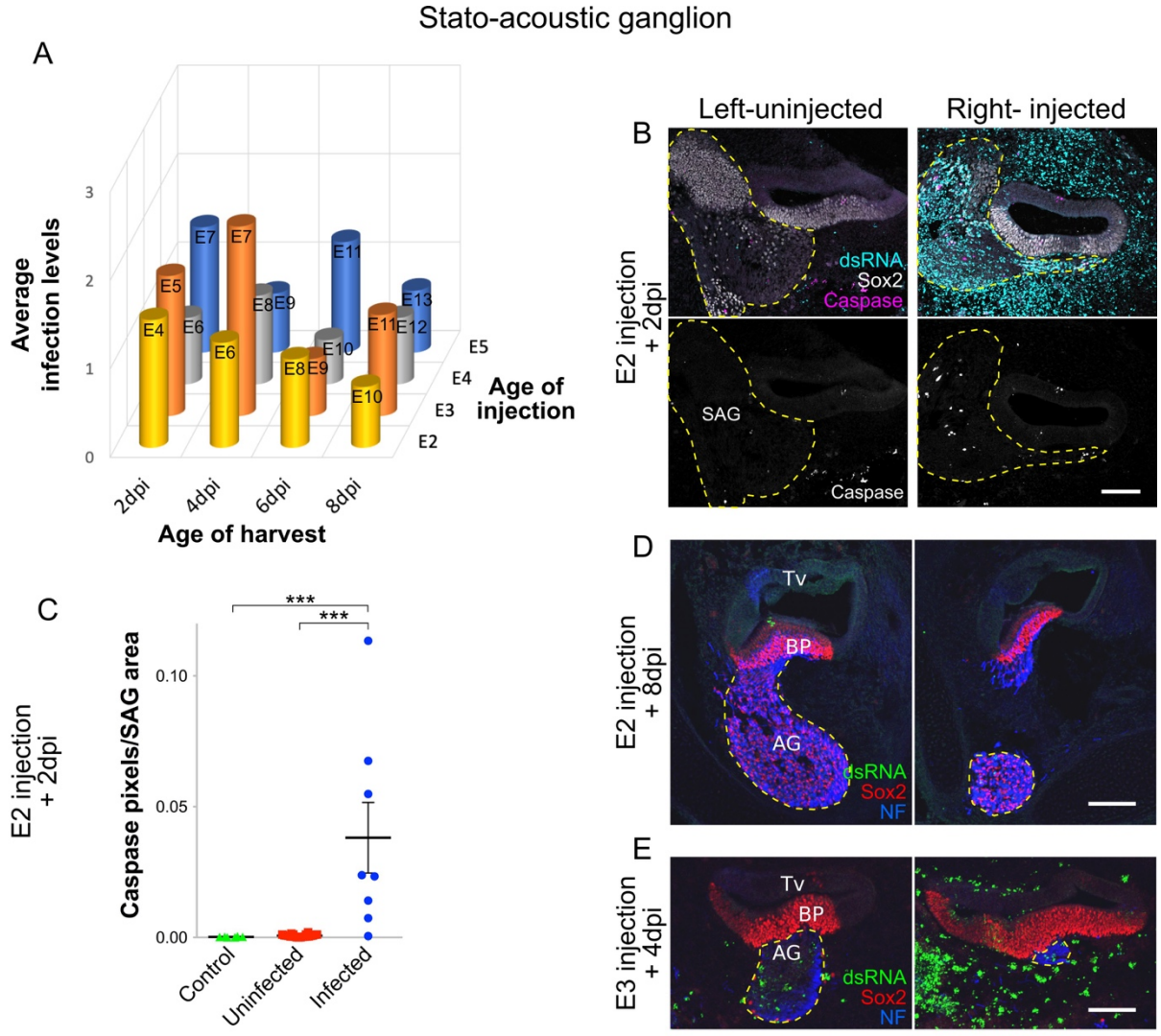
Stato-acoustic ganglion
A
Average infection levels
Age of harvest
2dpi
4dpi
6dpi
8dpi
Age of injection
E2
E3
E4
E5
B
Left-uninjected
Right- injected
E2 injection + 2dpi
dsRNA
Sox2
Caspase
SAG
C
E2 injection + 2dpi
Caspase pixels/SAG area
Control
Uninfected
Infected
D
E2 injection + 8dpi
Tv
BP
AG
dsRNA
Sox2
NF
E
E3 injection + 4dpi

4.2.5 Peak of infection of cochlea at the stages of mid-maturation

ZIKV-associated inner ear defects have primarily been reported in the context of the auditory dysfunction. We thus pursued additional analysis of sensory cochlear (or BP) infection following ZIKV injections. We had expected the cochlea to be more susceptible to ZIKV infection during the early stages of development, when the cells in the sensory domain are actively cycling than the later post-mitotic stages. However, we observed a different trend: for all ages of injection, later stages of harvests show higher levels of BP infection compared to the shorter harvests (Figure 4-6A). If we disregard the age of injection and only focus on the age of harvest after ZIKV infection, we observe that E9-E13 BPs present with the highest levels of infection, with a peak at E11 (Figure 4-6B). At these ages, the mechanosensory hair cells of the BP are all post-mitotic and are starting to differentiate (Katayama and Corwin, 1989). Thus, rather than the Sox-positive prosensory cells of the BP being the preferred target of ZIKV in the developing cochlea, it may be the newly post-mitotic, young hair cells that are most susceptible to ZIKV infection. Additionally, morphological defects of the cochlear duct were not observed very often; out of the 109 embryos analyzed, only one animal showed severely altered cochlea in the injected ear with the sensory domain reduced.

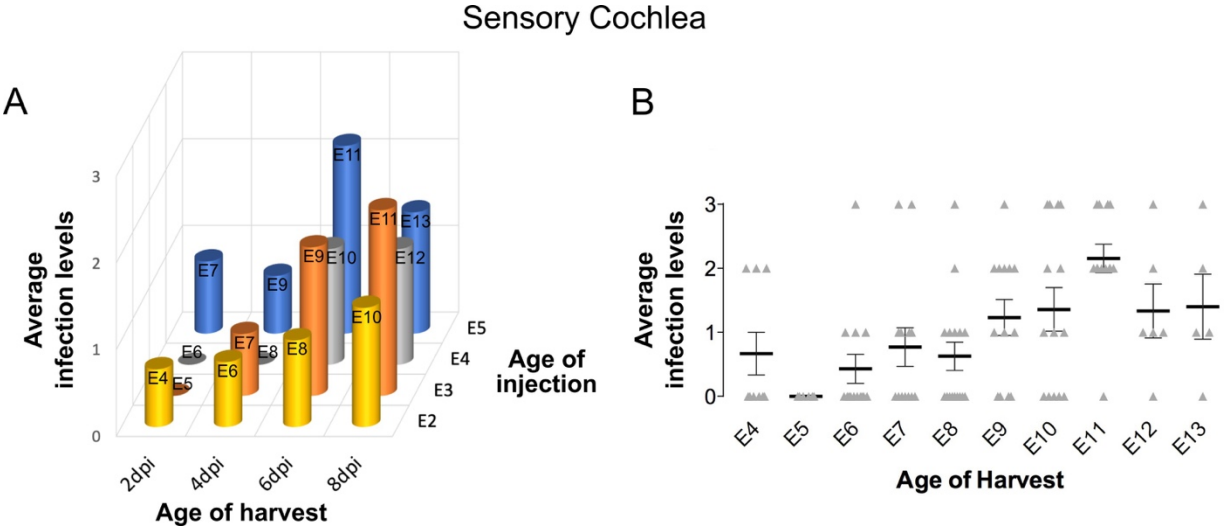

Figure 4-6 ZIKV infection results in high infection of the sensory cochlea (BP) after hair cells are borne.

(A) A three-dimensional histogram shows temporal trends of infection levels in the BP as a function of both the stage of injection (E2-5) and the days-post-injection (2-8dpi; age at the time of harvest is labeled on each bar) ($p<0.0001$; Two-way ANOVA; dpi is a significant variable, but age of injection is not). (B) Infection plotted against the age of harvest irrespective of the age of injection, shows that the peak of the BP infection is around E11 ($p<0.001$; Non-parametric One-way ANOVA test). Abbr.: dpi, days-post-infection.

4.3 Conclusions and Discussion

Congenital hearing loss in newborns is a common consequence of vertically transmitted viral infections, such as the TORCHES agents (TOxoplasmosis Rubella Cytomegalovirus HErpes Syphilis). Due to the impaired regenerative abilities of the mammalian inner ear, hearing aids and cochlear implants are the primary methods of restoring some function in these cases. Some types of progressive hearing loss can be treated or controlled with anti-viral therapy (Cohen et al., 2014). Hearing loss was detected in around 6% of the patients with ZIKV-associated microcephaly with diminished oto-acoustic emissions and auditory brainstem responses, indicating a sensorineural cause of the impaired audioception instead of a conductive blockage (Leal et al., 2016a; Leal et al., 2016b; Moore et al., 2017). The mothers to these microcephalic babies presented infection symptoms in the first four months of pregnancy, a time window that overlaps with inner ear morphogenesis and cell fate specification (Leal et al., 2016b; Lim and Brichta, 2016). Furthermore, the unilateral or bilateral hearing loss hints at a peripheral auditory pathway defect rather than a central cause (Leal et al., 2016b). ZIKV infected adults can also present with transient hearing loss (Vinhaes et al., 2017). A study in infected pregnant mice shows that the 25–66% of the infected pups presented with hearing impairements depending on the test frequency for the auditory brainstem response testing (Julander et al., 2018). Nonetheless, the cellular mechanisms underlying sensorineural hearing loss associated with congenital Zika syndrome are unknown and the incidence is probably underreported due to most of the case studies filtering for microcephalic patients (Mittal et al., 2017). This situation argues in favor of developing a laboratory model of studying inner ear sequela to *in utero* ZIKV exposure.

ZIKV is a known neurotropic pathogen that most likely mutated to become much more potent over the last 70 years (Dick, 1952; Li et al., 2016c; Miner and Diamond, 2017; Pettersson et al., 2016; Wang et al., 2018; Yuan et al., 2017; Zhu et al., 2016). ZIKV efficiently infects the developing central nervous system in the incidence of a congenital infection, targeting cells such as neural stem cells and glia (Retallack et al., 2016). The inner ear is a placodal organ system that comprises of several neural-like cells over the course of its development- the neuroblasts of the SAG, prosensory/sensory domains of the inner ear- that are accompanied by non-sensory cells and tissues that subserve distinct functions (Fekete and Wu, 2002; Groves and Fekete, 2012; Knowlton, 1967).

The neuro-sensory domain of the otocyst is the source of neuroblasts that delaminate from the otic epithelium to form the bulk of cochleo-vestibular ganglion (Fekete and Wu, 2002). The

cells of the neuro-sensory domain, the resulting prosensory domains of vestibular and auditory organs, as well as the glial or satellite cells of the statoacoustic ganglion express Sox2, a classic marker for neural stem cells of the ventricular zone in the brain (Ellis et al., 2004; Fekete and Wu, 2002; Groves and Fekete, 2012). Neuroblasts delaminating from the closing otic cup and the otocyst switch from being Sox2-positive to Islet1 or Neurogenin1-positive as they begin to differentiate; Islet1 being yet another marker for immature neurons of cranial and sensory ganglia and motor neurons (Evsen et al., 2013; Neves et al., 2011; Steevens et al., 2017). We hypothesized in view of the neurotropic nature of ZIKV, the SAG would be susceptible to infection, and that similar to the developing brain, the susceptibility would reduce over time. Our data showed that though only about a third of the embryos analyzed presented with medium to strong SAG infection, the E2 or E3 otic injections resulted in the strongest infection levels in the SAG. Possibly, the delaminating neuroblasts from the otic epithelium could have picked-up the ZIKV virions injected in the otocyst and carry the infection medially to the SAG. Less robust infection at later ages of development is logical due to maturation of neurons in the ganglion. Furthermore, several occurrences of a stunted auditory ganglion were observed after ZIKV infection. Anti-activated caspase-3 staining shows higher caspase activity in the infected SAG two days after E2 injections in contrast with the contralateral ear; quantitative evidence of ZIKV-associated increase in cell death in the SAG bolsters this observation.

In addition to Sox2, numerous neurogenic marker such as the basic-helix-loop-helix family of transcription factors (Neurogenin1, Atoh1, Neurod1) are important during sensory organ development of the inner ear (Table 4-1) (Evsen et al., 2013; Groves and Fekete, 2012; Wu and Kelley, 2012). Thus, we expected the sensory epithelia of the inner ear labyrinth to be more susceptible to ZIKV infection compared to the non-sensory domains. This hypothesis was supported by our unpublished observations 7dpi after E2 brain injections (follow-up of Chapter 3 or (Thawani et al., 2018). Six out of the 10 embryos immunolabeled for dsRNA showed positive staining in the sensory cochlea (5 out of 10) or the sensory saccule (3 out of 10), and no infection was detected in the non-sensory tissue except for 1 case with weak infection of the tegmentum vasculosum (Figure 4-7). However, no obvious preference of sensory over the non-sensory tissue was apparent following direct injections into the otocyst, where access to the target tissues should be more immediate (Figure 4-3C).

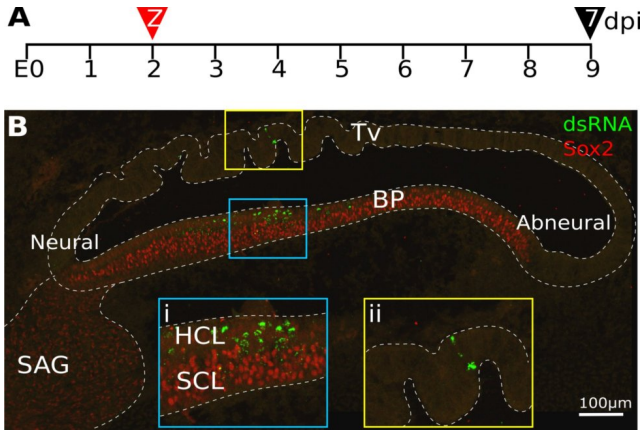

Figure 4-7 ZIKV infection spreads to the sensory inner ear epithelium after brain injection.

(A) Timeline with brain injection at E2 and harvest at 7dpi. (B) Example of an infected 7dpi BP labeled with dsRNA (green, infection), Sox2 (red, sensory domain) shows virus in i) the hair cell layer (HCL) and supporting cell layer (SCL); and ii) tegmentum vasculosum (Tv). Abbr.: BP, basilar papilla; SAG, statoacoustic ganglion.

As the newborn studies primarily report hearing dysfuction as a consequence of ZIKV infection, we focused further on the infectability of the cochlear duct. The data in Chapter 3 suggested that peak levels of ZIKV RNA copies in the brain were observed 2-3 days after ventricular injections. Hence, we expected the sensory cochlea as well to present higher levels of ZIKV infection in the short-term harvests (2 to 4dpi) rather than 6 to 8dpi. Moreover, we anticipated the actively dividing multipotent stem cells of the BP more likely to be susceptible to ZIKV infection, instead of when the apical layer stops dividing, all the hair cells are borne and begin differentiating (Katayama and Corwin, 1989). Intriguingly, the later stages of observation presented with higher levels of ZIKV infection, particularly E9 to E13, when the cochlea is maturing. Arguably, as the hair cells mature and assemble their neurosecretory machinery and synaptic junctions with afferent and efferent neurons, it could make them seem similar to immature neurons, and therefore susceptible to ZIKV infection; or perhaps the afferents infected at earlier stages of harvest serve as the source of virus delivered to the hair cells at later stages. It remains to be seen whether the fully matured basilar papilla is permissive to ZIKV.

ZIKV is also recorded to infect cranial neural crest cells (Bayless et al., 2016) that arise during neurulation. Neural crest cells contribute to certain cell populations in the developing inner ear as well, particularly the highly vascularized stria vascularis (mammalian equivalent of avian

tegmentum vasculosum, non-sensory cochlea) that is important for maintaining the high potential of the endolymph and nourishing the labyrinth (Steel and Barkway, 1989) and the SAG (D'Amico-Martel and Noden, 1983). Infection of these neural stem cell-derived populations can also result in auditory dysfunction.

Two major defects after ZIKV injection to the inner ear observed were undersized auditory ganglion (as described above) and faulty canal morphogenesis. Around E6-7 in chicken embryos, the fusion plates located in the center of the canal pouches undergo massive programmed cell death and the edges of the pouch seal off to form semicircular canals (Fekete et al., 1997). In certain ZIKV injected embryos, the anterior and posterior canals did not appear fully matured and separated when compared to the uninjected contralateral ear and age-matched controls. A pre-fusion pouch-like outgrowth was present instead. This is a novel finding in regard to the congenital Zika syndrome since a vestibular dysfunction symptomatology has not been previously described in ZIKV infected babies to our knowledge.

We also observed a very frequent occurrence of periotic mesenchymal infection as a consequence of ZIKV injection in the otic primordium or otocyst; periotic mesenchyme tissue is important for inner ear morphogenesis (Liang et al., 2010). This suggests that ZIKV can cross the basement membrane of the otic epithelium and infect the surrounding tissue; or the virus escaped with during the neuroblast migration to the surrounding mesenchyme. Perhaps the virus could also circulate in the microenvironment, multiplying and thriving until the sensory tissue at later stages of development, such as the differentiating BP, is ready for infection.

A key finding of this study was the absence of reliably robust infection of the inner ear epithelium. Most of the ZIKV-injected ears had considerably fewer infected cells compared to our results in the developing brain (Thawani et al., 2018), perhaps due to limitations in the injection volume that the otocyst can accommodate compared to the neural tube. This relatively sporadic infection created a challenge to explore mechanisms (such as cell death) that might explain the major phenotypic defects observed (canal truncation, cell loss in the SAG).

In a parallel study in the Fekete laboratory, we are using *in vitro* mouse cochlear cultures to study ZIKV pathogenesis where we can potentially get more even and robust infection by uniformly exposing the sensory tissue to high-titer ZIKV (Munnamalai and Fekete, 2016).

In summary, the chicken embryo is indeed a suitable model organism to study inner ear development and teratogen-associated defects. Although, we do not observe very strong infection of the inner ear epithelium, our data show that the immature SAG is susceptible to ZIKV infection

and so is the sensory as well as non-sensory tissue of the labyrinth. Additionally, we report two novel findings as sequela of embryonic ZIKV infection: damaged auditory ganglion, and dysmorphic semi-circular canals. Much is yet to be uncovered about the congenital Zika syndrome, and this report attempts to investigate the sensory system disorders associated with the disease.

CHAPTER 5. OTHER ROUTES OF ZIKA VIRUS INFECTION

5.1 Chicken embryo as a ZIKV transmission model

ZIKV is neurotropic virus, primarily transmitted through a focal infection by mosquito bites, and across the placental barrier *in utero* (Gyawali et al., 2016; Rasmussen et al., 2016). Animal models indicate that after focal or systemic inoculation in adults or pregnant mothers, the virus can cause viremia in the infected individual and reach the neural tissue in the gestating fetuses and the adults (Adams Waldorf et al., 2018; Adams Waldorf et al., 2016; Aliota et al., 2016; Dudley et al., 2016; Lazear et al., 2016; Miner et al., 2016a; Rossi et al., 2016). As described in Chapters 3 and 4, we investigated brain and inner ear injections to understand the spatiotemporal preference of ZIKV infection in those organ systems by direct injection in the organ system of interest. Interestingly, in most experimental subjects, we observed infection of the mesenchymal tissue, indication the virus can be maintained in the surrounding tissue and possibly the circulatory system as evidenced by the injections to the inner ear that could result in strong sensory infection as late as 8 days after the initial viral delivery. **We thus hypothesize that the ZIKV inoculum delivered to the peripheral tissue of the developing chicken embryo could reach the brain eventually**.

To attempt to establish a chicken embryonic model for transmission, we explored other, rather indirect, methods of ZIKV delivery to see whether and when ZIKV spreads to the brain and vascular tissues. ZIKV was injected into the limb bud (infection of peripheral soft tissue), blood stream (infected circulatory system), and chorio-allantoic membrane (possible transmission across the extra embryonic layers).

5.2 Results

5.2.1 Blood injection in E3 chicken embryos

Around 8 to 10nl of $9.6x10^7$PFU/ml ZIKV was injected into the anterior carotid vein at E3 (Figure 5-1A-B), and the viral mixture with the fastgreen dye was observed to travel to the heart, since the major vessels are relatively close to the surface of the embryo at these early stages. We presumed that after reaching the heart, virus would be pumped throughout the circulatory system. To analyze the viral loads through the embryo, samples of brain and heart were harvested at 1 to 3dpi. For younger stages (E4-5), the whole brain or a sagittal half was taken, and the entire heart

was dissolved in TRIzol for RNA extraction. For older stages (E6 and above), chunks were taken from the dorsal roofs of the anterior forebrain and midbrain to dissolve in TRIzol; the apical tip of the heart was harvested. Quantitative RTPCR on these samples show an increase in the viral levels in the first 2 days post infection, with peak of viremia at 2dpi (Figure 5-1C). ZIKV RNA levels in the brain were comparable to the viral load at 2-3dpi after E2 neural tube injections (10^5 ZIKV RNA copies/100µg of total RNA in brain; Chapter 3); though the heart showed around 10-fold higher infection after the bloodstream injections compared to the E2 neural tube injections (10^5 ZIKV RNA copies/100µg of total RNA in heart; Chapter 3). Due to the small sample sizes of these experiments, we verified the trends observed with qRTPCR using agarose gel electrophoresis performed with PCR products amplified for ZIKV and GAPDH (housekeeping gene). In Figure 5-1D, each lane represents one sample; GAPDH levels look similar across all the samples, however, ZIKV levels look the highest for 2dpi samples for brain and heart tissues.

Both the 3dpi embryos used for PCR reactions were also cryosectioned dorsal to ventral through the head to examine the neuroepithelium for infection by fluorescently immunolabeling with dsRNA antibody. Additionally, 1 embryo each was harvested for immunostaining for ages 1dpi and 2dpi. Histology presented barely any infection in the brain; however, all 4 embryos had dsRNA signal (or ZIKV infection) in the mesenchymal tissue in the body and often around the neuroepithelium (data not shown). The survival curve after blood injections shows 100% lethality by 15dpi (similar to brain injections) and 7dpi as the median age of survival (yet again similar to brain injections) (Figure 5-1E). Since these embryos had relatively little infection in the brain parenchyma, this leads us to speculate that it is systemic viremia, rather than a sequela of brain infection, that underlies the time course of lethality in ZIKV-infected chicken embryos.

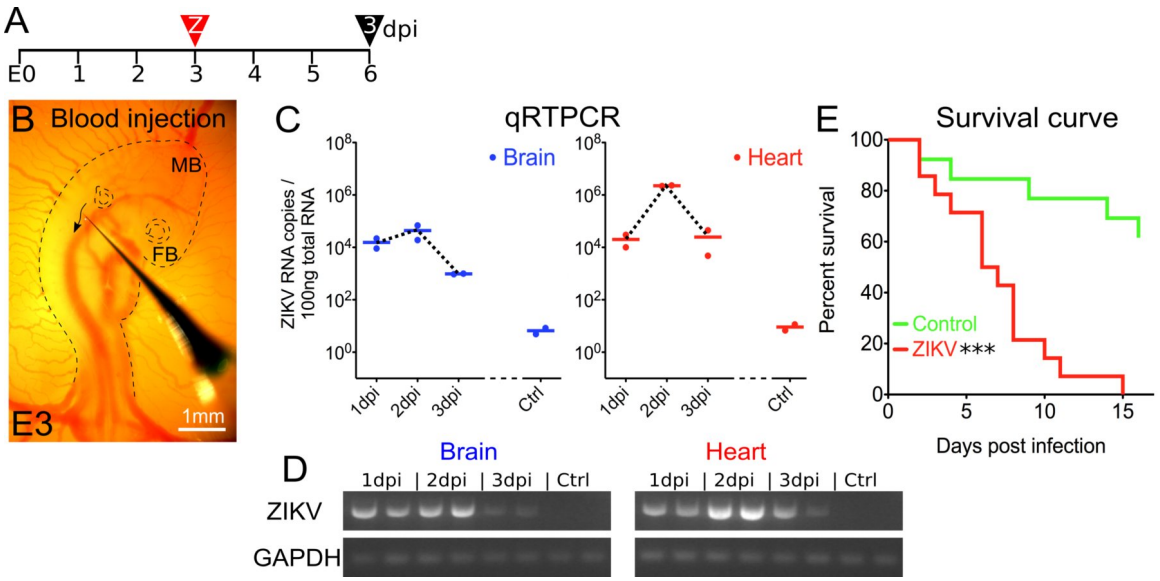

Figure 5-1 ZIKV injection in the bloodstream

A, B) On E3 ZIKV was injected into the anterior carotid vein (black arrow, B) and tissue was harvested at 1 to 3dpi. C) Analysis by qRTPCR showed ZIKV viral load initially increasing in the brain (n=2 each condition; $p<0.001$; one-way ANOVA test) and heart tissue (n=2 each condition; $p<0.001$; one-way ANOVA test) over two days. Bars represent mean. D) PCR gels for the same samples as panel C, ZIKV amplicons represented by the band intensity and GAPDH as the housekeeping gene. E) A survival study in which all ZIKV-injected embryos died by 15dpi (before hatching) and the survival was significantly lower compared to mock-injected controls (n=13 controls, 14 ZIKV; $p<0.001$; Log rank test).

5.2.2 Limb-bud injection in E4 embryos

We injected the anterior forelimb bud at early E4 (Figure 5-2A-B), soon after the limb-bud is of a significant size to inject. Five separate foci on the limb bud were injected and the experimenters controlled for the approximate amount of inoculum for each embryo. Brain, heart and limb samples were collected for qRTPCR and PCR gel analyses as described for blood vessel injections. For 1 and 2dpi harvests, sagittal half of the brain, apical piece from the heart and distal 1/3rd of the injected forelimb were harvested and dissolved in TRIzol for RNA isolation. For 4 and 6 dpi samples, pieces from the dorsal roof of the forebrain and midbrain, forelimb sample distal of the carpals, and apical tip of the heart were harvested for RNA extraction; ZIKV infected limbs appeared deformed at these ages compared to the respective controls. Unfortunately, the heart and limb RNA samples were lost during the experiments due to less than optimal RNA extractions. ZIKV genome was detected by qRTPCR and PCR gels (Figure 5-2C-D) in the brain tissue and viral RNA was noticeably increasing over time, indicating viral replication. Noticeably, the ZIKV RNA copy levels were at least 10 times less than that observed after blood and brain injections.

After harvesting tissues for qRTPCR experiments, the remaining head, heart and injected forelimb were fixed and cryosectioned for histology. Three ZIKV injected embryos harvested at 4 and 6dpi each were analyzed by fluorescent labelling for dsRNA in the brain, heart and forelimb tissues. DsRNA immunolabeling was very weakly detected in the neuroepithelium of the 6dpi brains; the mesenchymal tissue around the brains was infected much better (data not shown). Intriguingly, the limb muscles (6 out of 6 embryos), the ocular muscles (5 out of 6 embryos), and even the heart tissue (5 out of 6 embryos) showed dsRNA positive regions, suggesting that the chicken muscles cells are also susceptible to ZIKV. Embryos at 1 and 2dpi are yet to be analyzed by histology. Ocular muscle abnormalities (Melo et al., 2016) and limb contractures (Moore et al., 2017) have been previously detected in ZIKV infected babies. Figure 5-2E shows an example of ocular muscles of a 6dpi embryo where striated actin (detected using phalloidin) to identify myofibrils is co-localized with dsRNA.

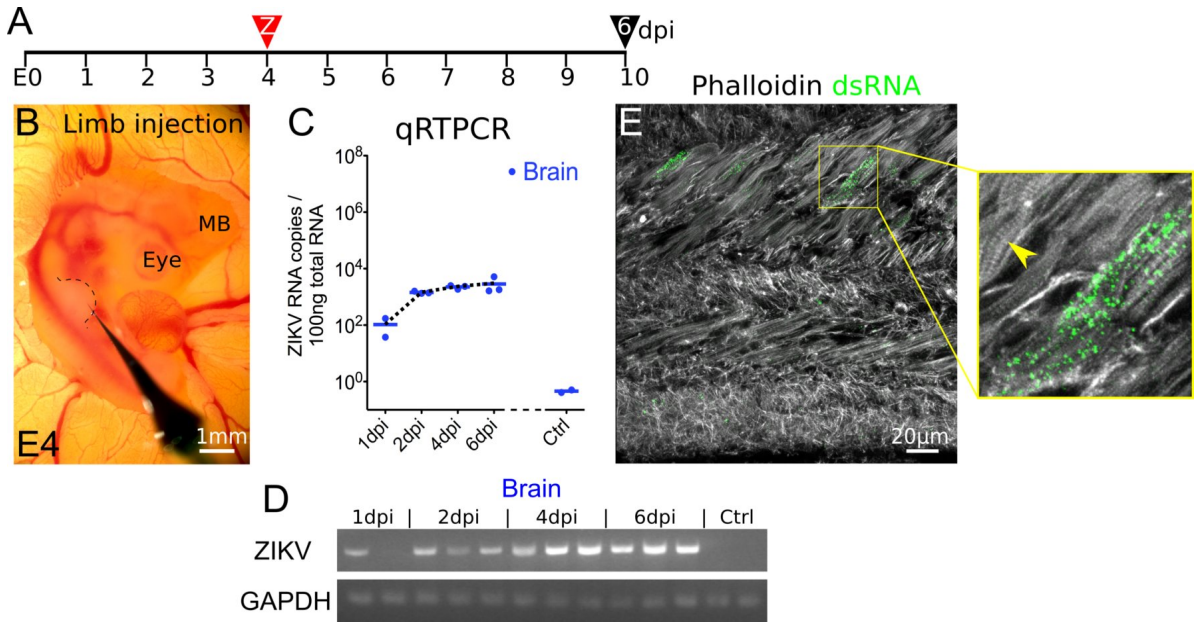

Figure 5-2 ZIKV injection in the limb bud

A) ZIKV was injected into the right forelimb bud at E4 (B) and tissue was harvested at 1 to 6dpi. C) Analysis by qRTPCR showed ZIKV viral load initially increasing in the brain (n=2 to 3 each condition; $p<0.0001$; one-way ANOVA test) over time. Bars represent mean. D) PCR gels for the same samples as panel C, with ZIKV amplicons represented by the band intensity and GAPDH as the housekeeping gene. E) Co-labeling for dsRNA (green) and phalloidin (grey) showed that eye muscles (panel E) and limb muscles close to the site of infection were primarily infected (data not shown; n=3 out of 3). Inset shows muscle like striations (arrowhead) stained with phalloidin.

5.2.3 CAM infection in E10 embryos

We infected the chorioallantoic membrane (CAM) (extra-embryonic layers) at E10 (Figure 5-3A-B) by ejecting 200µl of $9.6x10^5$ PFU/ml of ZIKV inoculum (100-fold diluted than the stock). At 1, 2, 4, and 6dpi, a piece from the anterior forebrain and a piece from the apical tip of the heart was dissected and dissolved in TRIzol for RNA extraction. The remaining brains were dissected out, processed and embedded for histology (n=2 for each condition). With qRTPCR and PCR gels for brain and heart tissue samples, we observed an increase in ZIKV RNA copies over time (Figure 5-3C-D), however the viral RNA levels were lower than other methods of injections, particularly for the heart samples.

At these ages of observation, we were expecting to observe low levels of infection as the Sox2-positive periventricular zone of the neural tissue was very thin. It came as no surprise that the bulk of the brain (especially the forebrain) showed very little infection, however one out of the four embryos observed at 4 to 6dpi showed some infection at the very surface of the brain, perhaps close to the blood-brain-barrier. Embryos harvested at 1 and 2dpi are yet to be analyzed by histology. Interestingly, 3 out of 4 embryos showed infection of the external granular layer of the cerebellum at 4 to 6dpi, more remarkable at 6dpi (Figure 5-3E). Lectin (*Lens culinaris* agglutinin) labels the endothelial cells of the chicken embryo (Jilani et al., 2003), hence the vascularized pia matter between the folia of the cerebellum was labeled with lectin. Notably, the external granular layer has persistent neurogenesis needed to generate the late-born granule cells (Ryder and Cepko, 1994), thus this progenitor population could be susceptible to ZIKV infection.

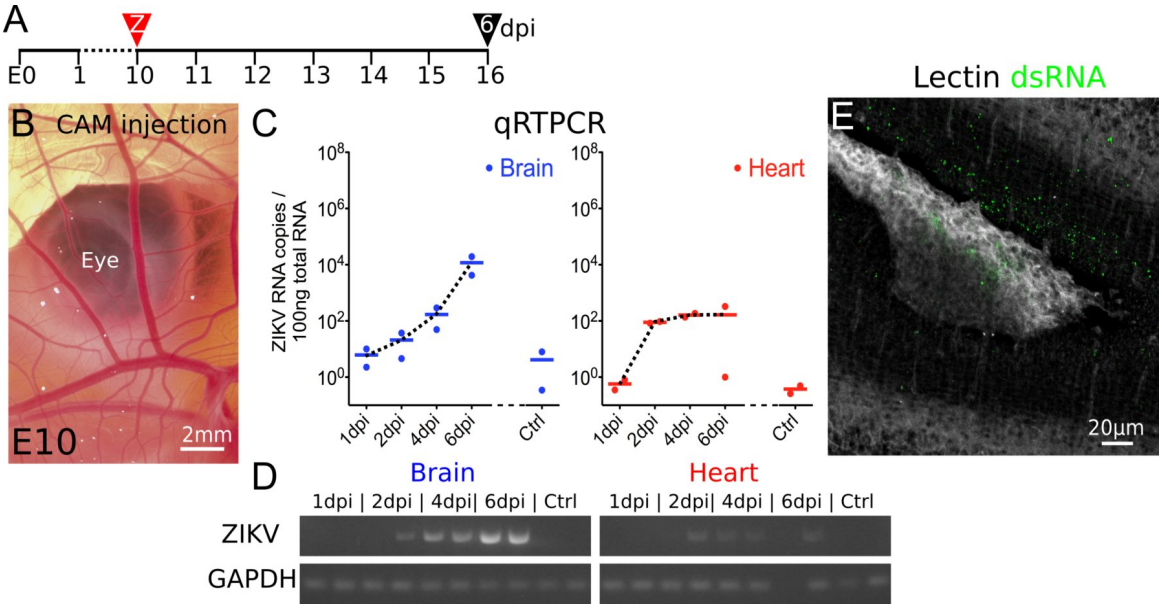

Figure 5-3 ZIKV infection in the chorioallantoic membrane

A) ZIKV was dripped onto the chorio-allantoic membrane (CAM) at E10. (B) tissue was harvested at 1 to 3dpi. C) Analysis by qRTPCR showed ZIKV viral load increasing in the brain (n=2 each condition; $p<0.05$; one-way ANOVA test) and heart tissue (n=2 each condition; $p=0.06$; one-way ANOVA test) over time. Bars represent means. D) PCR gels for the same samples as panel C, with ZIKV amplicons represented by the band intensity and GAPDH as the housekeeping gene. E) Labeling for dsRNA (green) and lectin (grey) showed that ZIKV was present primarily in the cerebellum (n=3 of 4 embryos), close to lectin-positive vasculature.

5.3 Conclusions and Discussion

Studies in immunocompromised mice models and non-human primates have shown evidence of bioactive replicating virus in brain tissue through qRTPCR and plaque-assay analyses after non-neural ZIKV delivery (Dudley et al., 2016; Li et al., 2016c; Miner and Diamond, 2017). Furthermore, viral delivery into the amniotic space of chicken embryos between E2 and E5 resulted in microencephaly at E15 to E20 tested via MRI (Goodfellow et al., 2016), however histological data is lacking. Our data shows viral RNA copy numbers increasing over time in the brain tissues after the non-neural methods of infection: blood, limb bud, and CAM at E3, E4 and E10 respectively. qRTPCR data for brain and heart tissues with each method of infection shows statistically significant linear trend; these statistical analyses must be interpreted cautiously due to low sample sizes (n= 2 to 3). However, the dsRNA immunolabeling at various stages of harvests post injection did not show a robust infection in the brain as we previously observed after the E2 neural tube injections (Chapter 3); the exception being at 6dpi after the CAM infections (E16) when some significant neural tissue infection was observed in this study.

We speculate how qRTPCR can present strong levels of ZIKV genome in the tissue samples and yet the histology showed no dsRNA labeling for the same embryos. One possibility is that the viral genome is not replicating as much in the neural tissue and hence no dsRNA immunostaining; the viral particles captured in the TRIzol samples could have primarily come from the circulatory system or the cerebrospinal fluid, and these would probably be lost from tissue processing, washes and the sectioning procedures. It is also possible that ZIKV is not yet at high enough level in the central nervous system and examination at additional few days after the last timepoints we studied might result in a noticeable level of infection, as detected with histology.

The three aforementioned injection methods were tested to explore different routes of infection, to assess whether other delivery routes can reach progenitors in the central nervous system and to observe ZIKV tropism for non-neural tissue types. Blood inoculation primarily yielded a mesenchymal (systemic) infection, but little to no brain infection. Limb bud injections largely showed muscle tissue infection in the limb, behind the eyes and the heart, again with little to no infection in the neural tissue. One can argue that due to the ability of ZIKV to rapidly adapt to the tissue target or the host organism (Dick, 1952; Miner et al., 2016b), it is possible that injection into a non-neural tissue, such as the forelimb, forced the virus to retain certain random mutations post replication that make it more suitable to infect that foreign non-neural tissue. CAM injections, however, resulted in infection of the circulatory system (heart tissue as evidenced by

qRTPCR), indicating that ZIKV transmitted through the extraembryonic layers into the bloodstream; the virus also spread to the cerebellum in a layer that lies in close apposition to the vasculature. The infection in superficial layers of the cerebellar folia correlates well with the fact that at these stages of cerebellar development, the external granular layer will comprise of some progenitor cells (Ryder and Cepko, 1994). We, thus, observe a wide spectrum of tissues that ZIKV can infect after non-neural routes of viral delivery.

CHAPTER 6. SUMMARY AND FUTURE DIRECTIONS

Congenital Zika Syndrome is not well understood yet. In addition to the signature microcephalic phenotype, fetal ZIKV infection can result in a myriad of other symptoms: (1) brain defects- calcifications, ventriculomegaly, brainstem hypoplasia, cerebellar hypoplasia; (2) sensory organ dysfunctions- chorioretinal atrophy, ocular muscle defects, lens subluxation, colombomas; and (3) movement disorders- joint and muscle contractures, difficulty swallowing; and more (Moore et al., 2017). Various cellular and animal models present strong evidence that ZIKV preferentially infects neural progenitor cells and causes increased cell death and reduced proliferation in the brains, ensuing microcephaly (Li et al., 2016c; Miner and Diamond, 2017). This study presents a low biohazard risk and easily accessible vertebrate model of development—the chicken embryo-- to study such severe congenital diseases for better understanding of the pathogenesis. Moreover, the chicken embryonic system has potential as a relatively higher throughput *in vivo* model for therapeutic testing purposes (Davey and Tickle, 2007). We directly infected the chicken embryos *in ovo* by delivering high titer ZIKV to the neural tube (E2; Chapter 3), inner ear (E2, 3, 4, and 5; Chapter 4), bloodstream (E3; Chapter 5), limb bud (E4; Chapter 5), and chorioallantoic membrane (E10; Chapter 5), and sought for evidence of infection in regions of interest.

By directly injecting the **neural tube at E2**, we attempted to address whether all the neural progenitor populations are equally infectible at early stages of brain development. Infection of the chicken neural tube resulting in a statistically significant microcephalic phenotype within 3 days after injection; the phenotype penetration was indeed variable with only 25% of the 3dpi embryos presenting with severe microcephaly. Upon histological investigation, instead of a uniform infection all along the neuroepithelium that is rich in Sox2-positive neural progenitors at the periventricular region, we found foci of heavy infection, or 'hot-spots'. These 'hot-spots' of ZIKV infection were associated with several key regions of the brain known for their role of morphogen-secreting signaling centers that are essential for fate specification and patterning of the neighboring tissue. Our data demonstrated that upon heavy infection, not only were the transcript levels for some of these morphogens (SHH, FGF8B, BMP7) reduced, some SHH-dependent cell populations (PAX6 and NKX2.2) at the MB basal plate presented with patterning defects. Thus, while ZIKV preferentially infects neural progenitors, it also seems to exhibit differential tropism for specific sub-regions of the developing brain, possibly abating their morphogenic function(s) during

embryonic brain development. Future studies need to address the cause of this differential susceptibility, to identify what is special about the periventricular regions of the morphogen secreting signaling centers.

We need to understand what receptor is responsible for such specificity of ZIKV infection in the developing brains. Similar to DENV, a close phylogenetic neighbor of ZIKV, the TIM/TAM family of receptors, which includes AXL, is thought to be responsible for ZIKV entry into the infected cells (Hamel et al., 2015). The AXL receptor is primarily expressed in the ventricular zone and the sub-ventricular zone in gestating fetal brains where the stem cell population of the neural epithelium resides (Nowakowski et al., 2016), which after all is the primary group targeted by ZIKV in the brain (Li et al., 2016c; Miner and Diamond, 2017). Although, AXL does not exist in the chicken genome, two other family members of the TAM receptor family, TYRO3 and MERTK, share around 40% homology with human Axl (NCBI- Protein BLAST). Furthermore, the GEISHA database of chicken embryonic gene expression (University of Arizona, Tucson) shows that *Tyro3* is expressed in the otic epithelium, the neural tube and the surrounding head mesenchyme around E2 (Darnell et al., 2007). Future experiments will follow up on Tyro3 receptor as a possible point of entry for ZIKV in chicken embryos.

Sensorineural hearing loss is a relatively unfamiliar sequela to congenital Zika syndrome. Stages of sensory organ development in the inner ear involve various neural-like cell populations that could be susceptible to ZIKV infection. Around 6% of newborns exposed prenatally to ZIKV presented with hearing deficits (Leal et al., 2016b), however no evidence of vestibular defects or related balance issues has come to light thus far. A key knowledge gap to understand the ZIKV-associated inner ear defects is the spatial and temporal susceptibility of the developing inner ear to ZIKV infection. To address this, we injected ZIKV into the **chicken otic primordium at E2, 3, 4, and 5**, and systematically harvested tissue at 2, 4, 6, and 8 dpi. Injections resulted in sensory epithelial infection in the vestibular and auditory organs frequently, with non-sensory infection observed nearly just as frequently. Infection was found in the sensory cochlea as late as E13, with the peak of infection around E10-11, when the hair cells have stopped dividing and are mid-differentiation. Two diverse phenotypic defects, though occurring rarely, were found with our experiments: (1) abnormal semicircular canal morphogenesis, and (2) stunted auditory ganglion. The latter is understandable as ZIKV, a known neurotropic virus, could infect the immature neurons and neuroblasts of the developing stato-acoustic ganglia. Current and future experiments in the lab are seeking evidence for ZIKV-mediated cell death in the SAG post infection to explain

the unusually small auditory ganglion. More difficult to explain is the defective canal fusion phenotype. During development, the canal pouches grow and extend dorsally or horizontally until E5, after which the thin epithelium in the middle fuses and undergoes massive programmed cell death in birds, or shrinks away in mammals (Fekete et al., 1997; Knowlton, 1967; Nishitani et al., 2017). To address the mechanism of the defective canal fusion, follow-up experiments should be done for markers like Dlx, Laminin, or Netrin that differentially label the fusion plates (Nishitani et al., 2017; Rakowiecki and Epstein, 2013). Though only a conjecture right now, we also wonder if ZIKV can infect and damage signaling centers of the inner ear important for canal pouch protrusion, fusion, and/or semicircular canal outgrowth (Rakowiecki and Epstein, 2013).

An overarching observation was that in addition to the neural stem cells (Li et al., 2016c), a wide variety of other tissues are infectible with ZIKV, particularly the mesenchymal cells. For almost all the embryos where any dsRNA staining was apparent, indicative of replicating flavivirus (Weber et al., 2006), the mesenchymal tissue was found to be infected, perhaps from the virus transmitting to the circulatory system and resulting in systemic viremia. Particularly with the **non-neural routes of ZIKV infection**, we observed mesenchymal infection more often and evidence of brain infection was limited. Moreover, after the inner ear infections, ZIKV persisted in the mesenchymal tissue. However, infection of the sensory patches, such as the basilar papilla, only appeared at later stages of harvest. We thus speculate whether the systemic infection is demonstrating a chronic infection of ZIKV that might infect and damage more organs of the developing embryo, possibly persist even after the embryonic gestation is complete, or result in inevitable lethality. E2 neural tube and E3 blood vessel injections result in a 100% mortality before the anticipated age of hatching, yet it remains to be investigated whether the other aforementioned methods of infection also lead to embryonic lethality.

Additionally, some evidentiary support is required for addressing how one virus can accommodate to infect and damage several other tissue types in addition to its primary target, neural progenitors in case of ZIKV. It is well known that the flaviviral surface “breathes”, or the surface proteins are dynamic in nature (Sirohi et al., 2016; Sirohi and Kuhn, 2017). We therefore wonder that such an ever-moving epitope on the viral shell makes is suitable to attach to a number of transmembrane receptors on the target cells’ surface, making them susceptible to infection.

Overall, much remains to be understood about ZIKV pathogenesis and transmission, and the chicken embryo could be a suitable vertebrate animal model for this purpose.

APPENDIX A. ACTIVATED ß-CATENIN AS A READOUT OF CANONICAL WNT SIGNALING IN THE RADIAL AXIS OF THE CHICKEN COCHLEA

This section is related to a previously published work from the Fekete laboratory. Munnamalai V, Sienknecht UJ, Duncan RK, Scott MK, Thawani A, Fantetti KN, Atallah NM, Biesemeier DJ, Song KH, Luethy K, Traub E & Fekete DM. (2017). Wnt9a can influence cell fates and neural connectivity across the radial axis of the developing cochlea. Journal of Neuroscience, 37(37), 8975-8988.

A.1 Wnt9a is important for radial axis formation in the chicken basilar papilla

During embryonic development, the otic primordium is exposed to signaling gradients (like Wnts, Fgfs, Bmps) along the anterior-posterior, dorsal-ventral and medio-lateral axes that pattern the cells by specifying their identity and thus creating a complex inner ear (Groves and Fekete, 2012; Wu and Kelley, 2012). Otic placode induction begins with the adjacent rhombomeres secreting Fgfs and giving the ectoderm placode its identity. Further patterning by Wnts compartmentalizes otic and epibrachial placodes, and later on vestibular and auditory regions in the otic capsule (Jayasena et al., 2008; Ohyama et al., 2006; Stevens et al., 2003). Wnt/ß-catenin signaling has been implicated in sensory hyperproliferation in the inner ear in zebrafish, chicken basilar papilla (BP) and mouse cochlea (Jacques et al., 2014; Jacques et al., 2012).

Similar to the mammalian organ of Corti, the auditory organ in the bird, called the basilar papilla (BP), has two mechanosensory hair cell populations that are differentially innervated by afferent versus efferent axons. In the BP, tall hair cells are found on the neural (or medial) side that are robustly innervated by afferent fibers while receiving modest numbers of small efferent boutons (nerve endings). In contrast, short hair cells on the abneural (or lateral) side are primarily innervated by large efferent terminals with small numbers of afferent contacts (Fettiplace and Kim, 2014; Fischer, 1992). Studies have shown that E5 to E7 is a crucial time frame for growth and patterning of the avian cochlea along the radial (neural to abneural) and longitudinal (base/dorsal to apex/ventral) axes (Bissonnette and Fekete, 1996; Katayama and Corwin, 1989; Lang et al., 2000; Sienknecht and Fekete, 2008, 2009). Partly in search of signaling molecules involved in cellular patterning of the inner ear, Sienknecht and Fekete published a comprehensive Wnt expression study in 2009, seeking a candidate molecule present at the right time and place to

influence the specification of hair cells types across the BP. They reported finding a specific Wnt ligand (Wnt9a) expression domain existing throughout the BP at E4.5 (HH25) and eventually restricting to a region adjacent to the neural edge of the prosensory BP by E5 (HH27) (Figure A-1, left). With a source of Wnt9a being asymmetrically localized with respect to the prosensory domain, this molecule became a candidate for being involved in radial axis patterning across the BP. When Wnt9a is overexpressed via ectopic gene delivery to the otocyst, the entire BP assumes a phenotype that is normally confined to the neural half of the organ, including structure and innervation (Figure A-1). This suggests that Wnt9a may function as a morphogen to pattern the radial axis (Munnamalai et al., 2017). In the Wnt9a overexpression ears, the overall width of the BP is greater, and the number of afferent fiber bundles are increased (Figure A-1). This hyper-proliferative effect of Wnt9a overexpression leads us to think it acts via the canonical Wnt/ß-catenin signaling pathway (Munnamalai and Fekete, 2013; Munnamalai et al., 2017; van Amerongen and Nusse, 2009). In fact, Wnt9a is hypothesized to act via the canonical ß-catenin pathway in many developmental situations like chondrogenesis, hepatocyte proliferation and avian atrioventricular cushion development (Matsumoto et al., 2008; Person et al., 2005; Spater et al., 2006). If so, then the BP at these early stages should show evidence of a gradient in Wnt signaling. We began by looking at a readout for canonical Wnt/ß-catenin signaling in controls and Wnt9a-infected specimens.

During canonical Wnt signaling, β-catenin translocates to the nucleus to function as a transcriptional co-activator (van Amerongen and Nusse, 2009). **We hypothesized that as a result of asymmetric Wnt9a signaling, transcriptionally active ß-catenin would have an asymmetric expression across the radial (neural-abneural) axis of the BP, being highest on the neural side (Figure A-2).** Neural regions with exposure to higher Wnt9a protein would have higher transcriptionally active ß-catenin signal. Moreover, Wnt9a overexpression would be predicted to create a uniformly high distribution of signaling, thus disrupting any ß-catenin gradient. Antibodies designed specifically against transcriptionally active β-catenin were used to map its expression, while Serrate 1, Sox2 and neurofilament immunolabeling were used to identify the sensory BP. Either viral capsid protein immunolabeling or Wnt9a in-situ hybridization were used to detect infected cells.

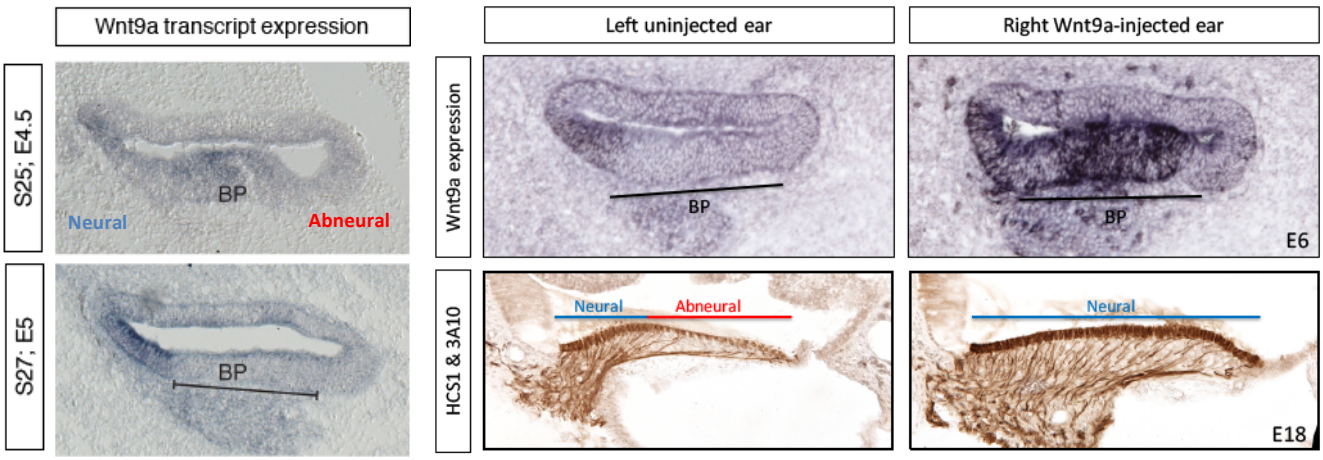

Figure A-1 Wnt9a overexpression can specify neural identity.

Wnt9a transcripts are first detected at E4 across the BP and within one day become restricted to neural-side nonsensory cells (Sienknecht and Fekete, 2009). Normally the prosensory BP develops into neural (tall hair cells) and abneural (short hair cells) phenotypes along the radial axis. When Wnt9a is overexpressed, the neural compartment expands. The mature BP is wider, shows increased innervation and occasionally presents with ectopic vestibular patches on the extreme abneural edge (not shown here) (Munnamalai et al., 2017). BP, basilar papilla; HCS1, hair cell marker; 3A10, axon marker.

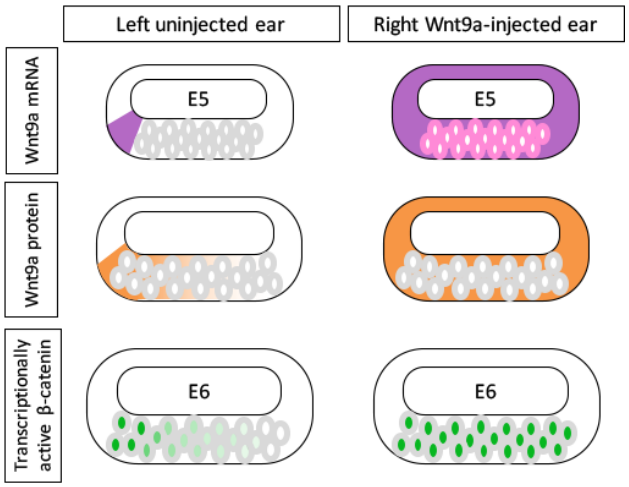

Figure A-2 Hypothesis figure.

The figures show a schematic of E5-6 chicken cochlear duct with round bodies representing the cells of the prosensory region. Left-to-right is the neural-to-abneural axis. We hypothesize that due to asymmetric Wnt9a-mediated canonical Wnt/ß-catenin signaling in the BP, transcriptionally active nuclear ß-catenin would have an asymmetric expression across the neural-abneural axis. Furthermore, when Wnt9a is overexpressed, transcriptionally active nuclear ß-catenin would be upregulated more uniformly across the BP, thus eliminating the gradient and forcing a neural-side identity on the cells.

A.2 Materials and Methods

Activation of the canonical Wnt pathway disrupts the destruction complex comprised of GSK3ß and casein kinase, which in the absence of Wnt ligand will phosphorylate ß-catenin at its N-terminal (S33, S37, T41) and tag it for ubiquitination and eventual degradation. Un-phosphorylated ß-catenin rapidly translocates to the nucleus, where it acts as a transcriptional co-activator of the TCF/LEF complex (Figure A-3 top) (Li et al., 2012; Nusse, 2012; van Amerongen and Nusse, 2009). Antibodies targeted specifically against transcriptionally-active ß-catenin were used for this study (Figure A-3 bottom) (Rhee et al., 2007; van Noort et al., 2002; Zhu et al., 2014).

Although not widely appreciated, pathways other than canonical Wnt signaling are known to employ ß-catenin and use its transcriptional activation of TCF/LEF complex to turn on an array of genes (Figure A-3). We used a nuclear β-catenin specific antibody (DSHB PY489-β-catenin; Antibody B in Figure A-3) targeted against a tyrosine moiety that when phosphorylated makes β-catenin rapidly translocate to the nucleus and interact with TCF/LEF complex to turn on known canonical Wnt signaling genes like Axin2 (Rhee et al., 2007; Zhu et al., 2014). It is important to show that changes in the levels of transcriptionally-active ß-catenin is a result of changes in Wnt9a levels and not these other pathways.

A.2.1 Histology

At E5-E7, tissue was collected, fixed, dehydrated and processed (as described in Chapter 2) either as cryosections through the head or as BP whole mounts. E3 otic vesicles were injected with the RCAS avian retroviral vector that did or did not also encode the Wnt9a transgene. The embryos for this study were either uninjected controls, parent virus (RCAS) injected controls, or RCAS-Wnt9a injected. All RCAS vectors used were of the A-envelope subgroup. The embryos were cryosectioned at the thickness of 10 to 12 μm ideally to obtain as many cross-sections as possible through the cochlear duct at these early stages of development (sets of 3 with 15 sections average in dorsal-to-ventral sectioning).

Tissue sections immunolabeled with PY489 β-catenin antibody [1:1000, mouse IgM, deposited to the DSHB by Balsamo, J. / Lilien, J.; DSHB Hybridoma Product PY489 (stored in -20^{0}C in 1:1 glycerol)] were stained using a heat-induced epitope retrieval method (adapted from (Galli et al., 2014) and counter stained with nuclear label TO-PRO®-3 Iodide (642/661) (1:2000, Life Technologies). To demarcate the boundaries of the prosensory domain, adjacent sections were stained with prosensory markers: Sox2 (1:500, goat IgG[H+L], Santa Cruz, SC-17320), Jagged-

1/Serrate-1 (1:50, rabbit IgG[H+L], Santa Cruz, SC-8303) and/or axonal labeling (3A10 antibody; 1:25 dilution from hybridoma cell supernatant, mouse IgG_1, hybridoma cells deposited to the DSHB by Jessell, T.M. / Dodd, J. / Brenner-Morton, S.). For heat-induced epitope retrieval, tissue sections were first rehydrated with Tris-buffered saline (pH 7.4). Slides were then immersed in 0.01M citric acid in a wide dish and microwaved at 90% power for 5 minutes followed by 10% power for 30 minutes to heat treat the sections for better permeabilization of the lipid membranes. After the permeabilization step, the slides were treated with blocking solution for 30-60 minutes to minimize non-specific antibody binding, followed by overnight primary incubation with the PY489 β-catenin primary antibody. The next day, after 15 minutes of blocking solution treatment, fluorophore-tagged secondary antibodies (Life Technologies, 1:250 to 1:500 dilution) were applied for 1 hour with nuclear label TO-PRO® added to the antibody solution. Sox2-NF slides were not treated with the microwave heat treatment and stained with only the blocking, primary antibody, and secondary antibody steps.

For the BP whole mounts, instead of a heat treatment method, we used a mild detergent treatment: tissue was treated with 1% Saponin for 10 minutes before blocking step, followed by primary antibody and secondary antibody treatments (adapted from Zhu et al., 2014). Whole mounts were triple stained for PY489 β-catenin, Serrate-1, and neurofilament (axons).

The anti-Active-β-catenin antibody (1:500, mouse IgG1-kappa, EMD Millipore 05-665) was specifically designed against a polypeptide for 36 to 44 amino acids of active (dephosphorylated) form of β-catenin dephosphorylated on Serine-37 and/or Threonine-41 (van Noort et al., 2002). The tissue sections were double-labeled for active-β-catenin and Sox2 using the heat induced epitope retrieval method described above.

For the RCAS or RCAS-Wnt9a infected embryos, infection was tested using a monoclonal antibody designed against the gag-epitope of the avian retroviruses (3C2; 1:10 to 1:50, mouse IgG1, deposited to the DSHB by Boettiger, D.; DSHB Hybridoma Product AMV-3C2).

A.2.2 Imaging and Quantification

A.2.2.1 PY489 β-catenin (Antibody B, Figure A-3)

Sox2-NF slides were imaged on Nikon Eclipse E800 microscope (epifluorescence imaging) to determine 10-percentile intervals along the dorso-ventral axis of the BP. The 1st BP section designated was the one where BP innervation first appeared. The last BP section (100%) designated was the one just before an only lagena section (based on innervation and Sox2 domain).

Approximate 10th percentile values were determined for left and right BPs independently. Images of Sox2 and NF were recorded at every ~10th percentile. For quantification of PY489 β-catenin, Nikon Eclipse 90i (confocal imaging) was used to capture images at 20X magnification, and z-axis stacks of 4-5 μm (middle optical slices) were collapsed by taking the 'sum' of the slices (not maximum intensity) using ImageJ (NIH). The top and bottom-most slices were not included to avoid skewing the intensity profile by the cut nuclei that stained very brightly in these sections.

In the collapsed images of PY489 β-catenin, the prosensory domain for each image was divided into bins of equal width (~50μm; same width for each bin; ImageJ) along the radial axis (yellow boxes in Figure A-4). Average β-catenin pixel intensity of each bin was normalized to the intensity of a TO-PRO nuclear stain to control for cell density and plotted as a function of distance from the neural edge. The slope of the linear plot was calculated in MS Excel. The data was compiled showing slopes of the linear best fits of the gradient curves plotted for each BP at 10% intervals from dorsal end of each BP as a box plot, using free online box plot generating tools.

A.2.2.2 Active β-catenin (Antibody A, Figure A-3)

Wnt9a-injected, parent virus (RCAS) injected and uninjected ears were sectioned and stained with anti-active β-catenin antibody (Antibody A; Figure A-3). The prosensory domain was imaged using a Nikon Eclipse 90i (confocal imaging) at high magnification (60X). The prosensory domain was demarcated by Serrate1 or Sox2 and pixel intensity distribution histograms were generated for the left and right BPs using ImageJ (NIH). A Kolmogorov-Smirnov (KS) test was employed for comparing pixel intensity distributions using R-Studio® with the help of statistical expertise from Purdue Statistics Consulting Services (we thank Sophie Sun for the guidance). The KS test is designed to compare sample normal distributions and determine whether they belong to the same population. Hypothetically, upon β-catenin signal upregulation by Wnt9a infection, the pixel intensity histogram would be more skewed towards the higher intensity values compared to the controls, hence the two distributions would be from separate populations of data. Using a KS test, a cumulative difference function (D-statistic) was calculated which represents the maximum difference between the two histograms, and a p-value was generated to indicate statistical significance of the difference.

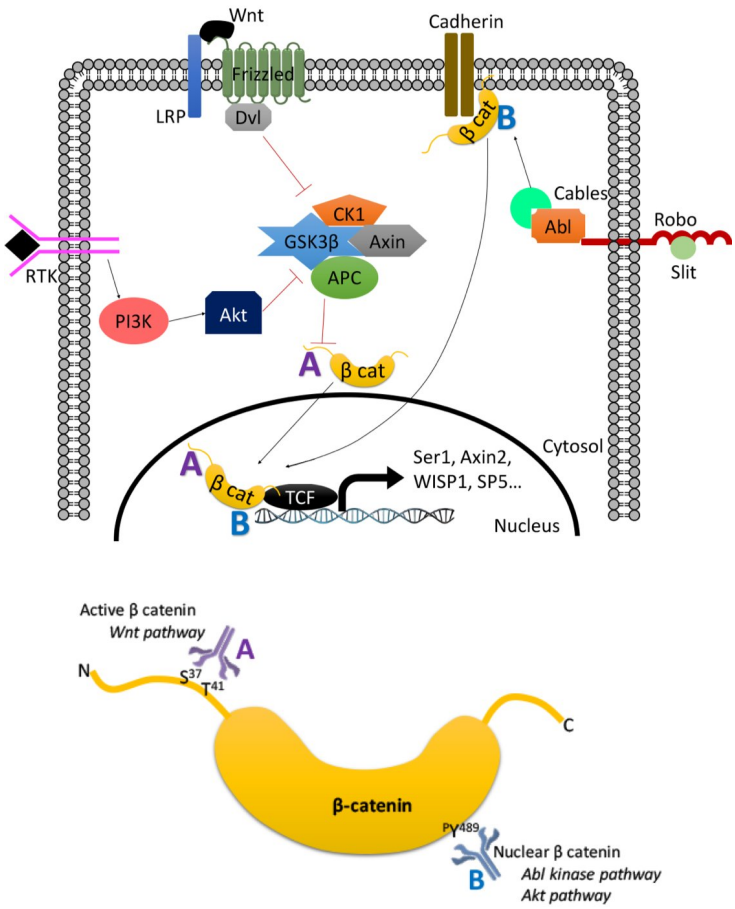

Figure A-3 Detecting β-catenin-mediated signaling with antibodies.

β-catenin is a transcriptional co-activator of TCF/LEF complex downstream of canonical Wnt signaling. We used two antibodies to detect β-catenin. Antibody A detects unphosphorylated S37 and T41 (van Noort et al., 2002). Antibody B detects PY489 phosphorylation. There is also evidence that Abl-kinase and Akt pathways act to regulate β-catenin activation and translocation to the nucleus to interact with TCF/LEF (Rhee et al., 2007; Zhu et al., 2014).

A.3 Results

A.3.1 Profiling PY489 β-catenin expression across the radial axis of the basilar papilla

Starting at E5, Wnt9a transcripts are expressed in the homogene cell region adjacent to the neural side of the prosensory BP. We can assume that the secreted Wnt9a protein diffuses across the radial (neural-abneural) axis. An established gradient of the Wnt ligand across the prosensory epithelium is predicted to activate the downstream signaling pathway in a similar gradient. Hence, we expect to observe a gradient of transcriptionally active nuclear localized β-catenin along the neural-abneural axis (high at neural and low at abneural end) (Figure A-2).

Choosing the time points to study, we considered that the prosensory BP is undergoing its final mitosis and initiation of differentiation between E5 and E8 (Katayama and Corwin, 1989), hence there would be a radial as well as longitudinal variation if a wide range of ages was included in the analysis. Furthermore, the proliferation activity along the radial axis could be varied from the base to the apical end of the cochlea; this makes it important to carefully control for location when attempting to find a read-out of Wnt signaling across the BP that might reflect signaling through Wnt9a. We primarily analyzed E6 embryos at every 10th percentile from base to apex in cross-sections, determined using the adjacent ganglion and innervation (neurofilament staining of axons). Sox2 (neural progenitor marker) staining is used to determine the width of the prosensory domain in cross-sections. Figure A-4 provides an example of an analyzed cochlear duct with the 20% percentile image showing the binning across the BP for signal quantification.

Linear best fit slopes were calculated for every 10^{th} percentile and plotted (Figure A-4) to observe the overall trend of changes in the gradient. An undergraduate researcher from Fekete lab, Sydney Tola, assisted with the cryosectioning, immunostaining, and quantification. The box plot in Figure A-5 represents data collected for 8 animals and the slopes are generally negative, corroborating our hypothesis of asymmetric PY489 β-catenin levels, higher on the neural slide than the abneural side. However, the data were quite variable as shown by long whiskers of the plot and no apparent pattern of the gradient slopes was observed from base to apex. One cautionary note is to consider that literature shows other pathways like Bcr-Abl kinase (Figure A-3; Balsamo et al., 2007) can also drive β-catenin to the nucleus so the observed β-catenin gradient may not be completely contributed by the asymmetric Wnt9a expression. We do not yet know of any correlation between Wnt9a signaling and Bcr-Abl kinase signaling. To complicate matters further, Wnt9a is not the only Wnt ligand expressed in the ear at this age (Sienknecht and Fekete, 2008)

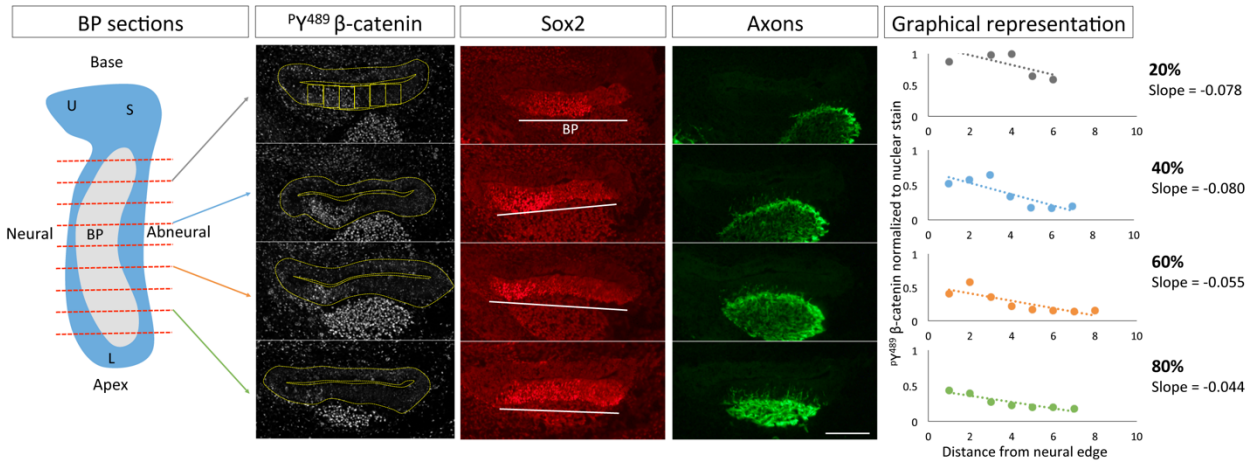

Figure A-4 PY489 β-catenin is expressed in a gradient along the neural-abneural axis of the E6 prosensory BP.

Uninjected embryos sectioned at 10 µm were immunolabeled with PY489 β-catenin antibody (Antibody B). Sox2 and/or axonal labeling were used to demarcate the boundaries of the prosensory domain. For quantification, confocal images were taken with at 20X magnification, and z-stacks of 4-5 µm were collapsed. The prosensory domain for each image was divided into bins of equal width along the radial axis (yellow boxes in upper left image). Average β-catenin pixel intensity of each bin was normalized to the intensity of a ToPro nuclear stain (not shown) to control for cell density and plotted as a function of distance from the neural edge

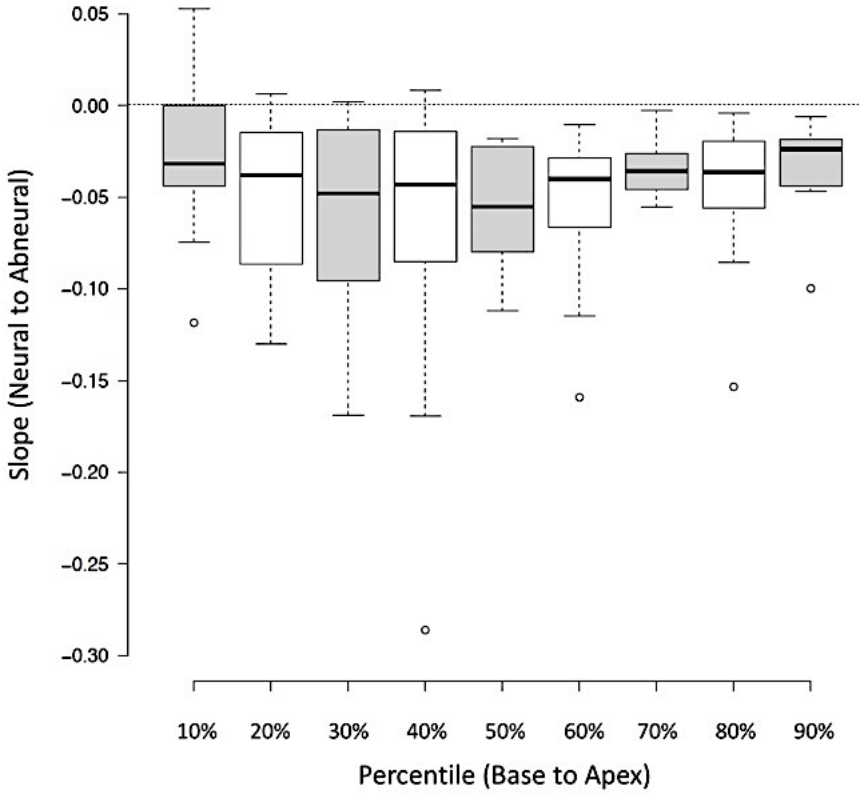

Figure A-5 Summary of PY489 β-catenin gradient along the neural-abneural axis.
The box plot shows slopes of the linear best fits of the gradient curves plotted for 16 BPs (8 animals) at 10% intervals from base. (━) represents the median for each percentile.

(Sienknecht and Fekete, 2009) and other Wnt ligands could activate the canonical Wnt pathway in the similar spatio-temporal fashion and contribute to the β-catenin levels.

A.3.2 Investigating PY489 β-catenin levels downstream of Wnt9a

If Wnt9a operates via the canonical Wnt pathway, we would expect an upregulation in the PY489 β-catenin levels when Wnt9a is overexpressed, as well as increased translocation of the protein to the nucleus. To test that, otic vesicles of 3-day old chicken embryos are injected with a high-titer avian retroviral vector, RCAS(A)Wnt9a, (The RCAS system; http://home.ncifcrf.gov/hivdrp/RCAS/overview.html). Along with the uninjected ear of the same embryo, RCAS(A) virus without the Wnt9a insert serves as another negative control. Whole heads or cochlear ducts were harvested, and the PY489 β-catenin expression was analyzed to observe the predicted augmentation of PY489 β-catenin levels in the Wnt9a injected ears. The E6 embryo we analyzed did not observe any significant changes in the PY489 β-catenin (Antibody B) levels (data not shown) but we tested a day later (E7) and noticed a difference in the cochlear morphology and PY489 β-catenin signal.

Whole mounts of cochlear ducts were stained with PY489 β-catenin and Serrate-1 (known downstream gene of Wnt signaling; known to be expressed in a gradient from neural to abneural side). Some of the cochlear duct pairs were obtained from batches of Wnt9a injections performed by Dr. Donna Fekete. We observe a widening of the prosensory domain in the Wnt9a injected ears (Figure A-6; defined by Serrate1) similar to our previous observations in E18 BPs (Munnamalai et al., 2017). As expected, if Wnt9a is acting via the canonical signaling pathway to promote proliferation, we observe an augmentation in the mitotic cell bodies in the Wnt9a injected ears compared to uninjected controls. However, beyond this effect, the β-catenin levels increase mildly if at all in 67% of cases (n=4/6). Only in 2 out of 6 pairs of BPs did we see a robust increase in PY489 β-catenin levels (Figure A-6, left panel), corroborating our hypothesis. A caveat is that there are brightly stained mitotic nuclei *en face*, with very strong PY489 β-catenin that might be obscuring the weaker β-catenin expression levels in the rest of the epithelium. Unfortunately, we were not able to correlate these results to levels of infection via histology due to unavailability of additional channels and had to rely on injection notes of the experimenter. Furthermore, as mentioned before, the role of Bcr-Abl kinase-mediated signaling was an unidentified factor in this experimental approach and could not be exculpated from the overall nuclear translocated β-catenin detected.

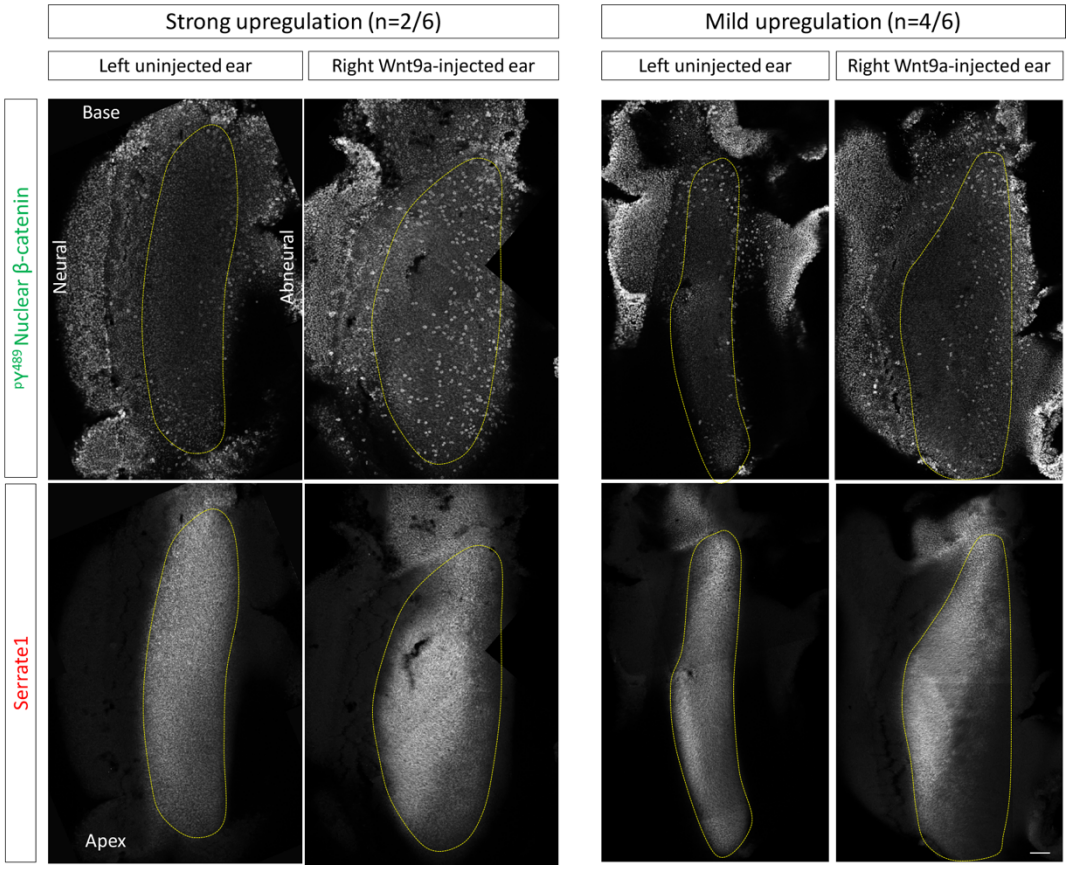

Figure A-6 Wnt9a overexpression moderately upregulates PY489 β-catenin levels.

E7 cochlear ducts were dissected and stained with the PY489-β-catenin antibody (Antibody B). The prosensory domain, outlined by a yellow dotted line, was defined by Serrate1 and axonal labelling (not shown here). The BPs were imaged *en face* by confocal microscopy using a 20X lens. The brightest spots seen in the PY489 β-catenin stains are M-phase cells that are found at the apical surface of the BP. In the Wnt9a-infected specimens, the BPs have more mitotic cells and are wider. Despite this obvious phenotype in all Wnt9a-injected BPs, only a subset shows a robust upregulation of β-catenin (left panel; n = 2/6). The overall increase in β-catenin is relatively weak in the remaining BPs (right panel; n = 4/6). Scale bar = 100μm.

A.3.3 Investigating anti-active-β-catenin levels downstream of Wnt9a

Considering the lack of a direct link between Wnt signaling pathway and Tyrosine-489 phosphorylation of β-catenin, we decided to employ another antibody designed to detect transcriptionally active β-catenin. Anti-active-β-catenin antibody (Figure A-3; Antibody A) binds to the un-phosphorylated Serine-37 and Threonine-41 epitope towards the N-terminal of β-catenin, which is phosphorylated by GSK-3β complex when Wnt ligand is absent (Nusse, 2012; van Noort et al., 2002). As with the previous antibody approach, the goal was to test for a neural-abneural gradient of active β-catenin, and upregulation of transcriptionally active β-catenin in Wnt9a infected embryos compared to the controls. We used E6 embryos for these experiments.

Though anti-active-β-catenin antibody could detect β-catenin in the middle of the cells in our immunostains (presumably transcriptionally active nuclear labelling), we found that it also detected the β-catenin bound to the adherens complex near the cell membrane, that accounted for the bulk of the signal (Figure A-3). We have yet to quantify expression levels of active β-catenin signal along the neural-abneural axis; however, upon staining the control E6 ears, an asymmetry in active-β-catenin was not visually apparent because of the overwhelming cell membrane staining compared to the nuclear signal. To examine changes in the active-β-catenin levels upon Wnt9a overexpression, we stained sections of E6 Wnt9a injected ears and compared the total active-β-catenin levels using a KS test on the intensity distributions (Figure A-7 shows an example). Some of the embryonic heads were obtained from batches of Wnt9a injections performed by Dr. Donna Fekete.

The summary figure (Figure A-8) shows KS test curves for all the animals analyzed at the 50% longitudinal position (additional percentiles along the longitudinal axis have not yet been analyzed). Among six Wnt9a-injected embryos, only three right (injected) BPs show a statistically significantly higher levels of β-catenin expression (22%, 52% and 54%) compared to the contralateral (uninjected) ears. Adjacent sections were stained with 3C2 antibody to detect RCAS virus and determine the level of infection for each animal (data not shown). No correlation between infection quality in the sensory epithelium and significance in KS test was observed. Some uninjected and parent virus controls show statistically significant differences in the average intensity between left and right ears, but the percentage changes are low (+/- 11% or smaller). Overall, no strong conclusions could be derived towards our hypotheses.

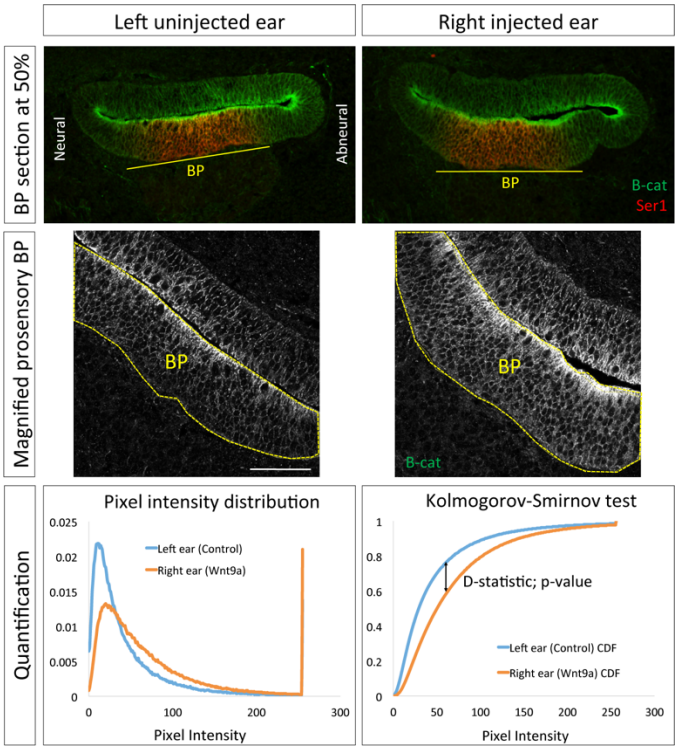

Figure A-7 Active β-catenin staining and quantification in Wnt9a-injected BPs at E6.

Wnt9a-injected, parent virus [RCAS(A)-injected and uninjected ears were sectioned and stained with anti-active β-catenin antibody (Antibody A). The prosensory domain was imaged at high magnification (60X lens) and a pixel distribution histogram was generated for the left and right prosensory BPs demarcated by Serrate1 or Sox2. Using a KS test, a cumulative difference function (D-statistic) was calculated which represents the maximum difference between the two histograms. This exemplar embryo is DMF323-32 in Figure A-8.

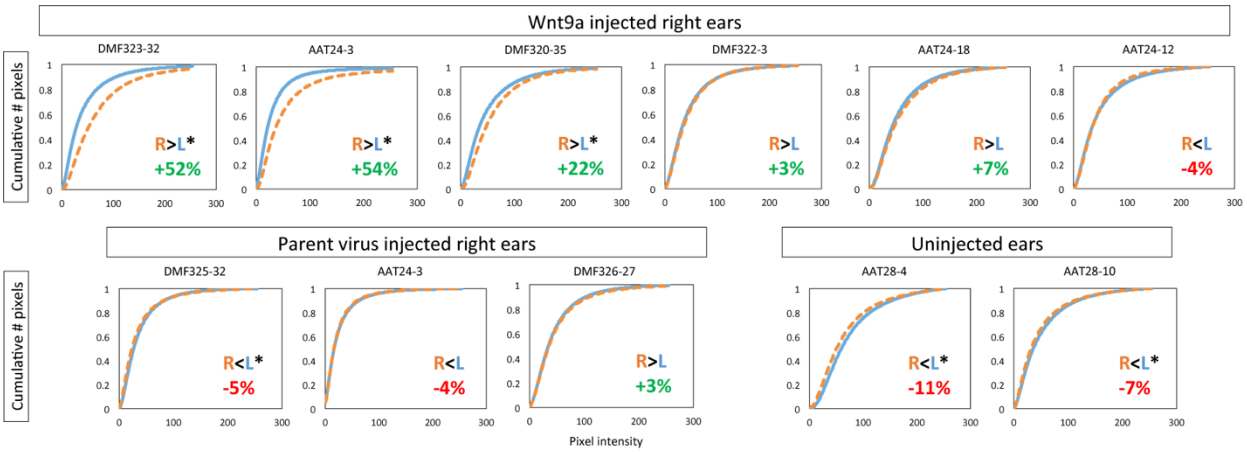

Figure A-8 Active β-catenin levels are higher in a subset of Wnt9a-injected BPs at E6.

KS curves of all the BPs analyzed are compiled. Left and Right ear of uninjected and parent virus injected animals are compared to set a baseline control. Change% in average β-catenin intensity is represented for each curve. Half (3/6) of the Wnt9a-injected ears show a significant increase in active β-catenin on the injected side that exceeds 20%, while the other half show relative differences between the sides that are comparable in magnitude to control ears (at or below +/-11%). In the plots, asterisks represent $p>0.05$ that right vs. left ears are not sampled from the same population (i.e., the null hypothesis is rejected).

A.3 Discussion

We used two different antibodies to seek direct evidence for canonical Wnt signaling facilitated by Wnt9a acting as a morphogen. At E6, we observed a negative gradient in nuclear-localized β-catenin in the expected direction across the radial axis of the BP using the PY489-β-catenin antibody (Antibody B), but not the active β-catenin antibody (Antibody A; data not shown). Because the phosphorylation of Y489 can be regulated by non-Wnt pathways, further studies are needed to understand the mechanism underlying this radial gradient.

With both antibodies, only a fraction (one-third to one-half) of the Wnt9a overexpression ears showed a robust increase in the levels of transcriptionally active β-catenin phosphoprotein. Wnt9a virus causes hyper-proliferation of the BP on E6 (Munnamalai et al., 2017), and this could be confirmed with the PY489-β-catenin antibody on E7, due to its inexplicably strong labeling of M-phase cells. Both β-catenin antibodies showed evidence of an increase in signal intensities 3-4 days after Wnt9a virus injection (E6 or E7), but not for every specimen tested. This biological variability was unrelated to the penetrance of an observable phenotype (a wider BP), which is nearly 100% upon Wnt9a overexpression (Munnamalai et al., 2017). Since the time of observation is 3 to 4 days after the injection of the virus carrying the transgene, we consider the possibility that the variability in response may reflect some negative feedback mechanism operating in this time window.

Inconsistencies in the changes in β-catenin levels may be due to the temporal levels of Wnt signaling upregulation or negative feedback when the tissue was harvested. Long RNA deep sequencing data comparing Wnt9a-injected E6 BPs with controls corroborates this interpretation of the data. Figure A-9 shows some known genes involved in the Wnt signaling pathway, including several negative regulators of Wnts, that are upregulated and some positive regulators that are downregulated by E6. This leads us to speculate that the inconsistent enhancement of β-catenin by Wnt9a may reflect a counteracting suppression of the canonical Wnt pathway via negative feedback. Interestingly, we also observed a non-canonical Wnt pathway (PCP gene; Celsr1) changing upon Wnt9a overexpression, that suggests maybe there is a switch between canonical Wnt/β-catenin pathway and non-canonical Wnt signaling ensuing at this stage. Future experiments could focus on markers more reliable (and perhaps less transient) than transcriptionally active β-catenin to reflect canonical activation of Wnt signaling mediated by Wnt9a.

Wnt target genes

Gene	Fold Change	Role in Wnt signaling
SP5	2.3	
WISP1	2.0	Negative regulator
WIF1	1.6	Negative regulator
Nkd1	1.4	Negative regulator
Gjb6	1.4	
Stra6	1.3	
Axin2	1.2	Negative regulator
sFrp2	0.8	Negative regulator
Isl1	0.7	
Dlk1	0.4	

Wnt signaling genes

Gene	Fold Change	Role in Wnt signaling
Znrf3	1.6	Negative regulator
Sox13	1.3	Negative regulator
Celsr1	1.2	PCP pathway
Rspo3	0.3	Positive regulator
Fzd10	0.4	Wnt receptor

Wnt9a	90.5

Upregulated
Downregulated

* All fold changes have p-adjusted-value <= 0.05

Figure A-9 Wnt9a overexpression changes known Wnt target genes and other genes related to Wnt signaling.

Using a deep sequencing approach to compare transcriptomes of Wnt9a-injected BPs with parent virus-injected (Control) BPs, we looked for differentially expressed genes (up or down) at E6. Fold change was calculated as Wnt9a/Control. Several negative regulators of Wnt signaling are upregulated, and two genes that promote Wnt signaling (Rspo3 and Fzd10) are downregulated. Note that one gene involved in the Wnt/planar cell polarity pathway, Celsr1, is also increased, suggesting activation of a non-canonical Wnt pathway. This analysis summary was prepared by Dr. Vidhya Munnamalai, Fekete lab (Munnamalai et al., 2017).

APPENDIX B. ASYMMETRIC RADIAL EXPRESSION OF MICRORNAS IN THE CHICKEN COCHLEA

We thank Dr. Shuai Chen for bioinformatics analysis of the small RNA sequencing data.

B.1 Involvement of microRNAs in cochlear development

As elaborated in Appendix A, Wnt9a ligand is significant in radial axis patterning of the chicken basilar papilla, the sensory domain of the avian cochlear duct. The mature basilar papilla comprises of tall hair cells and short hair cells, with each differentially innervated and serving different functions during auditory perception. Higher Wnt9a signaling instructs the superior, or tall hair cell fate, as demonstrated by a gain of function approach by the Fekete laboratory (Munnamalai et al., 2017). In this published study, we found several downstream signaling pathways and axon guidance molecules were detected to be differentially expressed upon Wnt9a overexpression. In conjunction with a long RNA sequencing project (part of the study published in Munnamalai et al., 2017), we attempted to identify the microRNAs that respond to Wnt9a signaling and can influence ensuing patterning cues.

MicroRNAs (miRNAs or miRs) are small non-coding RNA molecules, about 21 to 25 nucleotides in length, that regulate expression of genes post-transcriptionally, primarily by binding to the 3'-untranslated regions (UTR) of the target genes. MiRNAs are often coded in intron regions of genes, and are transcribed into pri-miRNAs, processed by Drosha enzymes into pre-miRNA, exported out of the nucleus, and processed further by Dicer complex. When the processed miRNA is attached to an RNA-induced silencing complex (RISC), it can bind to the target transcripts (He and Hannon, 2004; Winter et al., 2009). As well described in several contexts, miRNAs are recognized to be important in development and as prospective regulators or fine-tuners of morphogen gradients establishing threshold responses and sharpening patterning genes post-transcriptionally (He and Hannon, 2004; Inui et al., 2012; Parchem et al., 2014). For example, miR135a is important to regulate Wnt and possibly TGFß/BMP pathways during forebrain development (Caronia-Brown et al., 2016); miR9 is important for the maintenance of the midbrain-hindbrain boundary signaling center and its associated FGF signaling pathway (Leucht et al., 2008). Most miRNAs with multi-fold overexpression can downregulate the target expression by not more than 50%, however even slight modulation of morphogen levels can result in varied or

uncharacteristic downstream fate patterning (Inui et al., 2012). This makes miRNAs suitable "rheostats" to control morphogen-driven signaling.

Our goal was to explore such fine-tuned fate patterning mechanisms in cochlear patterning, and **small RNA sequencing (as well as long RNA) was performed by Fekete laboratory to determine miRNAs expressed in developing sensory cochlea, particularly those important for radial axis patterning of the basilar papilla (BP)**. The differentially-expressed miRNAs across the experimental groups: control and Wnt9a-overexpression, would be possible candidates involved downstream of Wnt9a to alter hair cell fates. From the small RNA sequencing data, miRNA candidates were shortlisted based on expression levels, fold changes across the two aforementioned experimental conditions, and our interest for these candidates based on the knowledge of the miRNA response elements (MREs) containing target genes.

B.2 Identifying microRNAs involved in radial axis patterning of the chicken cochlea

E3 otic vesicles were injected with avian retrovirus (RCAS) with or without the Wnt9a transgene; the two experimental conditions were RCAS parent virus injection (control), and RCAS-Wnt9a injection (Wnt9a). The cochlear ducts were micro-dissected out of live E6 embryos; all care was taken to remove the vestibular organs, lagena and as much of the auditory ganglion as possible. Six batches of samples (3 Wnt9a-injected and 3 controls) were prepared as a combined effort with Donna Fekete (advisor) and M. Katie Scott (graduate student). Total RNA was extracted using Qiagen miRNeasy® kit for deep sequencing. For each sample, 24 BPs were pooled from one batch of injections. The samples were sent to the Purdue sequencing facility to construct RNA libraries (Figure B-1). Briefly, the purified RNA samples were tagged with proprietary sequences and converted into cDNA via reverse transcriptase and amplified. The output was compared to the *Gallus gallus* genome bank (NCBI and Ensembl) to identify the RNA reads. For miRNAs, our collaborator Dr. Shuai Chen (former Purdue graduate student) used the Harvard database for mature miRNA sequences to compare the read sequences and further bioinformatics analysis. The deep sequencing data gave us around 300 significantly expressed miRNA candidates (cutoff = 10 reads). Fold change of 1.5 or more was considered significant. 6 out of 300 miRNAs were significantly differentially expressed across the experimental conditions by a fold change of 1.5 or more and some additional miRNA candidates with high expression levels but not statistically significant fold changes are listed in Table B-1 as candidates for further analysis (in situ hybridization).

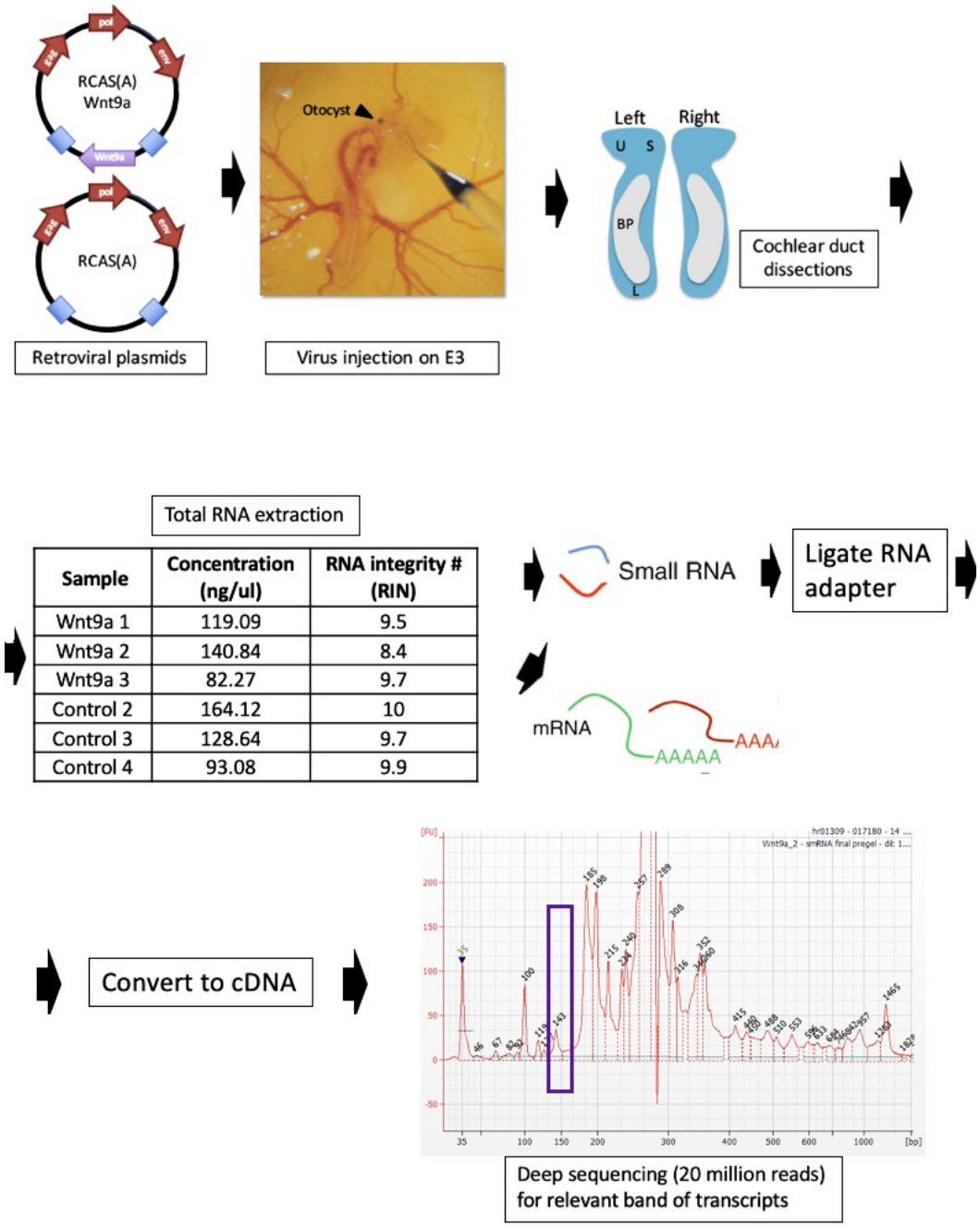

Figure B-1 Flowchart of small RNA sequencing of Wnt9a-overexpressed cochlea.

Following the arrowheads from top to bottom, E3 chicken embryos were injected with RCAS (control empty vector) or RCAS-Wnt9a into the otocyst. Cochlear ducts were dissected at E6 and RNA was extracted from samples, with each sample consisting of 24 cochleae each. Samples were split for long and small RNA sequencing. For small RNA sequencing, adapters of known length were ligated to the RNA transcripts, the entire sample converted to cDNA, and the band of interest was isolated (miRs + adapter length; purple box).

Table B-1 List of differentially expressed microRNAs

microRNA	Average reads	Fold Change	P-value
gga-miR-10a-5p	1,371.6	2.49	0.0001
gga-miR-1563	35.1	2.10	0.0092
gga-miR-206/miR-1-3p	93.4	1.93	0.0126
gga-miR-489-3p	188.8	1.61	0.0179
gga-miR-1662	5,836.9	1.52	0.0291
gga-miR-490-5p	197.3	1.50	0.0419
gga-miR-19a-3p	299.7	3.20	0.1677
gga-miR-19b-3p	1,028.8	3.16	0.1952
gga-miR-10b-5p	1,015.3	2.15	0.0565
gga-miR-146c-3p	2,439.8	1.33	0.0727
gga-miR-100-5p	218,955.1	1.42	0.0758
gga-miR-221-5p	377.3	2.37	0.0768
gga-miR-130a-5p	3,740.6	1.50	0.0963
gga-miR-18b-3p	549.9	1.73	0.0980

Green miRNAs are upregulated upon Wnt9a overexpression. Red are downregulated. Grey highlighted miRNAs are not statistically significantly ($p>0.05$) different but are added to the list based on high copy number or high fold change.

B.3 Discussion and Future directions

Several miRNAs have been identified and examined for their function in the inner ear development, maturation and regeneration (Elkan-Miller et al., 2011; Frucht et al., 2011; Hertzano et al., 2011; Zhang et al., 2015). For example, miR-96 family is important for hair cell maturation in the cochlea (Zhang et al., 2015); miR181a is important for adult basilar papilla regeneration post injury (Frucht et al., 2011). This project aimed at identifying miRNAs important for radial axis patterning and cell fate specification of chicken basilar papilla.

We chose to investigate the cochlear duct a day later than when the Wnt9a asymmetric expression is first observed (Sienknecht and Fekete, 2009); by E6 we could expect to observe the early signs of Wnt9a-mediated asymmetric signaling in the prosensory domain. After finding possibly significant miRNA candidates via small RNA sequencing and validating their expression *in vivo*, future studies from the lab could be conducted to focus on miRNA-target gene interactions by matching the candidate miRNAs with relevant differentially expressed long RNAs obtained via deep sequencing from the same samples (PhD dissertation project of M. Katie Scott, graduate student from Fekete lab).

While collecting the cochlear ducts for RNA extraction, part of the auditory ganglion (unwantedly so) and the non-sensory region of the cochlear duct were collected along with the prosensory domain. Adam Lorch, a research technician in the Fekete lab, attempted to detect the shortlisted miRNAs (Table B-1) via in situ hybridization to check for expression in the inner ears of normal or Wnt9a-overexpression embryos. Digoxygenin double-labeled locked nucleic acid (LNA^{TM}) probes were custom-designed and purchased from Exiqon (http://www.exiqon.com) by and several miRNAs were detected at E6, 7, 8, 9, and 10: miR 10a-5p, 100-5p, 206, 221-5p, 1662, 6599, 199a-5p, 140-3p, and 140-5p (experiments done by Adam Lorch). MiR-96 (previously used and established protocol from Zhang et al., 2015) was successfully used as a positive control. Though the positive control worked as expected, with positive signal in the hair cell layer of the vestibular organs, the miRNAs of interest for radial axis patterning were not reliably and robustly detected, perhaps due to low number of transcripts. For future experiments, the lab is working towards improvising the miRNA in situ hybridization protocol.

As a future direction, any candidate miRNA validated by in situ hybridization as having an interesting expression pattern in the E6 cochlear duct, could be further analyzed. A more extensive spatial and temporal expression pattern could be explored. TargetScan.org, miRBase.org, PicTar, miRanda and other similar programs can be used to determine the miRNA-target gene interaction

to find candidate interactions for further evaluation. Ingenuity Pathway Analysis (IPA) can be used to match the differentially expressed small RNAs and long RNAs to identify possible gene regulatory networks. IPA can find feed-forward or feedback gene interaction loops involving these miRNAs for further study by comparing the predicted targets of the shortlisted miRNAs with the long RNA differential expression data, and subsequent validated by in situ hybridization.

Using the TargetScan database, preliminary search results for transcripts with miRNA response elements for our shortlisted miRNAs (Table B-1) identified certain genes that were also differentially expressed in the long RNA sequencing data; several genes are predicted targets for one or more miRNA from our list (Table B-2). In addition to miR-10 predicted to target Wnt9a itself, several of these are known to be expressed in the developing inner ear. For example, Prox1 is expressed in the supporting cells of the abneural compartment in the murine cochlea (Jacques et al., 2012). Immunostaining of whole mount E6 BPs shows an abneural expression of Prox1 primarily in the apical half of the BP (unpublished observations from Fekete lab). Our deep sequencing results show that Wnt9a overexpression leads to downregulation of Prox1 by ~30% and more than one miRNA from our shortlist is predicted to target Prox1 (TargetScan.org; Figure B-2). We have yet to test changes in Prox1 expression in Wnt9a-injected ears via immunohistochemistry.

Misexpression of these miRNAs of interest can shed further light on these miR-target gene interactions. The significance of this study is that our results can add to the understanding of the molecular mechanisms controlling the morphogen-driven fate specification of two main hair cell types of the avian cochlea. The molecular mechanisms can be projected to the mammalian phenotype because of highly conserved basic principles of development across the phylogenetic tree.

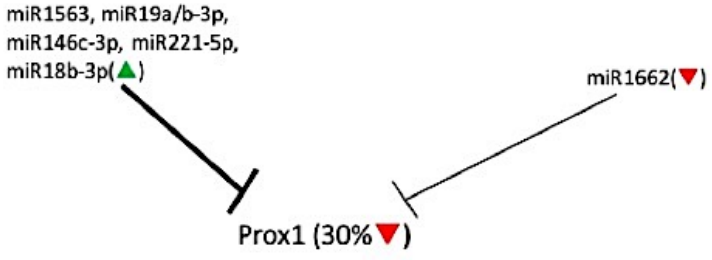

Figure B-2 Example of microRNA-target gene interaction.

Prox1 (an abneural ear marker) is downregulated (red arrow) in our deep sequencing dataset and some miRNAs predicted to target Prox1 are significantly upregulated (green arrow).

Table B-2 Prospective target genes with MREs for shortlisted microRNAs

microRNA	Target genes (TargetScan) also differentially expressed in Wnt9a long RNA sequencing database
gga-miR-10-5p	WNT9A, SLC24A4, MDGA2, PPFIA2, CHL1, ST6GALNAC3, PAK3, TNC, PYGO1, RHOU, FOXP2, NPAS3, SETBP1, TFRC, SLIT2, DLG5, KIAA1462, LTBP1, ATP8A2, BDNF,
gga-miR-1563	PDE8B, SLC24A2, TSHZ3, DENND5B, KLF7, ZBTB20, HAPLN1, GULP1, HUNK, CTGF, ADAMTSL1, MLLT3, SIK1, ZFHX4, SYNJ1, RAPH1, RHOU, FOXP2, SLC4A4, PDGFRA, C1orf198, COL9A1, COL5A1, KIF21A, ZBTB1, BRWD1, STAM, DLG5, YES1, ITSN1, SALL3, GPRC5B, FANCA, PROX1, HDAC9, BDNF, ERBB4, SORCS3, CDH8, ALPK2,
gga-miR-206	SLC5A3, ZPLD1, PDE8B, PPFIA2, ALCAM, GALNTL6, ANO3, KLF7, HAPLN1, PAK3, UST, RHOJ, KAL1, SESN3, MLLT3, ZFHX4, ARHGEF3, MYLK, SYNJ1, DSE, SNAI2, ASAP1, NPAS3, ARID5B, KALRN, WNK1, ANKRD50, BRWD1, YES1, KIAA1462, THBS1, RPL35A, ITGA6, KCNK2, ANXA5, TOX, SALL1, RORB, BDNF, STC2, NSUN7, FZD10, KCNJ15, RSPO3,
gga-miR489-3p	MKX, LZTS1, CHL1, ARL4A, ZBTB20, TDRP, ST6GALNAC3, PAK3, VCL, GULP1, SESN3, CTNNAL1, ZFHX4, CACNA1H, BMP7, SLCO5A1, NPAS3, ARID5B, PALLD, KIAA1217, ZFHX3, DACT1, EML1, ANKRD50, DLG5, BASP1, HSPA12A, SALL3, NELL2, ATP8A2, SFRP2, GREB1L, ELMOD1, RORB, BEGAIN, SHISA2, BDNF, ERBB4, NRXN3, ITGA8,
gga-miR-490-5p	ZPLD1, ALCAM, LZTS1, FZD4, ZNRF3, ATP11A, TENM1, ZBTB20, TDRP, ST6GALNAC3, ADCY5, HUNK, CYP1B1, ADAMTSL1, MLLT3, ARHGAP42, RHOU, FOXP2, PPL, SLCO5A1, PDLIM5, CCDC80, ZBTB1, MAPK6, ATP8A2, KCNK2, CNTN3, ISL1, BDNF, ERBB4, ITGA8, MYPN,
gga-miR1662	PPFIA2, ALCAM, CHL1, NXPH1, SLITRK6, PTPRT, TENM1, ZBTB20, STX18, SESN3, SIK1, ARHGEF3, ZNF469, PDGFRA, SLCO5A1, NPAS3, ARID5B, COL1A2, KIAA1217, AHR, WNK1, PHACTR2, EML1, EP300, ANKRD50, BRWD1, DLG5, HSPA12A, THBS1, RPS12, ATP8A2, PROX1, BDNF, ERBB4, ACTC1,
gga-miR-19-3p	SLC24A4, PRRX1, ZPLD1, PPFIA2, TSHZ3, ZNRF3, ANO3, SMOC1, ATP11A, KLF7, KIAA1211, TENM1, ARL4A, ZBTB20, GRHL1, GULP1, CTGF, E2F8, ARHGEF3, MPPED2, PTPRU, ASAP1, RAPH1, FOXP2, PPL, NPAS3, ARID5B, COL1A2, PALLD, CELSR1, KALRN, PHACTR2, EML1, BRWD1, STAM, DLG5, YES1, ITSN1, KIAA1462, THBS1, MAPK6, MSRB3, WNT7B, ITGA6, ATP2B2, PROX1, NRP2, C4orf19, HDAC9, ERBB4, HES5, ITGB6, NTN4,
gga-miR-146c-3p	VGLL2, MDGA2, PDE8B, PDZRN4, ZNRF3, LRRFIP2, SMOC1, ZBTB20, SMAD6, E2F8, SESN3, MLLT3, NPNT, RFTN2, RAPH1, LRP8, PALLD, KALRN, ITPR3, CCDC80, EML1, STAM, YES1, ITSN1, OTX2, LTBP1, TLL2, ITGA6, ATP2B2, PROX1, SOX2, HDAC9, ERBB4, NRXN3, ITGA8, STC2, RSPO3,
gga-miR-100-5p	GALNTL6, CACNA1H,
gga-miR-221-5p	HCN4, MDGA2, TSHZ3, TENM1, ZBTB20, HUNK, RHOU, PPL, NPAS3, SETBP1, WNK1, SEPP1, TJP2, ATP9B, ITGA6, PROX1, NRXN3, NSUN7,
gga-miR-130a-5p	MSX2, SLC24A4, HS3ST1, DLX5, TNR, PRRX1, TBX3, PTPRT, ABLIM1, LTBP2, ARL4A, ZBTB20, GJB6, KIAA1551, VCL, RHOJ, MLLT3, ZFHX4, PLS3, NPNT, APCDD1, INPP4B, FOXP2, PPL, PDGFRA, NPAS3, ARID5B, KIAA1217, ZFHX3, NCALD, EP300, ANKRD50, DLG5, YES1, TJP2, SALL3, MGAT3, GPRC5B, KHDRBS3, TOX, HDAC9, BEGAIN, BDNF, NRXN3, STC2, FZD10, NTN4,
gga-miR-18b-3p	PPFIA2, ALCAM, KLF7, TENM1, ZBTB20, HAPLN1, CDK6, SESN3, MYLK, ASAP1, LRP8, WNK1, ITPR3, TFRC, PHACTR2, RPS20, HEY1, MGAT3, OTX2, PCSK1, TLL2, PROX1, ITGA8,

All miRNAs listed above except for the grey highlighted miRNAs are statistically significantly ($p<0.05$) different.

REFERENCES

Adams Waldorf, K.M., Nelson, B.R., Stencel-Baerenwald, J.E., Studholme, C., Kapur, R.P., Armistead, B., Walker, C.L., Merillat, S., Vornhagen, J., Tisoncik-Go, J.*, et al.* (2018). Congenital Zika virus infection as a silent pathology with loss of neurogenic output in the fetal brain. Nat Med *24*, 368-374.

Adams Waldorf, K.M., Stencel-Baerenwald, J.E., Kapur, R.P., Studholme, C., Boldenow, E., Vornhagen, J., Baldessari, A., Dighe, M.K., Thiel, J., Merillat, S.*, et al.* (2016). Fetal brain lesions after subcutaneous inoculation of Zika virus in a pregnant nonhuman primate. Nat Med *22*, 1256-1259.

Aliota, M.T., Dudley, D.M., Newman, C.M., Mohr, E.L., Gellerup, D.D., Breitbach, M.E., Buechler, C.R., Rasheed, M.N., Mohns, M.S., Weiler, A.M.*, et al.* (2016). Heterologous Protection against Asian Zika Virus Challenge in Rhesus Macaques. PLoS Negl Trop Dis *10*, e0005168.

Anfasa, F., Siegers, J.Y., van der Kroeg, M., Mumtaz, N., Stalin Raj, V., de Vrij, F.M.S., Widagdo, W., Gabriel, G., Salinas, S., Simonin, Y.*, et al.* (2017). Phenotypic Differences between Asian and African Lineage Zika Viruses in Human Neural Progenitor Cells. mSphere *2*.

Ashwal, S., Michelson, D., Plawner, L., Dobyns, W.B., Quality Standards Subcommittee of the American Academy of, N., and the Practice Committee of the Child Neurology, S. (2009). Practice parameter: Evaluation of the child with microcephaly (an evidence-based review). Neurology *73*, 887-897.

Barbi, L., Coelho, A.V.C., Alencar, L.C.A., and Crovella, S. (2018). Prevalence of Guillain-Barre syndrome among Zika virus infected cases: a systematic review and meta-analysis. Braz J Infect Dis *22*, 137-141.

Bayless, N.L., Greenberg, R.S., Swigut, T., Wysocka, J., and Blish, C.A. (2016). Zika Virus Infection Induces Cranial Neural Crest Cells to Produce Cytokines at Levels Detrimental for Neurogenesis. Cell Host Microbe *20*, 423-428.

Besnard, M., Eyrolle-Guignot, D., Guillemette-Artur, P., Lastere, S., Bost-Bezeaud, F., Marcelis, L., Abadie, V., Garel, C., Moutard, M.L., Jouannic, J.M.*, et al.* (2016). Congenital cerebral malformations and dysfunction in fetuses and newborns following the 2013 to 2014 Zika virus epidemic in French Polynesia. Euro Surveill *21*.

Bissonnette, J.P., and Fekete, D.M. (1996). Standard atlas of the gross anatomy of the developing inner ear of the chicken. J Comp Neurol *368*, 620-630.

Bok, J., Raft, S., Kong, K.A., Koo, S.K., Drager, U.C., and Wu, D.K. (2011). Transient retinoic acid signaling confers anterior-posterior polarity to the inner ear. Proc Natl Acad Sci U S A *108*, 161-166.

Bollati, M., Alvarez, K., Assenberg, R., Baronti, C., Canard, B., Cook, S., Coutard, B., Decroly, E., de Lamballerie, X., Gould, E.A.*, et al.* (2010). Structure and functionality in flavivirus NS-proteins: perspectives for drug design. Antiviral Res *87*, 125-148.

Bronner-Fraser, M. (1996). Methods in avian embryology (San Diego: Academic Press).

Butler, H., and Juurlink, B.H.J. (1987). An atlas for staging mammalian and chick embryos (Boca Raton, Fla.: CRC Press).

Caine, E.A., Jagger, B.W., and Diamond, M.S. (2018). Animal Models of Zika Virus Infection during Pregnancy. Viruses *10*.

Caires-Junior, L.C., Goulart, E., Melo, U.S., Araujo, B.H.S., Alvizi, L., Soares-Schanoski, A., de Oliveira, D.F., Kobayashi, G.S., Griesi-Oliveira, K., Musso, C.M.*, et al.* (2018). Discordant congenital Zika syndrome twins show differential in vitro viral susceptibility of neural progenitor cells. Nat Commun *9*, 475.

Caronia-Brown, G., Anderegg, A., and Awatramani, R. (2016). Expression and functional analysis of the Wnt/beta-catenin induced mir-135a-2 locus in embryonic forebrain development. Neural Dev *11*, 9.

Cavodeassi, F., and Houart, C. (2012). Brain regionalization: of signaling centers and boundaries. Dev Neurobiol *72*, 218-233.

Centers for Disease Control and Prevention (CDC). (2018). Zika Cases in the United States, 2015-2018. Available at: https://www.cdc.gov/zika/reporting/case-counts.html

Coelho, A.V.C., and Crovella, S. (2017). Microcephaly Prevalence in Infants Born to Zika Virus-Infected Women: A Systematic Review and Meta-Analysis. Int J Mol Sci *18*.

Cohen, B.E., Durstenfeld, A., and Roehm, P.C. (2014). Viral causes of hearing loss: a review for hearing health professionals. Trends Hear *18*.

Cugola, F.R., Fernandes, I.R., Russo, F.B., Freitas, B.C., Dias, J.L., Guimaraes, K.P., Benazzato, C., Almeida, N., Pignatari, G.C., Romero, S.*, et al.* (2016). The Brazilian Zika virus strain causes birth defects in experimental models. Nature *534*, 267-271.

D'Amico-Martel, A., and Noden, D.M. (1983). Contributions of placodal and neural crest cells to avian cranial peripheral ganglia. Am J Anat *166*, 445-468.

Dai, L., Song, J., Lu, X., Deng, Y.Q., Musyoki, A.M., Cheng, H., Zhang, Y., Yuan, Y., Song, H., Haywood, J.*, et al.* (2016). Structures of the Zika Virus Envelope Protein and Its Complex with a Flavivirus Broadly Protective Antibody. Cell Host Microbe *19*, 696-704.

Dallos, P., Popper, A.N., and Fay, R.R. (1996). The cochlea (New York: Springer).

Darnell, D.K., Kaur, S., Stanislaw, S., Davey, S., Konieczka, J.H., Yatskievych, T.A., and Antin, P.B. (2007). GEISHA: an in situ hybridization gene expression resource for the chicken embryo. Cytogenet Genome Res *117*, 30-35.

Davey, M.G., and Tickle, C. (2007). The chicken as a model for embryonic development. Cytogenet Genome Res *117*, 231-239.

de Fatima Vasco Aragao, M., van der Linden, V., Brainer-Lima, A.M., Coeli, R.R., Rocha, M.A., Sobral da Silva, P., Durce Costa Gomes de Carvalho, M., van der Linden, A., Cesario de Holanda, A., and Valenca, M.M. (2016). Clinical features and neuroimaging (CT and MRI) findings in presumed Zika virus related congenital infection and microcephaly: retrospective case series study. BMJ *353*, i1901.

de Paula Freitas, B., de Oliveira Dias, J.R., Prazeres, J., Sacramento, G.A., Ko, A.I., Maia, M., and Belfort, R., Jr. (2016). Ocular Findings in Infants With Microcephaly Associated With Presumed Zika Virus Congenital Infection in Salvador, Brazil. JAMA Ophthalmol.

Dick, G.W. (1952). Zika virus. II. Pathogenicity and physical properties. Trans R Soc Trop Med Hyg *46*, 521-534.

Dick, G.W., Kitchen, S.F., and Haddow, A.J. (1952). Zika virus. I. Isolations and serological specificity. Trans R Soc Trop Med Hyg *46*, 509-520.

do Rosario, M.S., de Jesus, P.A., Vasilakis, N., Farias, D.S., Novaes, M.A., Rodrigues, S.G., Martins, L.C., Vasconcelos, P.F., Ko, A.I., Alcantara, L.C.*, et al.* (2016). Guillain-Barre Syndrome After Zika Virus Infection in Brazil. Am J Trop Med Hyg *95*, 1157-1160.

Doss, C.G., Siva, R., Christopher, B.P., Chakraborty, C., and Zhu, H. (2017). Zika: How safe is India? Infect Dis Poverty *6*, 37.

Dowall, S.D., Graham, V.A., Rayner, E., Atkinson, B., Hall, G., Watson, R.J., Bosworth, A., Bonney, L.C., Kitchen, S., and Hewson, R. (2016). A Susceptible Mouse Model for Zika Virus Infection. PLoS Negl Trop Dis *10*, e0004658.

Driggers, R.W., Ho, C.Y., Korhonen, E.M., Kuivanen, S., Jaaskelainen, A.J., Smura, T., Rosenberg, A., Hill, D.A., DeBiasi, R.L., Vezina, G.*, et al.* (2016). Zika Virus Infection with Prolonged Maternal Viremia and Fetal Brain Abnormalities. N Engl J Med *374*, 2142-2151.

Dudley, D.M., Aliota, M.T., Mohr, E.L., Weiler, A.M., Lehrer-Brey, G., Weisgrau, K.L., Mohns, M.S., Breitbach, M.E., Rasheed, M.N., Newman, C.M.*, et al.* (2016). A rhesus macaque model of Asian-lineage Zika virus infection. Nat Commun *7*, 12204.

Echevarria, D., Vieira, C., Gimeno, L., and Martinez, S. (2003). Neuroepithelial secondary organizers and cell fate specification in the developing brain. Brain Res Brain Res Rev *43*, 179-191.

Elkan-Miller, T., Ulitsky, I., Hertzano, R., Rudnicki, A., Dror, A.A., Lenz, D.R., Elkon, R., Irmler, M., Beckers, J., Shamir, R.*, et al.* (2011). Integration of transcriptomics, proteomics, and microRNA analyses reveals novel microRNA regulation of targets in the mammalian inner ear. PLoS One *6*, e18195.

Ellis, P., Fagan, B.M., Magness, S.T., Hutton, S., Taranova, O., Hayashi, S., McMahon, A., Rao, M., and Pevny, L. (2004). SOX2, a persistent marker for multipotential neural stem cells derived from embryonic stem cells, the embryo or the adult. Dev Neurosci *26*, 148-165.

Evsen, L., Sugahara, S., Uchikawa, M., Kondoh, H., and Wu, D.K. (2013). Progression of neurogenesis in the inner ear requires inhibition of Sox2 transcription by neurogenin1 and neurod1. J Neurosci *33*, 3879-3890.

Fair, J.M., Nemeth, N.M., Taylor-McCabe, K.J., Shou, Y., and Marrone, B.L. (2011). Clinical and acquired immunologic responses to West Nile virus infection of domestic chickens (Gallus gallus domesticus). Poult Sci *90*, 328-336.

Fandino-Cardenas, M., Idrovo, A.J., Velandia, R., Molina-Franky, J., and Alvarado-Socarras, J.L. (2018). Zika Virus Infection during Pregnancy and Sensorineural Hearing Loss among Children at 3 and 24 Months Post-Partum. J Trop Pediatr.

Fekete, D.M., Homburger, S.A., Waring, M.T., Riedl, A.E., and Garcia, L.F. (1997). Involvement of programmed cell death in morphogenesis of the vertebrate inner ear. Development *124*, 2451-2461.

Fekete, D.M., and Wu, D.K. (2002). Revisiting cell fate specification in the inner ear. Curr Opin Neurobiol *12*, 35-42.

Ferran, J.L., Sanchez-Arrones, L., Bardet, S.M., Sandoval, J.E., Martinez-de-la-Torre, M., and Puelles, L. (2008). Early pretectal gene expression pattern shows a conserved anteroposterior tripartition in mouse and chicken. Brain Res Bull *75*, 295-298.

Fettiplace, R., and Kim, K.X. (2014). The physiology of mechanoelectrical transduction channels in hearing. Physiol Rev *94*, 951-986.

Fischer, F.P. (1992). Quantitative analysis of the innervation of the chicken basilar papilla. Hear Res *61*, 167-178.

Foy, B.D., Kobylinski, K.C., Chilson Foy, J.L., Blitvich, B.J., Travassos da Rosa, A., Haddow, A.D., Lanciotti, R.S., and Tesh, R.B. (2011). Probable non-vector-borne transmission of Zika virus, Colorado, USA. Emerg Infect Dis *17*, 880-882.

Frieden, T.R., Schuchat, A., and Petersen, L.R. (2016). Zika Virus 6 Months Later. JAMA *316*, 1443-1444.

Fritzsch, B., Beisel, K.W., and Hansen, L.A. (2006). The molecular basis of neurosensory cell formation in ear development: a blueprint for hair cell and sensory neuron regeneration? Bioessays *28*, 1181-1193.

Frucht, C.S., Santos-Sacchi, J., and Navaratnam, D.S. (2011). MicroRNA181a plays a key role in hair cell regeneration in the avian auditory epithelium. Neurosci Lett *493*, 44-48.

Galli, L.M., Munji, R.N., Chapman, S.C., Easton, A., Li, L., Onguka, O., Ramahi, J.S., Suriben, R., Szabo, L.A., Teng, C.*, et al.* (2014). Frizzled10 mediates WNT1 and WNT3A signaling in the dorsal spinal cord of the developing chick embryo. Dev Dyn *243*, 833-843.

Garcez, P.P., Loiola, E.C., Madeiro da Costa, R., Higa, L.M., Trindade, P., Delvecchio, R., Nascimento, J.M., Brindeiro, R., Tanuri, A., and Rehen, S.K. (2016). Zika virus impairs growth in human neurospheres and brain organoids. Science *352*, 816-818.

Garcia-Lopez, R., Pombero, A., and Martinez, S. (2009). Fate map of the chick embryo neural tube. Dev Growth Differ *51*, 145-165.

Gatherer, D., and Kohl, A. (2016). Zika virus: a previously slow pandemic spreads rapidly through the Americas. J Gen Virol *97*, 269-273.

Ginhoux, F., Lim, S., Hoeffel, G., Low, D., and Huber, T. (2013). Origin and differentiation of microglia. Front Cell Neurosci *7*, 45.

Goodfellow, F.T., Tesla, B., Simchick, G., Zhao, Q., Hodge, T., Brindley, M.A., and Stice, S.L. (2016). Zika Virus Induced Mortality and Microcephaly in Chicken Embryos. Stem Cells Dev *25*, 1691-1697.

Goodyear, R.J., Legan, P.K., Christiansen, J.R., Xia, B., Korchagina, J., Gale, J.E., Warchol, M.E., Corwin, J.T., and Richardson, G.P. (2010). Identification of the hair cell soma-1 antigen, HCS-1, as otoferlin. J Assoc Res Otolaryngol *11*, 573-586.

Gorman, M.J., Caine, E.A., Zaitsev, K., Begley, M.C., Weger-Lucarelli, J., Uccellini, M.B., Tripathi, S., Morrison, J., Yount, B.L., Dinnon, K.H., 3rd*, et al.* (2018). An Immunocompetent Mouse Model of Zika Virus Infection. Cell Host Microbe *23*, 672-685 e676.

Group, M.E.R. (2016). Microcephaly in Infants, Pernambuco State, Brazil, 2015. Emerg Infect Dis *22*, 1090-1093.

Groves, A.K., and Fekete, D.M. (2012). Shaping sound in space: the regulation of inner ear patterning. Development *139*, 245-257.

Guillemette-Artur, P., Besnard, M., Eyrolle-Guignot, D., Jouannic, J.M., and Garel, C. (2016). Prenatal brain MRI of fetuses with Zika virus infection. Pediatr Radiol *46*, 1032-1039.

Gulland, A. (2016). Zika virus is a global public health emergency, declares WHO. BMJ *352*, i657.

Gyawali, N., Bradbury, R.S., and Taylor-Robinson, A.W. (2016). The global spread of Zika virus: is public and media concern justified in regions currently unaffected? Infect Dis Poverty *5*, 37.

Hamburger, V., and Hamilton, H.L. (1992). A series of normal stages in the development of the chick embryo. 1951. Dev Dyn *195*, 231-272.

Hamel, R., Dejarnac, O., Wichit, S., Ekchariyawat, P., Neyret, A., Luplertlop, N., Perera-Lecoin, M., Surasombatpattana, P., Talignani, L., Thomas, F.*, et al.* (2015). Biology of Zika Virus Infection in Human Skin Cells. J Virol *89*, 8880-8896.

Hasan, S.S., Miller, A., Sapparapu, G., Fernandez, E., Klose, T., Long, F., Fokine, A., Porta, J.C., Jiang, W., Diamond, M.S.*, et al.* (2017). A human antibody against Zika virus crosslinks the E protein to prevent infection. Nat Commun *8*, 14722.

Hastings, A.K., Yockey, L.J., Jagger, B.W., Hwang, J., Uraki, R., Gaitsch, H.F., Parnell, L.A., Cao, B., Mysorekar, I.U., Rothlin, C.V.*, et al.* (2017). TAM Receptors Are Not Required for Zika Virus Infection in Mice. Cell Rep *19*, 558-568.

Hayhurst, M., Gore, B.B., Tessier-Lavigne, M., and McConnell, S.K. (2008). Ongoing sonic hedgehog signaling is required for dorsal midline formation in the developing forebrain. Dev Neurobiol *68*, 83-100.

He, L., and Hannon, G.J. (2004). MicroRNAs: small RNAs with a big role in gene regulation. Nat Rev Genet *5*, 522-531.

Hertzano, R., Elkon, R., Kurima, K., Morrisson, A., Chan, S.L., Sallin, M., Biedlingmaier, A., Darling, D.S., Griffith, A.J., Eisenman, D.J.*, et al.* (2011). Cell type-specific transcriptome analysis reveals a major role for Zeb1 and miR-200b in mouse inner ear morphogenesis. PLoS Genet *7*, e1002309.

Hills, S.L., Russell, K., Hennessey, M., Williams, C., Oster, A.M., Fischer, M., and Mead, P. (2016). Transmission of Zika Virus Through Sexual Contact with Travelers to Areas of Ongoing Transmission - Continental United States, 2016. MMWR Morb Mortal Wkly Rep *65*, 215-216.

Hirokawa, N. (1978). The ultrastructure of the basilar papilla of the chick. J Comp Neurol *181*, 361-374.

Hirsch, A.J., Smith, J.L., Haese, N.N., Broeckel, R.M., Parkins, C.J., Kreklywich, C., DeFilippis, V.R., Denton, M., Smith, P.P., Messer, W.B.*, et al.* (2017). Zika Virus infection of rhesus macaques leads to viral persistence in multiple tissues. PLoS Pathog *13*, e1006219.

Huang, W.C., Abraham, R., Shim, B.S., Choe, H., and Page, D.T. (2016). Zika virus infection during the period of maximal brain growth causes microcephaly and corticospinal neuron apoptosis in wild type mice. Sci Rep *6*, 34793.

Inui, M., Montagner, M., and Piccolo, S. (2012). miRNAs and morphogen gradients. Curr Opin Cell Biol *24*, 194-201.

Jacques, B.E., Montgomery, W.H.t., Uribe, P.M., Yatteau, A., Asuncion, J.D., Resendiz, G., Matsui, J.I., and Dabdoub, A. (2014). The role of Wnt/beta-catenin signaling in proliferation and regeneration of the developing basilar papilla and lateral line. Dev Neurobiol *74*, 438-456.

Jacques, B.E., Puligilla, C., Weichert, R.M., Ferrer-Vaquer, A., Hadjantonakis, A.K., Kelley, M.W., and Dabdoub, A. (2012). A dual function for canonical Wnt/beta-catenin signaling in the developing mammalian cochlea. Development *139*, 4395-4404.

Jayasena, C.S., Ohyama, T., Segil, N., and Groves, A.K. (2008). Notch signaling augments the canonical Wnt pathway to specify the size of the otic placode. Development *135*, 2251-2261.

Jilani, S.M., Murphy, T.J., Thai, S.N., Eichmann, A., Alva, J.A., and Iruela-Arispe, M.L. (2003). Selective binding of lectins to embryonic chicken vasculature. J Histochem Cytochem *51*, 597-604.

Julander, J.G., Siddharthan, V., Park, A.H., Preston, E., Mathur, P., Bertolio, M., Wang, H., Zukor, K., Van Wettere, A.J., Sinex, D.G.*, et al.* (2018). Consequences of in utero exposure to Zika virus in offspring of AG129 mice. Sci Rep *8*, 9384.

Katayama, A., and Corwin, J.T. (1989). Cell production in the chicken cochlea. J Comp Neurol *281*, 129-135.

Kawakami, A., Kimura-Kawakami, M., Nomura, T., and Fujisawa, H. (1997). Distributions of PAX6 and PAX7 proteins suggest their involvement in both early and late phases of chick brain development. Mech Dev *66*, 119-130.

Khorevin, V.I. (2008). The Lagena (the Third Otolith Endorgan in Vertebrates). Neurophysiology *40*, 142-159.

Kiernan, A.E. (2006). The paintfill method as a tool for analyzing the three-dimensional structure of the inner ear. Brain Res *1091*, 270-276.

Knowlton, V.Y. (1967). Correlation of Development of Membranous and Bony Labyrinths Acoustic Ganglia Nerves and Brain Centers of Chick Embryo. Journal of Morphology *121*, 179-&.

Lang, H., Bever, M.M., and Fekete, D.M. (2000). Cell proliferation and cell death in the developing chick inner ear: spatial and temporal patterns. J Comp Neurol *417*, 205-220.

Langevin, S.A., Bunning, M., Davis, B., and Komar, N. (2001). Experimental infection of chickens as candidate sentinels for West Nile virus. Emerg Infect Dis *7*, 726-729.

Lazear, H.M., Govero, J., Smith, A.M., Platt, D.J., Fernandez, E., Miner, J.J., and Diamond, M.S. (2016). A Mouse Model of Zika Virus Pathogenesis. Cell Host Microbe *19*, 720-730.

Le Dreau, G., and Marti, E. (2012). Dorsal-ventral patterning of the neural tube: a tale of three signals. Dev Neurobiol *72*, 1471-1481.

Leal, M.C., Muniz, L.F., Caldas Neto, S.D., van der Linden, V., and Ramos, R.C. (2016a). Sensorineural hearing loss in a case of congenital Zika virus. Braz J Otorhinolaryngol.

Leal, M.C., Muniz, L.F., Ferreira, T.S., Santos, C.M., Almeida, L.C., Van Der Linden, V., Ramos, R.C., Rodrigues, L.C., and Neto, S.S. (2016b). Hearing Loss in Infants with Microcephaly and Evidence of Congenital Zika Virus Infection - Brazil, November 2015-May 2016. MMWR Morb Mortal Wkly Rep *65*, 917-919.

Leucht, C., Stigloher, C., Wizenmann, A., Klafke, R., Folchert, A., and Bally-Cuif, L. (2008). MicroRNA-9 directs late organizer activity of the midbrain-hindbrain boundary. Nat Neurosci *11*, 641-648.

Li, C., Xu, D., Ye, Q., Hong, S., Jiang, Y., Liu, X., Zhang, N., Shi, L., Qin, C.F., and Xu, Z. (2016a). Zika Virus Disrupts Neural Progenitor Development and Leads to Microcephaly in Mice. Cell Stem Cell *19*, 672.

Li, H., Saucedo-Cuevas, L., Regla-Nava, J.A., Chai, G., Sheets, N., Tang, W., Terskikh, A.V., Shresta, S., and Gleeson, J.G. (2016b). Zika Virus Infects Neural Progenitors in the Adult Mouse Brain and Alters Proliferation. Cell Stem Cell *19*, 593-598.

Li, H., Saucedo-Cuevas, L., Shresta, S., and Gleeson, J.G. (2016c). The Neurobiology of Zika Virus. Neuron *92*, 949-958.

Li, V.S., Ng, S.S., Boersema, P.J., Low, T.Y., Karthaus, W.R., Gerlach, J.P., Mohammed, S., Heck, A.J., Maurice, M.M., Mahmoudi, T.*, et al.* (2012). Wnt signaling through inhibition of beta-catenin degradation in an intact Axin1 complex. Cell *149*, 1245-1256.

Liang, J.K., Bok, J., and Wu, D.K. (2010). Distinct contributions from the hindbrain and mesenchyme to inner ear morphogenesis. Dev Biol *337*, 324-334.

Liang, Q., Luo, Z., Zeng, J., Chen, W., Foo, S.S., Lee, S.A., Ge, J., Wang, S., Goldman, S.A., Zlokovic, B.V.*, et al.* (2016). Zika Virus NS4A and NS4B Proteins Deregulate Akt-mTOR Signaling in Human Fetal Neural Stem Cells to Inhibit Neurogenesis and Induce Autophagy. Cell Stem Cell *19*, 663-671.

Lim, R., and Brichta, A.M. (2016). Anatomical and physiological development of the human inner ear. Hear Res *338*, 9-21.

Lim, Y., and Golden, J.A. (2007). Patterning the developing diencephalon. Brain Res Rev *53*, 17-26.

Lowery, L.A., and Sive, H. (2009). Totally tubular: the mystery behind function and origin of the brain ventricular system. Bioessays *31*, 446-458.

Marigo, V., and Tabin, C.J. (1996). Regulation of patched by sonic hedgehog in the developing neural tube. Proc Natl Acad Sci U S A *93*, 9346-9351.

Marrs, C., Olson, G., Saade, G., Hankins, G., Wen, T., Patel, J., and Weaver, S. (2016). Zika Virus and Pregnancy: A Review of the Literature and Clinical Considerations. Am J Perinatol *33*, 625-639.

Martinez-Lopez, J.E., Moreno-Bravo, J.A., Madrigal, M.P., Martinez, S., and Puelles, E. (2015). Mesencephalic basolateral domain specification is dependent on Sonic Hedgehog. Front Neuroanat *9*, 12.

Matsumoto, K., Miki, R., Nakayama, M., Tatsumi, N., and Yokouchi, Y. (2008). Wnt9a secreted from the walls of hepatic sinusoids is essential for morphogenesis, proliferation, and glycogen accumulation of chick hepatic epithelium. Dev Biol *319*, 234-247.

Meertens, L., Labeau, A., Dejarnac, O., Cipriani, S., Sinigaglia, L., Bonnet-Madin, L., Le Charpentier, T., Hafirassou, M.L., Zamborlini, A., Cao-Lormeau, V.M.*, et al.* (2017). Axl Mediates ZIKA Virus Entry in Human Glial Cells and Modulates Innate Immune Responses. Cell Rep *18*, 324-333.

Melo, A.S., Aguiar, R.S., Amorim, M.M., Arruda, M.B., Melo, F.O., Ribeiro, S.T., Batista, A.G., Ferreira, T., Dos Santos, M.P., Sampaio, V.V.*, et al.* (2016). Congenital Zika Virus Infection: Beyond Neonatal Microcephaly. JAMA Neurol *73*, 1407-1416.

Miner, J.J., Cao, B., Govero, J., Smith, A.M., Fernandez, E., Cabrera, O.H., Garber, C., Noll, M., Klein, R.S., Noguchi, K.K.*, et al.* (2016a). Zika Virus Infection during Pregnancy in Mice Causes Placental Damage and Fetal Demise. Cell *165*, 1081-1091.

Miner, J.J., and Diamond, M.S. (2017). Zika Virus Pathogenesis and Tissue Tropism. Cell Host Microbe *21*, 134-142.

Miner, J.J., Sene, A., Richner, J.M., Smith, A.M., Santeford, A., Ban, N., Weger-Lucarelli, J., Manzella, F., Ruckert, C., Govero, J.*, et al.* (2016b). Zika Virus Infection in Mice Causes Panuveitis with Shedding of Virus in Tears. Cell Rep *16*, 3208-3218.

Misson, J.P., Edwards, M.A., Yamamoto, M., and Caviness, V.S., Jr. (1988). Mitotic cycling of radial glial cells of the fetal murine cerebral wall: a combined autoradiographic and immunohistochemical study. Brain Res *466*, 183-190.

Mittal, R., Fifer, R.C., and Liu, X.Z. (2017). A Possible Association Between Hearing Loss and Zika Virus Infections. JAMA Otolaryngol Head Neck Surg.

Mlacker, S., Shafa, G., Aldahan, A.S., Shah, V.V., Samarkandy, S., and Nouri, K. (2016). Origin of the Zika virus revealed: a historical journey across the world. Int J Dermatol *55*, 1369-1372.

Moore, C.A., Staples, J.E., Dobyns, W.B., Pessoa, A., Ventura, C.V., Fonseca, E.B., Ribeiro, E.M., Ventura, L.O., Neto, N.N., Arena, J.F.*, et al.* (2017). Characterizing the Pattern of Anomalies in Congenital Zika Syndrome for Pediatric Clinicians. JAMA Pediatr *171*, 288-295.

Mourya, D.T., Shil, P., Sapkal, G.N., and Yadav, P.D. (2016). Zika virus: Indian perspectives. Indian J Med Res *143*, 553-564.

Muller, P., Rogers, K.W., Yu, S.R., Brand, M., and Schier, A.F. (2013). Morphogen transport. Development *140*, 1621-1638.

Munnamalai, V., and Fekete, D.M. (2013). Wnt signaling during cochlear development. Semin Cell Dev Biol *24*, 480-489.

Munnamalai, V., and Fekete, D.M. (2016). Organotypic Culture of the Mouse Cochlea from Embryonic Day 12 to the Neonate. Methods Mol Biol *1427*, 293-303.

Munnamalai, V., Sienknecht, U.J., Duncan, R.K., Scott, M.K., Thawani, A., Fantetti, K.N., Atallah, N.M., Biesemeier, D.J., Song, K.H., Luethy, K.*, et al.* (2017). Wnt9a Can Influence Cell Fates and Neural Connectivity across the Radial Axis of the Developing Cochlea. J Neurosci *37*, 8975-8988.

Musso, D., Nilles, E.J., and Cao-Lormeau, V.M. (2014). Rapid spread of emerging Zika virus in the Pacific area. Clin Microbiol Infect *20*, O595-596.

Neves, J., Kamaid, A., Alsina, B., and Giraldez, F. (2007). Differential expression of Sox2 and Sox3 in neuronal and sensory progenitors of the developing inner ear of the chick. J Comp Neurol *503*, 487-500.

Neves, J., Parada, C., Chamizo, M., and Giraldez, F. (2011). Jagged 1 regulates the restriction of Sox2 expression in the developing chicken inner ear: a mechanism for sensory organ specification. Development *138*, 735-744.

Nishitani, A.M., Ohta, S., Yung, A.R., Del Rio, T., Gordon, M.I., Abraira, V.E., Aviles, E.C., Schoenwolf, G.C., Fekete, D.M., and Goodrich, L.V. (2017). Distinct functions for netrin 1 in chicken and murine semicircular canal morphogenesis. Development *144*, 3349-3360.

Nowakowski, T.J., Pollen, A.A., Di Lullo, E., Sandoval-Espinosa, C., Bershteyn, M., and Kriegstein, A.R. (2016). Expression Analysis Highlights AXL as a Candidate Zika Virus Entry Receptor in Neural Stem Cells. Cell Stem Cell *18*, 591-596.

Nusse, R. (2012). Wnt signaling. Cold Spring Harb Perspect Biol *4*.

Oesterle, E.C., Cunningham, D.E., and Rubel, E.W. (1992). Ultrastructure of hyaline, border, and vacuole cells in chick inner ear. J Comp Neurol *318*, 64-82.

Ohyama, K., Das, R., and Placzek, M. (2008). Temporal progression of hypothalamic patterning by a dual action of BMP. Development *135*, 3325-3331.

Ohyama, T., Mohamed, O.A., Taketo, M.M., Dufort, D., and Groves, A.K. (2006). Wnt signals mediate a fate decision between otic placode and epidermis. Development *133*, 865-875.

Osuna, C.E., Lim, S.Y., Deleage, C., Griffin, B.D., Stein, D., Schroeder, L.T., Omange, R.W., Best, K., Luo, M., Hraber, P.T.*, et al.* (2016). Zika viral dynamics and shedding in rhesus and cynomolgus macaques. Nat Med *22*, 1448-1455.

Parchem, R.J., Ye, J., Judson, R.L., LaRussa, M.F., Krishnakumar, R., Blelloch, A., Oldham, M.C., and Blelloch, R. (2014). Two miRNA clusters reveal alternative paths in late-stage reprogramming. Cell Stem Cell *14*, 617-631.

Perera-Lecoin, M., Meertens, L., Carnec, X., and Amara, A. (2013). Flavivirus entry receptors: an update. Viruses *6*, 69-88.

Perez-Balaguer, A., Puelles, E., Wurst, W., and Martinez, S. (2009). Shh dependent and independent maintenance of basal midbrain. Mech Dev *126*, 301-313.

Person, A.D., Garriock, R.J., Krieg, P.A., Runyan, R.B., and Klewer, S.E. (2005). Frzb modulates Wnt-9a-mediated beta-catenin signaling during avian atrioventricular cardiac cushion development. Dev Biol *278*, 35-48.

Peterson, A.T., Osorio, J., Qiao, H., and Escobar, L.E. (2016). Zika Virus, Elevation, and Transmission Risk. PLoS Curr *8*.

Petrovic, J., Formosa-Jordan, P., Luna-Escalante, J.C., Abello, G., Ibanes, M., Neves, J., and Giraldez, F. (2014). Ligand-dependent Notch signaling strength orchestrates lateral induction and lateral inhibition in the developing inner ear. Development *141*, 2313-2324.

Pettersson, J.H., Bohlin, J., Dupont-Rouzeyrol, M., Brynildsrud, O.B., Alfsnes, K., Cao-Lormeau, V.M., Gaunt, M.W., Falconar, A.K., de Lamballerie, X., Eldholm, V.*, et al.* (2018). Re-visiting the evolution, dispersal and epidemiology of Zika virus in Asia. Emerg Microbes Infect *7*, 79.

Pettersson, J.H., Eldholm, V., Seligman, S.J., Lundkvist, A., Falconar, A.K., Gaunt, M.W., Musso, D., Nougairede, A., Charrel, R., Gould, E.A.*, et al.* (2016). How Did Zika Virus Emerge in the Pacific Islands and Latin America? MBio *7*.

Puelles, L., and Rubenstein, J.L. (2015). A new scenario of hypothalamic organization: rationale of new hypotheses introduced in the updated prosomeric model. Front Neuroanat *9*, 27.

Purves, D. (2008). Neuroscience, 4th edn (Sunderland, Mass.: Sinauer).

Qian, X., Nguyen, H.N., Jacob, F., Song, H., and Ming, G.L. (2017). Using brain organoids to understand Zika virus-induced microcephaly. Development *144*, 952-957.

Qian, X., Nguyen, H.N., Song, M.M., Hadiono, C., Ogden, S.C., Hammack, C., Yao, B., Hamersky, G.R., Jacob, F., Zhong, C.*, et al.* (2016). Brain-Region-Specific Organoids Using Mini-bioreactors for Modeling ZIKV Exposure. Cell *165*, 1238-1254.

Rakowiecki, S., and Epstein, D.J. (2013). Divergent roles for Wnt/beta-catenin signaling in epithelial maintenance and breakdown during semicircular canal formation. Development *140*, 1730-1739.

Rasmussen, S.A., Jamieson, D.J., Honein, M.A., and Petersen, L.R. (2016). Zika Virus and Birth Defects--Reviewing the Evidence for Causality. N Engl J Med *374*, 1981-1987.

Retallack, H., Di Lullo, E., Arias, C., Knopp, K.A., Laurie, M.T., Sandoval-Espinosa, C., Mancia Leon, W.R., Krencik, R., Ullian, E.M., Spatazza, J.*, et al.* (2016). Zika virus cell tropism in the developing human brain and inhibition by azithromycin. Proc Natl Acad Sci U S A *113*, 14408-14413.

Rhee, J., Buchan, T., Zukerberg, L., Lilien, J., and Balsamo, J. (2007). Cables links Robo-bound Abl kinase to N-cadherin-bound beta-catenin to mediate Slit-induced modulation of adhesion and transcription. Nat Cell Biol *9*, 883-892.

Rossi, S.L., Tesh, R.B., Azar, S.R., Muruato, A.E., Hanley, K.A., Auguste, A.J., Langsjoen, R.M., Paessler, S., Vasilakis, N., and Weaver, S.C. (2016). Characterization of a Novel Murine Model to Study Zika Virus. Am J Trop Med Hyg *94*, 1362-1369.

Rubenstein, J.L., and Puelles, L. (1994). Homeobox gene expression during development of the vertebrate brain. Curr Top Dev Biol *29*, 1-63.

Ryder, E.F., and Cepko, C.L. (1994). Migration patterns of clonally related granule cells and their progenitors in the developing chick cerebellum. Neuron *12*, 1011-1028.

Sacramento, C.Q., de Melo, G.R., de Freitas, C.S., Rocha, N., Hoelz, L.V., Miranda, M., Fintelman-Rodrigues, N., Marttorelli, A., Ferreira, A.C., Barbosa-Lima, G.*, et al.* (2017). The clinically approved antiviral drug sofosbuvir inhibits Zika virus replication. Sci Rep *7*, 40920.

Sanchez-Calderon, H., Martin-Partido, G., and Hidalgo-Sanchez, M. (2005). Pax2 expression patterns in the developing chick inner ear. Gene Expr Patterns *5*, 763-773.

Satoh, T., and Fekete, D.M. (2005). Clonal analysis of the relationships between mechanosensory cells and the neurons that innervate them in the chicken ear. Development *132*, 1687-1697.

Scholpp, S., Wolf, O., Brand, M., and Lumsden, A. (2006). Hedgehog signalling from the zona limitans intrathalamica orchestrates patterning of the zebrafish diencephalon. Development *133*, 855-864.

Shan, C., Xie, X., Muruato, A.E., Rossi, S.L., Roundy, C.M., Azar, S.R., Yang, Y., Tesh, R.B., Bourne, N., Barrett, A.D.*, et al.* (2016). An Infectious cDNA Clone of Zika Virus to Study Viral Virulence, Mosquito Transmission, and Antiviral Inhibitors. Cell Host Microbe *19*, 891-900.

Shao, Q., Herrlinger, S., Yang, S.L., Lai, F., Moore, J.M., Brindley, M.A., and Chen, J.F. (2016). Zika virus infection disrupts neurovascular development and results in postnatal microcephaly with brain damage. Development *143*, 4127-4136.

Siedner, M.J., Ryan, E.T., and Bogoch, II (2018). Gone or forgotten? The rise and fall of Zika virus. Lancet Public Health *3*, e109-e110.

Sienknecht, U.J., and Fekete, D.M. (2008). Comprehensive Wnt-related gene expression during cochlear duct development in chicken. J Comp Neurol *510*, 378-395.

Sienknecht, U.J., and Fekete, D.M. (2009). Mapping of Wnt, frizzled, and Wnt inhibitor gene expression domains in the avian otic primordium. J Comp Neurol *517*, 751-764.

Singh, P.K., Guest, J.M., Kanwar, M., Boss, J., Gao, N., Juzych, M.S., Abrams, G.W., Yu, F.S., and Kumar, A. (2017). Zika virus infects cells lining the blood-retinal barrier and causes chorioretinal atrophy in mouse eyes. JCI Insight *2*, e92340.

Singh, S., and Groves, A.K. (2016). The molecular basis of craniofacial placode development. Wiley Interdiscip Rev Dev Biol *5*, 363-376.

Sirohi, D., Chen, Z., Sun, L., Klose, T., Pierson, T.C., Rossmann, M.G., and Kuhn, R.J. (2016). The 3.8 A resolution cryo-EM structure of Zika virus. Science *352*, 467-470.

Sirohi, D., and Kuhn, R.J. (2017). Zika Virus Structure, Maturation, and Receptors. J Infect Dis *216*, S935-S944.

Spater, D., Hill, T.P., O'Sullivan R, J., Gruber, M., Conner, D.A., and Hartmann, C. (2006). Wnt9a signaling is required for joint integrity and regulation of Ihh during chondrogenesis. Development *133*, 3039-3049.

Steel, K.P., and Barkway, C. (1989). Another role for melanocytes: their importance for normal stria vascularis development in the mammalian inner ear. Development *107*, 453-463.

Steevens, A.R., Sookiasian, D.L., Glatzer, J.C., and Kiernan, A.E. (2017). SOX2 is required for inner ear neurogenesis. Sci Rep *7*, 4086.

Stevens, C.B., Davies, A.L., Battista, S., Lewis, J.H., and Fekete, D.M. (2003). Forced activation of Wnt signaling alters morphogenesis and sensory organ identity in the chicken inner ear. Dev Biol *261*, 149-164.

Swinburne, I.A., Mosaliganti, K.R., Upadhyayula, S., Liu, T.L., Hildebrand, D.G.C., Tsai, T.Y., Chen, A., Al-Obeidi, E., Fass, A.K., Malhotra, S.*, et al.* (2018). Lamellar projections in the endolymphatic sac act as a relief valve to regulate inner ear pressure. Elife *7*.

Tanaka, K., and Smith, C.A. (1978). Structure of the chicken's inner ear: SEM and TEM study. Am J Anat *153*, 251-271.

Thawani, A., Sirohi, D., Kuhn, R.J., and Fekete, D.M. (2018). Zika Virus Can Strongly Infect and Disrupt Secondary Organizers in the Ventricular Zone of the Embryonic Chicken Brain. Cell Rep *23*, 692-700.

Torres, M., and Giraldez, F. (1998). The development of the vertebrate inner ear. Mech Dev *71*, 5-21.

van Amerongen, R., and Nusse, R. (2009). Towards an integrated view of Wnt signaling in development. Development *136*, 3205-3214.

van Noort, M., Meeldijk, J., van der Zee, R., Destree, O., and Clevers, H. (2002). Wnt signaling controls the phosphorylation status of beta-catenin. J Biol Chem *277*, 17901-17905.

Ventura, C.V., Maia, M., Ventura, B.V., Linden, V.V., Araujo, E.B., Ramos, R.C., Rocha, M.A., Carvalho, M.D., Belfort, R., Jr., and Ventura, L.O. (2016). Ophthalmological findings in infants with microcephaly and presumable intra-uterus Zika virus infection. Arq Bras Oftalmol *79*, 1-3.

Vermillion, M.S., Lei, J., Shabi, Y., Baxter, V.K., Crilly, N.P., McLane, M., Griffin, D.E., Pekosz, A., Klein, S.L., and Burd, I. (2017). Intrauterine Zika virus infection of pregnant immunocompetent mice models transplacental transmission and adverse perinatal outcomes. Nat Commun *8*, 14575.

Vinhaes, E.S., Santos, L.A., Dias, L., Andrade, N.A., Bezerra, V.H., de Carvalho, A.T., de Moraes, L., Henriques, D.F., Azar, S.R., Vasilakis, N.*, et al.* (2017). Transient Hearing Loss in Adults Associated With Zika Virus Infection. Clin Infect Dis *64*, 675-677.

Wang, J., Liu, J., Zhou, R., Ding, X., Zhang, Q., Zhang, C., and Li, L. (2018). Zika virus infected primary microglia impairs NPCs proliferation and differentiation. Biochem Biophys Res Commun *497*, 619-625.

Weaver, S.C., Costa, F., Garcia-Blanco, M.A., Ko, A.I., Ribeiro, G.S., Saade, G., Shi, P.Y., and Vasilakis, N. (2016). Zika virus: History, emergence, biology, and prospects for control. Antiviral Res *130*, 69-80.

Weber, F., Wagner, V., Rasmussen, S.B., Hartmann, R., and Paludan, S.R. (2006). Double-stranded RNA is produced by positive-strand RNA viruses and DNA viruses but not in detectable amounts by negative-strand RNA viruses. J Virol *80*, 5059-5064.

Weger-Lucarelli, J., Ruckert, C., Chotiwan, N., Nguyen, C., Garcia Luna, S.M., Fauver, J.R., Foy, B.D., Perera, R., Black, W.C., Kading, R.C*., et al.* (2016). Vector Competence of American Mosquitoes for Three Strains of Zika Virus. PLoS Negl Trop Dis *10*, e0005101.

Wells, M.F., Salick, M.R., Wiskow, O., Ho, D.J., Worringer, K.A., Ihry, R.J., Kommineni, S., Bilican, B., Klim, J.R., Hill, E.J*., et al.* (2016). Genetic Ablation of AXL Does Not Protect Human Neural Progenitor Cells and Cerebral Organoids from Zika Virus Infection. Cell Stem Cell *19*, 703-708.

Winter, J., Jung, S., Keller, S., Gregory, R.I., and Diederichs, S. (2009). Many roads to maturity: microRNA biogenesis pathways and their regulation. Nat Cell Biol *11*, 228-234.

Wolpert, L. (2007). Principles of development, 3rd edn (Oxford ; New York: Oxford University Press).

World Health Organization (WHO). (2018). Mosquito control: can it stop Zika at source? Available at: https://www.who.int/emergencies/zika-virus/articles/mosquito-control/en/

Wu, D.K., and Kelley, M.W. (2012). Molecular mechanisms of inner ear development. Cold Spring Harb Perspect Biol *4*, a008409.

Wu, D.K., and Oh, S.H. (1996). Sensory organ generation in the chick inner ear. J Neurosci *16*, 6454-6462.

Wu, K.Y., Zuo, G.L., Li, X.F., Ye, Q., Deng, Y.Q., Huang, X.Y., Cao, W.C., Qin, C.F., and Luo, Z.G. (2016). Vertical transmission of Zika virus targeting the radial glial cells affects cortex development of offspring mice. Cell Res *26*, 645-654.

Wu, Y.H., Cui, X.Y., Yang, W., Fan, D.Y., Liu, D., Wang, P.G., and An, J. (2018). Zika Virus Infection in Hypothalamus Causes Hormone Deficiencies and Leads to Irreversible Growth Delay and Memory Impairment in Mice. Cell Rep *25*, 1537-1547 e1534.

Wurst, W., and Bally-Cuif, L. (2001). Neural plate patterning: upstream and downstream of the isthmic organizer. Nat Rev Neurosci *2*, 99-108.

Yockey, L.J., Varela, L., Rakib, T., Khoury-Hanold, W., Fink, S.L., Stutz, B., Szigeti-Buck, K., Van den Pol, A., Lindenbach, B.D., Horvath, T.L*., et al.* (2016). Vaginal Exposure to Zika Virus during Pregnancy Leads to Fetal Brain Infection. Cell *166*, 1247-1256 e1244.

Yoon, K.J., Song, G., Qian, X., Pan, J., Xu, D., Rho, H.S., Kim, N.S., Habela, C., Zheng, L., Jacob, F*., et al.* (2017). Zika-Virus-Encoded NS2A Disrupts Mammalian Cortical Neurogenesis by Degrading Adherens Junction Proteins. Cell Stem Cell *21*, 349-358 e346.

Yuan, L., Huang, X.Y., Liu, Z.Y., Zhang, F., Zhu, X.L., Yu, J.Y., Ji, X., Xu, Y.P., Li, G., Li, C., *et al.* (2017). A single mutation in the prM protein of Zika virus contributes to fetal microcephaly. Science *358*, 933-936.

Zhang, K.D., Stoller, M.L., and Fekete, D.M. (2015). Expression and Misexpression of the miR-183 Family in the Developing Hearing Organ of the Chicken. PLoS One *10*, e0132796.

Zhu, J., Luz-Madrigal, A., Haynes, T., Zavada, J., Burke, A.K., and Del Rio-Tsonis, K. (2014). beta-Catenin inactivation is a pre-requisite for chick retina regeneration. PLoS One *9*, e101748.

Zhu, Z., Chan, J.F., Tee, K.M., Choi, G.K., Lau, S.K., Woo, P.C., Tse, H., and Yuen, K.Y. (2016). Comparative genomic analysis of pre-epidemic and epidemic Zika virus strains for virological factors potentially associated with the rapidly expanding epidemic. Emerg Microbes Infect *5*, e22.

VITA

Ankita Thawani will continue her Developmental Biology research training as a Postdoctoral Associate at Baylor College of Medicine, Houston TX starting March 2019.

Education

Ph.D. in Biological Sciences, Purdue University (2013-19)
Advisor: Dr. Donna M. Fekete

B.Tech. and **M.Tech.** in Biochemical Engineering & Biotechnology, Indian Institute of Technology Delhi (2007-12)
Minor Degree in Management Studies
Master's Advisor: Dr. Saroj Mishra

Publications

Thawani A, Sammudin NH, Reygaerts H, Munnamalai V, Kuhn RJ, & Fekete DM. (2019). Zika virus infects the vestibular and auditory organs of the developing inner ear in the chicken embryo. (Manuscript in preparation)

Thawani A, Sirohi D, Kuhn RJ, & Fekete DM. (2018). Zika virus can strongly infect and disrupt secondary organizers in the ventricular zone of the embryonic chicken brain. *Cell Reports, 23(3),* 692-700.

Munnamalai V, Sienknecht UJ, Duncan RK, Scott MK, Thawani A, Fantetti KN, ... & Fekete DM. (2017). Wnt9a can influence cell fates and neural connectivity across the radial axis of the developing cochlea. *Journal of Neuroscience*, *37*(37), 8975-8988.

Kong Y, Thawani A, Anderson T, & Pelaez N (2017). A Model of the Use of Evolutionary Trees (MUET) to Inform K-14 Biology Education. *The American Biology Teacher*, *79*(2), 81-90.

Maity N, Thawani A, Sharma A, Gautam A, Mishra S, & Sahai V (2015). Expression and Control of Codon-Optimized Granulocyte Colony-Stimulating Factor in *Pichia pastoris*. *Applied Biochemistry and Biotechnology*, 1-14.

Nasir MN, Thawani A, Kouzayha A, & Besson F (2010). Interactions of the natural antimicrobial mycosubtilin with phospholipid membrane models. *Colloids and Surfaces B: Biointerfaces*, *78*(1), 17-23.

Fellowships, Scholarships and Awards

- Best Talk Award, Biology Graduate Research Symposium, Purdue University (2018)
- Bilsland Dissertation Fellowship, Purdue University (Fall semester 2018)
- Biology Graduate Teaching Award, Purdue University (2018)
- Purdue Research Foundation Fellowship, Purdue University (2017-18)
- Neuroscience Research Travel Award, Purdue Institute for Integrative Neuroscience (2017)
- Society for Developmental Biology Travel Award (2017)
- Best Poster Award- 2nd position, Annual Biology Graduate Student Retreat, Purdue University (2016)
- Association for Research in Otolaryngology (ARO) Travel Award (2016)
- MHRD Scholarship Graduate Aptitude Test in Engineering (GATE) Scholarship (2011-12)
- French Government Scholarship by Embassy of France in India for internship (Summer 2009)

Oral presentations

Zika virus pathogenesis in the developing inner ear

- Sensorium- annual symposium of Sensory Biology and Ecology (Nov 2018)

Zika virus and brain development

- Biology Graduate Research Symposium, Purdue University (Aug 2018)
- Purdue Institute of Inflammation, Immunology and Infectious Disease Lecture Series, Purdue University (Invited speaker, Feb 2018)

Zika virus exhibits differential tropism in developing chicken brain and inner ear

- Seminars in Hearing Research, Purdue University (Aug 2018)
- Purdue University Department of Biological Sciences Annual Retreat (Invited speaker, Nov 2017)
- Seminars in Hearing Research, Purdue University (Sep 2017)
- Neuro(R)evolution: New Approaches for Studying Neurodevelopment. Society for Developmental Biology Satellite Symposium (Invited speaker, Jul 2017)
- Neuroscience and Physiology Seminar, Purdue University (Selected speaker, Feb 2017)
- Seminars in Hearing Research, Purdue University (Sep 2016)
- Annual Biology Graduate Student Retreat, Purdue University (Aug 2016)

Investigating Cellular Patterning in the Developing Chicken Auditory Organ

- Seminars in Hearing Research, Purdue University (Sep 2015)

Poster presentations

Thawani A, Sammudin NH, Reygaerts H, Sirohi D, Munnamalai V, Kuhn RJ, Fekete DM. Zika virus tropism in the early developing brain and inner ear of the chicken embryo

- Gordon Research Conference- Neural Development (2018)

Thawani A, Sirohi D, Kuhn RJ, Fekete DM. Zika virus exhibits differential tropism within the developing brain

- Society for Developmental Biology (SDB) (2017)
- Purdue Institute of Integrative Neuroscience summer retreat (2017)
- Office of Interdisciplinary Graduate Programs spring reception, Purdue University (2017)

Thawani A, Scott MK, Munnamalai V, Sienknecht UJ, Fekete DM. Seeking Evidence for the Role of Canonical Wnt/β-Catenin Signaling in Radial Axis Patterning of Chicken Basilar Papilla

- Annual Biology Graduate Student Retreat, Purdue University (2016)
- Society for Neuroscience – Indianapolis chapter (IndySfN) (2016)
- Association for Research in Otolaryngology (ARO) (2016)

Research Experience

Doctoral Dissertation, Purdue University, IN: Advisor: Dr. Donna Fekete (Aug 2014 – present)

- Exploring Zika virus tropism in developing chicken inner ear by direct inoculation of the embryonic inner ear
- Analyzed Zika virus tropism in early stages of developing chicken brain by direct injections and found strong infection and disruption at the morphogen-producing secondary organizers
- Tested asymmetry in β-catenin expression as a direct readout of canonical Wnt pathway in radial axis patterning in the developing chicken auditory organ
- Identifying differentially expressed microRNAs along the radial axis of the developing chicken auditory organ by RNA sequencing

Rotation project, Purdue University, IN: Advisor: Dr. Nancy Pelaez (Aug 2013 – May 2014)

- Designed an educational tool to fully describe the information in phylogenetic trees using the "model of modeling" framework with the goal to improve the classroom instruction of evolutionary trees

Master's Thesis, Indian Institute of Technology Delhi, India: Advisor: Dr. Saroj Mishra (May 2011 – Jun 2012)

- Cloning and expression of an optimized Granulocyte Colony Stimulating Factor (GCSF) in *Pichia pastoris*

Internship, Reliance Life Sciences, Mumbai, India: Advisors: Ms. Arundhati Mandal, Dr. Chandra Vishwanathan (May 2010 – Jul 2010)

- Trained in specialized techniques for human embryonic stem cell culture and maintenance
- Analyzed the cytotoxicity of various pharmaceutical drugs in hepatocytes *in vitro* and evidenced xenobiotic specificity of Cytochrome P450 monooxygenases (CYP) expression

Internship, Univérsité Claude Bernard Lyon, France: Advisor: Dr. Françoise Besson (May 2009 – Jul 2009)

- Studied interactions of Alkaline Phosphatase and Mycosubtilin (natural anti-fungal) with various phospholipid membrane molecules using biomimetic layers generated on air-water and air-glycine interface

Teaching Experience

Purdue University, Research Mentor

- Hannah Reygaerts, Undergraduate (Jun 2017 – August 2018)
- Zoe M. Cubero, Summer research student from Puerto Rico University (Jun 2018 – July 2018)
- Nabilah Hamdiah Binti Che Sammudin, Undergraduate Alumna (Apr 2017 – Dec 2017)
- Sydney B. Tola, Undergraduate Alumna (May 2015 – Dec 2016)

Purdue University, Teaching Assistant

- Principles of Development, Laboratory (Spring semester 2015-17)
- Biology for Elementary School Teachers, Laboratory (Fall semester 2014, Spring semester 2014)
- Biology of the Living Cell, Lecture (Fall semester 2013)

Professional Experience

Women In Science Programs Leadership Team Member, Purdue University, IN (2017-18)**:**

- Department of Biological Sciences representative

Biology Graduate Admissions Committee Member, Purdue University, IN (2017):

- Student representative of graduate admissions committee for PhD and MS programs

Business Analytics Associate, ZS Associates, New Delhi, India (Jul 2012 – Jul 2013):

- Worked on quantitative promotional strategy analysis projects for pharmaceutical products in US and European markets as a part of Promotional Response Expertise Centre

Affiliations

- Society for Developmental Biology (SDB)- Member (2017-present)
- Purdue Institute of Inflammation, Immunology and Infectious Disease (PI4D)- Member (2017-present)
- Purdue Institute of Integrative Neuroscience (PIIN)- Member (2016-present)
- Association for Research in Otolaryngology (ARO)- Member (2015-present)
- Women in Science Programs (WISP)- Member (2013-present)